

1

²A SEARCH FOR LONG-LIVED, CHARGED, SUPERSYMMETRIC PARTICLES
³USING IONIZATION WITH THE ATLAS DETECTOR

4

BRADLEY AXEN

5

September 2016 – Version 0.44

6



⁸ Bradley Axen: *A Search for Long-Lived, Charged, Supersymmetric Particles using*
⁹ *Ionization with the ATLAS Detector*, Subtitle, © September 2016

10

Usually a quotation.

11

Dedicated to.

₁₂ ABSTRACT

₁₃ How to write a good abstract:

₁₄ <https://plg.uwaterloo.ca/~migod/research/beck00PSLA.html>

₁₅ PUBLICATIONS

₁₆ Some ideas and figures have appeared previously in the following publications:

₁₇

₁₈ Put your publications from the thesis here. The packages `multibib` or `bibtopic`
₁₉ etc. can be used to handle multiple different bibliographies in your document.

²¹ ACKNOWLEDGEMENTS

²² Put your acknowledgements here.

²³

²⁴ And potentially a second round.

²⁵

26 CONTENTS

27	I	INTRODUCTION	1
28	1	INTRODUCTION	3
29	II	THEORETICAL CONTEXT	5
30	2	STANDARD MODEL	7
31	2.1	Particles	7
32	2.2	Interactions	8
33	2.3	Limitations	8
34	3	SUPERSYMMETRY	9
35	3.1	Motivation	9
36	3.2	Structure	9
37	3.3	Phenomenology	9
38	4	LONG-LIVED PARTICLES	11
39	4.1	Mechanisms	11
40	4.1.1	Examples in Supersymmetry	11
41	4.2	Phenomenology	11
42	4.2.1	Disimilarities to Prompt Decays	11
43	4.2.2	Characteristic Signatures	11
44	III	EXPERIMENTAL STRUCTURE AND RECONSTRUCTION	13
45	5	THE LARGE HADRON COLLIDER	15
46	5.1	Injection Chain	16
47	5.2	Design	17
48	5.2.1	Layout	17
49	5.2.2	Magnets	18
50	5.2.3	RF Cavities	19
51	5.2.4	Beam	21
52	5.3	Luminosity Parameters	21
53	5.4	Delivered Luminosity	23
54	6	THE ATLAS DETECTOR	25
55	6.1	Coordinate System	27
56	6.2	Magnetic Field	28
57	6.3	Inner Detector	30
58	6.3.1	Pixel Detector	33
59	6.3.2	Semiconductor Tracker	35
60	6.3.3	Transition Radiation Tracker	37
61	6.4	Calorimetry	38
62	6.4.1	Electromagnetic Calorimeter	40
63	6.4.2	Hadronic Calorimeters	41
64	6.5	Muon Spectrometer	43
65	6.5.1	Resistive Plate Chamber and Thin Gap Chamber	43

66	6.6	Trigger	44
67	6.6.1	Trigger Scheme	44
68	6.6.2	Missing Transverse Energy Triggers	44
69	7	EVENT RECONSTRUCTION	47
70	7.1	Tracks and Vertices	47
71	7.1.1	Track Reconstruction	47
72	7.1.2	Vertex Reconstruction	47
73	7.2	Jets	47
74	7.2.1	Topological Clustering	47
75	7.2.2	Jet Energy Scale	47
76	7.2.3	Jet Energy Scale Uncertainties	47
77	7.2.4	Jet Energy Resolution	47
78	7.3	Electrons	47
79	7.3.1	Electron Identification	47
80	7.4	Muons	47
81	7.4.1	Muon Identification	47
82	7.5	Missing Transverse Energy	47
83	IV	CALORIMETER RESPONSE	49
84	8	RESPONSE MEASUREMENT WITH SINGLE HADRONS	51
85	8.1	Dataset and Simulation	52
86	8.1.1	Data Samples	52
87	8.1.2	Simulated Samples	52
88	8.1.3	Event Selection	52
89	8.2	Inclusive Hadron Response	53
90	8.2.1	E/p Distribution	53
91	8.2.2	Zero Fraction	54
92	8.2.3	Neutral Background Subtraction	55
93	8.2.4	Corrected Response	57
94	8.2.5	Additional Studies	59
95	8.3	Identified Particle Response	62
96	8.3.1	Decay Reconstruction	62
97	8.3.2	Identified Response	63
98	8.3.3	Additional Species in Simulation	65
99	8.4	Summary	66
100	9	JET ENERGY RESPONSE AND UNCERTAINTY	69
101	9.1	Motivation	69
102	9.2	Uncertainty Estimate	69
103	9.3	Summary	72
104	V	SEARCH FOR LONG-LIVED PARTICLES	75
105	10	LONG-LIVED PARTICLES IN ATLAS	77
106	10.1	Event Topology	77
107	10.1.1	Detector Interactions	78
108	10.1.2	Lifetime Dependence	79
109	10.2	Simulation	82

110	11	EVENT SELECTION	85
111	11.1	Trigger	86
112	11.2	Kinematics and Isolation	87
113	11.3	Particle Species Rejection	91
114	11.4	Ionization	94
115	11.4.1	Mass Estimation	95
116	11.5	Efficiency	96
117	12	BACKGROUND ESTIMATION	99
118	12.1	Background Sources	99
119	12.2	Prediction Method	100
120	12.3	Validation	101
121	12.3.1	Closure in Simulation	101
122	12.3.2	Validation Region in Data	102
123	13	SYSTEMATIC UNCERTAINTIES AND RESULTS	105
124	13.1	Systematic Uncertainties	105
125	13.1.1	Background Estimate	105
126	13.1.2	Signal Yield	106
127	13.2	Final Yields	112
128	13.3	Cross Sectional Limits	113
129	13.4	Mass Limits	115
130	13.5	Context for Long-Lived Searches	117
131	VI	CONCLUSIONS	121
132	14	SUMMARY AND OUTLOOK	123
133	14.1	Summary	123
134	14.2	Outlook	123
135	VII	APPENDIX	125
136	A	INELASTIC CROSS SECTION	127
137	B	EXPANDED R-HADRON YIELDS AND LIMITS	129
138		BIBLIOGRAPHY	135

139 LIST OF FIGURES

140	Figure 1	The particle content of the Standard Model (SM).	8
141	Figure 2	The four collision points and corresponding experiments of the Large Hadron Collider (LHC). The image includes the location of the nearby city of Geneva as well as the border of France and Switzerland.	16
142			
143			
144			
145	Figure 3	The cumulative luminosity over time delivered to the A Toroidal LHC ApparatuS (ATLAS) experiment from high energy proton-proton collisions since 2011. The energies of the collisions are listed for each of the data-taking periods.	17
146			
147			
148			
149			
150	Figure 4	The accelerator complex that builds up to the full design energies at the LHC . The protons are passed in order to Linac 2, the PSB , the PS , the SPS and then the LHC	18
151			
152			
153			
154	Figure 5	A schematic of the layout of the LHC , not to scale. The arched and straight sections are illustrated at the bottom of the schematic, and all four crossing sites are indicated with their respective experiments.	19
155			
156			
157			
158	Figure 6	A cross section of the the cryodipole magnets which bend the flight path of protons around the circumference of the LHC . The diagram includes both the superconducting coils which produce the magnetic field and the structural elements which keep the magnets precisely aligned.	20
159			
160			
161			
162			
163			
164	Figure 7	The arrangement of four radiofrequency (RF) cavities within a cryomodule.	20
165			
166	Figure 8	The cumulative luminosity versus time delivered to ATLAS (green), recorded by ATLAS (yellow), and certified to be good quality data (blue) during stable beams for pp collisions at 13 TeV in 2015.	23
167			
168			
169			
170	Figure 9	The luminosity-weighted distribution of the mean number of interactions per crossing for the 2015 pp collision data at 13 TeV.	24
171			
172			
173	Figure 10	A cut-away schematic of the layout of the ATLAS detector. Each of the major subsystems is indicated.	26
174			
175	Figure 11	A cross-sectional slice of the ATLAS experiment which illustrates how the various SM particles interact with the detector systems.	26
176			
177			
178	Figure 12	The layout of the four superconducting magnets in the ATLAS detector.	29
179			

180	Figure 13	The arrangement of the subdetectors of the ATLAS inner detector. Each of the subdetectors is labelled in the cut-away view of the system.	31
181			
182			
183	Figure 14	A quarter section of the ATLAS inner detector which shows the layout of each of the subdetectors in detail. The lower panel shows an enlarged view of the pixel detector. Example trajectories for a particle with $\eta = 1.0, 1.5, 2.0, 2.5$ are shown. The Insertible B-Layer (IBL), which was added after the original detector commissioning, is not shown.	31
184			
185			
186			
187			
188			
189			
190	Figure 15	A computer generated three-dimensional view of the inner detector along the line of the beam axis. The subdetectors and their positions are labelled.	32
191			
192			
193	Figure 16	An alternative computer generated three-dimensional view of the inner detector transverse to the beam axis. The subdetectors and their positions are labelled.	32
194			
195			
196	Figure 17	The integrated radiation lengths traversed by a straight track at the exit of the ID envelope, including the services and thermal enclosures. The distribution is shown as a function of $ \eta $ and averaged over ϕ . The breakdown indicates the contributions of individual subdetectors, including services in their active volume.	33
197			
198			
199			
200			
201			
202	Figure 18	36
203	Figure 19	An image of the insertion of the IBL into the current pixel detector.	36
204			
205	Figure 20	A three-dimensional computer-generated image of the geometry of the IBL with a view (a) mostly transverse to the beam pipe (b) mostly parallel to the beam pipe.	37
206			
207			
208	Figure 21	An exploded view of the geometry of the silicon microstrip (SCT) double layers in the barrel region.	38
209			
210	Figure 22	39
211	Figure 23	The depth of (a) the electromagnetic barrel calorimeter in radiation lengths and (b) all calorimeters in interaction lengths as a function of pseudorapidity.	40
212			
213			
214	Figure 24	A schematic of the Liquid Argon (LAr) calorimeter in the barrel region, highlighting the accordion structure.	40
215			
216	Figure 25	A schematic of a hadronic tile module which shows the alternating layers of steel and plastic scintillator.	42
217			
218	Figure 26	The segmentation in depth and η of the tile-calorimeter modules in the central (left) and extended (right) barrels.	42
219			
220	Figure 27	A cut-away diagram of the muon systems on ATLAS	43
221	Figure 28	A quarter view of the muon spectrometer which highlights the layout of each of the detecting elements. The BOL, BML, BIL, EOL, EML, and EIL are all Monitored Drift Tube (MDT) elements, where the acronyms encode their positions.	44
222			
223			
224			
225			

226	Figure 29	45
227	Figure 30	An illustration (a) of the E/p variable used throughout this paper. The red energy deposits come from the charged particle targeted for measurement, while the blue energy deposits are from nearby neutral particles and must be subtracted. The same diagram (b) for the neutral-background selection, described in Section 8.2.3.	54
228			
229			
230			
231			
232			
233	Figure 31	The E/p distribution and ratio of simulation to data for isolated tracks with (a) $ \eta < 0.6$ and $1.2 < p/\text{GeV} < 1.8$ and (b) $ \eta < 0.6$ and $2.2 < p/\text{GeV} < 2.8$.	54
234			
235			
236	Figure 32	The fraction of tracks as a function (a, b) of momentum, (c, d) of interaction lengths with $E \leq 0$ for tracks with positive (on the left) and negative (on the right) charge.	56
237			
238			
239			
240	Figure 33	$\langle E/p \rangle_{\text{BG}}$ as a function of the track momentum for tracks with (a) $ \eta < 0.6$, (b) $0.6 < \eta < 1.1$, and as a function of the track pseudorapidity for tracks with (c) $1.2 < p/\text{GeV} < 1.8$, (d) $1.8 < p/\text{GeV} < 2.2$.	57
241			
242			
243			
244	Figure 34	$\langle E/p \rangle_{\text{COR}}$ as a function of track momentum, for tracks with (a) $ \eta < 0.6$, (b) $0.6 < \eta < 1.1$, (c) $1.8 < \eta < 1.9$, and (d) $1.9 < \eta < 2.3$.	58
245			
246			
247	Figure 35	$\langle E/p \rangle_{\text{COR}}$ calculated using LCW-calibrated topological clusters as a function of track momentum for tracks with (a) zero or more associated topological clusters or (b) one or more associated topological clusters.	59
248			
249			
250			
251	Figure 36	Comparison of the $\langle E/p \rangle_{\text{COR}}$ for tracks with (a) less than and (b) greater than 20 hits in the TRT.	60
252			
253	Figure 37	Comparison of the $\langle E/p \rangle_{\text{COR}}$ for (a) positive and (b) negative tracks as a function of track momentum for tracks with $ \eta < 0.6$.	60
254			
255			
256	Figure 38	Comparison of the E/p distributions for (a) positive and (b) negative tracks with $0.8 < p/\text{GeV} < 1.2$ and $ \eta < 0.6$, in simulation with the FTFP_BERT and QGSP_BERT physics lists.	61
257			
258			
259			
260	Figure 39	Comparison of the response of the hadronic calorimeter as a function of track momentum (a) at the EM-scale and (b) after the LCW calibration.	61
261			
262			
263	Figure 40	Comparison of the response of the EM calorimeter as a function of track momentum (a) at the EM-scale and (b) with the LCW calibration.	62
264			
265			
266	Figure 41	The reconstructed mass peaks of (a) K_S^0 , (b) Λ , and (c) $\bar{\Lambda}$ candidates.	63
267			
268	Figure 42	The E/p distribution for isolated (a) π^+ , (b) π^- , (c) proton, and (d) anti-proton tracks.	64
269			
270	Figure 43	The fraction of tracks with $E \leq 0$ for identified (a) π^+ and π^- , and (b) proton and anti-proton tracks	64
271			

272	Figure 44	The difference in $\langle E/p \rangle$ between (a) π^+ and π^- (b) p and π^+ , and (c) \bar{p} and π^-	65
273			
274	Figure 45	$\langle E/p \rangle_{\text{COR}}$ as a function of track momentum for (a) π^+ tracks and (b) π^- tracks.	66
275			
276	Figure 46	The ratio of the calorimeter response to single particles of various species to the calorimeter response to π^+ with the physics list FTFP_BERT.	66
277			
278	Figure 47	The spectra of true particles inside anti- k_t , $R = 0.4$ jets with (a) $90 < p_T/\text{GeV} < 100$, (b) $400 < p_T/\text{GeV} < 500$, and (c) $1800 < p_T/\text{GeV} < 2300$	70
280			
281	Figure 48	The jet energy scale (JES) uncertainty contributions, as well as the total JES uncertainty, as a function of jet p_T for (a) $ \eta < 0.6$ and (b) $0.6 < \eta < 1.1$	72
283			
284	Figure 49	The JES correlations as a function of jet p_T and $ \eta $ for jets in the central region of the detector.	73
286			
287	Figure 50	A schematic diagram of an R-Hadron event with a lifetime around 0.01 ns. The diagram includes one charged R-Hadron (solid blue), one neutral R-Hadron (dashed blue), Lightest Supersymmetric Particles (LSPs) (dashed green) and charged hadrons (solid orange). The pixel detector, calorimeters, and muon system are illustrated but not to scale.	79
288			
289			
290			
291			
292			
293			
294	Figure 51	A schematic diagram of an R-Hadron event with a lifetime around 4 ns. The diagram includes one charged R-Hadron (solid blue), one neutral R-Hadron (dashed blue), LSPs (dashed green) and a charged hadron (solid orange). The pixel detector, calorimeters, and muon system are illustrated but not to scale.	80
295			
296			
297			
298			
299			
300	Figure 52	A schematic diagram of an R-Hadron event with a lifetime around 5 ns. The diagram includes one charged R-Hadron (solid blue), one neutral R-Hadron (dashed blue), LSPs (dashed green) and charged hadrons (solid orange). The pixel detector, calorimeters, and muon system are illustrated but not to scale.	81
301			
302			
303			
304			
305			
306	Figure 53	A schematic diagram of an R-Hadron event with a lifetime around 20 ns. The diagram includes one charged R-Hadron (solid blue), one neutral R-Hadron (dashed blue), LSPs (dashed green) and charged hadrons (solid orange). The pixel detector, calorimeters, and muon system are illustrated but not to scale.	81
307			
308			
309			
310			
311			
312	Figure 54	A schematic diagram of an R-Hadron event with a lifetime around 20 ns. The diagram includes one charged R-Hadron (solid blue) and one neutral R-Hadron (dashed blue). The pixel detector, calorimeters, and muon system are illustrated but not to scale.	82
313			
314			
315			
316			

317	Figure 55	The distribution of (a) E_T^{miss} and (b) Calorimeter E_T^{miss} for simulated signal events before the trigger requirement.	86
318			
319			
320	Figure 56	The distribution of E_T^{miss} for data and simulated signal events, after the trigger requirement.	88
321			
322	Figure 57	The trigger efficiency for the HLT_xe70 trigger requirement as a function of (a) E_T^{miss} and (b) Calorimeter E_T^{miss} for simulated signal events.	89
323			
324			
325	Figure 58	The dependence of dE/dx on N_{split} in data after basic track hit requirements have been applied.	90
326			
327	Figure 59	The distribution of dE/dx with various selections applied in data and simulated signal events.	90
328			
329	Figure 60	The distribution of track momentum for data and simulated signal events, after previous selection requirements have been applied.	91
330			
331			
332	Figure 61	The distribution of M_T for data and simulated signal events, after previous selection requirements have been applied.	92
333			
334			
335	Figure 62	The distribution of summed tracked momentum within a cone of $\Delta R < 0.25$ around the candidate track for data and simulated signal events, after previous selection requirements have been applied.	93
336			
337			
338			
339	Figure 63	The normalized, two-dimensional distribution of E/p and f_{EM} for simulated (a) $Z \rightarrow ee$, (b) $Z \rightarrow \tau\tau$, (c) 1200 GeV Stable R-Hadron events, and (d) 1200 GeV, 10 ns R-Hadron events.	94
340			
341			
342			
343	Figure 64	Two-dimensional distribution of dE/dx versus charge signed momentum (qp) for minimum-bias tracks. The fitted distributions of the most probable values for pions, kaons and protons are superimposed.	95
344			
345			
346			
347	Figure 65	The distribution of mass estimated using dE/dx for simulated stable R-Hadrons with masses between 1000 and 1600 GeV.	96
348			
349			
350	Figure 66	The acceptance \times efficiency as a function of R-Hadron (a) mass and (b) lifetime. (a) shows all of the combinations of mass and lifetime considered in this search, and (b) highlights the lifetime dependence for 1000 GeV and 1600 GeV R-Hadrons.	98
351			
352			
353			
354			
355	Figure 67	The distribution of (a) dE/dx and (b) momentum for tracks in data and simulated signal after requiring the event level selection and the track selection on p_T , hits, and N_{split} . Each sub-figure shows the normalized distributions for tracks classified as hadrons, electrons, and muons in data and R-Hadrons in the simulated signal.	100
356			
357			
358			
359			
360			
361			

362	Figure 68	The distribution of $M_{dE/dx}$ (a) before and (b) after the ionization requirement for tracks in simulated W boson decays and for the randomly generated background estimate.	102
363			
364			
365			
366	Figure 69	The distribution of $M_{dE/dx}$ (a) before and (b) after the ionization requirement for tracks in the validation region and for the randomly generated background estimate.	103
367			
368			
369			
370	Figure 70	The trigger efficiency for the HLT_xe70 trigger requirement as a function of Calorimeter E_T^{miss} for simulated data events with a W boson selection. Simulated signal events and simulated W boson events are also included.	108
371			
372			
373			
374			
375	Figure 71	The efficiency of the muon veto for R-hadrons of two different masses, as a function of $\frac{1}{\beta}$ for simulated R-Hadron tracks.	110
376			
377			
378	Figure 72	The average reconstructed MDT β distribution for $Z \rightarrow \mu\mu$ events in which one of the muons is reconstructed as a slow muon, for both data and simulation. A gaussian fit is superimposed.	111
379			
380			
381			
382	Figure 73	The observed mass distribution of events in data and the generated background distribution in (a) the stable and (b) the metastable signal region. A few example simulated signal distributions are superimposed.	112
383			
384			
385			
386	Figure 74	The observed and expected cross section limits as a function of mass for the stable simulated signal. The predicted cross section values for the corresponding signals are included.	115
387			
388			
389			
390	Figure 75	The observed and expected cross section limits as a function of mass for each generated lifetime. The predicted cross section values for the corresponding signals are included.	116
391			
392			
393			
394	Figure 76	The excluded range of masses as a function of gluino lifetime. The expected lower limit (LL), with its experimental $\pm 1\sigma$ band, is given with respect to the nominal theoretical cross-section. The observed 95% LL obtained at $\sqrt{s} = 8$ TeV [63] is also shown for comparison.	118
395			
396			
397			
398			
399	Figure 77	The constraints on the gluino mass as a function of lifetime for a split-supersymmetry model with the gluino R-Hadrons decaying into a gluon or light quarks and a neutralino with mass of 100 GeV. The solid lines indicate the observed limits, while the dashed lines indicate the expected limits. The area below the curves is excluded. The dots represent results for which the particle is assumed to be prompt or stable.	119
400			
401			
402			
403			
404			
405			
406			

407 LIST OF TABLES

408 Table 1	The design parameters of the LHC beam that determines the energy of collisions and the luminosity, for both the injection of protons and at the nominal circulation.	22
412 Table 2	The performance goals for each of the subsystems of the ATLAS detector. The $ \eta $ coverage specifies the range where the subsystem needs to be able to provide measurements with the specified resolution. The resolutions include a p_T or E dependence that is added in quadrature with a p_T/E independent piece.	27
418 Table 3	A summary of the parameters of the inner detector and each of the subdetectors [3].	34
420 Table 4	A summary of the expected performance of the combined inner detector [8]. Included are the reconstruction efficiencies for multiple particle types as well as the momentum and impact parameter (IP) resolution for various momenta.	35
425 Table 5	The dominant sources of corrections and systematic uncertainties in the JES estimation technique, including typical values for the correcting shift (Δ) and the associated uncertainty (σ).	71
429 Table 6	The expected number of events at each level of the selection for metastable 1600 GeV, 10 ns R-Hadrons, along with the number of events observed in data, for 3.2 fb^{-1} . The simulated yields are shown with statistical uncertainties only. The total efficiency \times acceptance is also shown for the signal.	97
435 Table 7	A summary of the sources of systematic uncertainty for the data-driven background in the signal region. If the uncertainty depends on the mass, the maximum values are reported.	105
439 Table 8	A summary of the sources of systematic uncertainty for the simulated signal yield. The uncertainty depends on the mass and lifetime, and the maximum negative and positive values are reported in the table.	107
443 Table 9	Example of the contributing systematic variations to the total systematic for the E_T^{miss} Scale, as measured in a 1200 GeV, Stable R-Hadron signal sample.	109

446	Table 10	The estimated number of background events and the number of observed events in data for the specified selection regions prior to the requirement on mass. The background estimates show statistical and systematic uncertainties.	112
447			
448			
449			
450			
451	Table 11	The left and right extremum of the mass window for each generated mass point with a 10 ns lifetime.	113
452			
453	Table 12	The left and right extremum of the mass window used for each generated stable mass point.	113
454			
455	Table 13	The expected number of signal events, the expected number of background events, and the observed number of events in data with their respective statistical errors within the respective mass window for each generated stable mass point.	114
456			
457			
458			
459			
460	Table 14	The expected number of signal events, the expected number of background events, and the observed number of events in data with their respective statistical errors within the respective mass window for each generated mass point with a lifetime of 10 ns.	114
461			
462			
463			
464			
465	Table 15	The observed and expected 95% CL lower limit on mass for gluino R-Hadrons for each considered lifetime.	117
466			
467	Table 16	The left and right extremum of the mass window for each generated mass point with a 50 ns lifetime.	129
468			
469	Table 17	The left and right extremum of the mass window for each generated mass point with a 30 ns lifetime.	129
470			
471	Table 18	The left and right extremum of the mass window for each generated mass point with a 10 ns lifetime.	130
472			
473	Table 19	The left and right extremum of the mass window used for each generated mass point with a lifetime of 3 ns.	130
474			
475	Table 20	The left and right extremum of the mass window used for each mass point with a lifetime of 1 ns.	130
476			
477	Table 21	The left and right extremum of the mass window for each generated mass point with a lifetime of 0.4 ns.	131
478			
479	Table 22	The left and right extremum of the mass window used for each generated stable mass point.	131
480			
481	Table 23	The expected number of signal events, the expected number of background events, and the observed number of events in data with their respective statistical errors within the respective mass window for each generated mass point with a lifetime of 50 ns.	131
482			
483			
484			
485			
486	Table 24	The expected number of signal events, the expected number of background events, and the observed number of events in data with their respective statistical errors within the respective mass window for each generated mass point with a lifetime of 30 ns.	132
487			
488			
489			
490			

491	Table 25	The expected number of signal events, the expected number of background events, and the observed number of events in data with their respective statistical errors within the respective mass window for each generated mass point with a lifetime of 10 ns.	132
492			
493			
494			
495			
496	Table 26	The expected number of signal events, the expected number of background events, and the observed number of events in data with their respective statistical errors within the respective mass window for each generated mass point with a lifetime of 3 ns.	133
497			
498			
499			
500			
501	Table 27	The expected number of signal events, the expected number of background events, and the observed number of events in data with their respective statistical errors within the respective mass window for each generated mass point with a lifetime of 1 ns.	133
502			
503			
504			
505			
506	Table 28	The expected number of signal events, the expected number of background events, and the observed number of events in data with their respective statistical errors within the respective mass window for each generated mass point with a lifetime of p4 ns.	134
507			
508			
509			
510			
511	Table 29	The expected number of signal events, the expected number of background events, and the observed number of events in data with their respective statistical errors within the respective mass window for each generated stable mass point	134
512			
513			
514			
515			

517 ACRONYMS

- 518 SM Standard Model
519 CERN European Organization for Nuclear Research
520 SUSY Supersymmetry
521 LSP Lightest Supersymmetric Particle
522 LHC Large Hadron Collider
523 ATLAS A Toroidal LHC ApparatuS
524 CMS Compact Muon Solenoid
525 ALICE A Large Ion Collider Experiment
526 LHCb Large Hadron Collider beauty experiment
527 LEP the Large Electron Positron collider
528 PS Proton Synchrotron
529 PSB Proton Synchrotron Booster
530 SPS Super Proton Synchrotron
531 SCT silicon microstrip
532 TRT transition radiation tracker
533 LAr Liquid Argon
534 EM electromagnetic
535 RPC Resistive Plate Chamber
536 TGC Thin Gap Chamber
537 MDT Monitored Drift Tube
538 CSC Cathode Strip Chamber
539 ToT time over threshold
540 LCW local cluster weighted
541 MIP minimally ionizing particle
542 IP impact parameter
543 EPJC European Physical Journal C

- 544 JES jet energy scale
545 LLP Long-Lived Particle
546 CR Control Region
547 NLO next-to-leading order
548 NLL next-to-leading logarithmic
549 PDF parton distribution function
550 ISR initial state radiation
551 RMS root mean square
552 IBL Insertible B-Layer
553 CP Combined Performance
554 MDT Monitored Drift Tube
555 RF radiofrequency

556

PART I

557

INTRODUCTION

558

You can put some informational part preamble text here.

1

559

560 INTRODUCTION

561

PART II

562

THEORETICAL CONTEXT

563

You can put some informational part preamble text here.

2

564

565 STANDARD MODEL

566 The SM of particle physics seeks to explain the symmetries and interactions of
567 all currently discovered fundamental particles. It has been tested by several genera-
568 tions of experiments and has been remarkably successful, no significant de-
569 viations have been found. The SM provides predictions in particle physics for
570 interactions up to the Planck scale (10^{15} - 10^{19} GeV).

571 The theory itself is a quantum field theory grown from an underlying $SU(3) \times$
572 $SU(2) \times U(1)$ that requires the particle content and quantum numbers consist-
573 ent with experimental observations (see Section 2.1). Each postulated symme-
574 try is accompanied by an interaction between particles through gauge invari-
575 ance. These interactions are referred to as the Strong, Weak, and Electromag-
576 netic forces, which are discussed in Section 2.2.

577 Although this model has been very predictive, the theory is incomplete; for
578 example, it is not able to describe gravity or astronomically observed dark matter.
579 These limitations are discussed in more detail in Section 2.3.

580 21 PARTICLES

581 The most familiar matter in the universe is made up of protons, neutrons, and
582 electrons. Protons and neutrons are composite particles, however, and are made
583 up in turn by particles called quarks. Quarks carry both electric charge and color
584 charge, and are bound in color-neutral combinations called baryons. The elec-
585 tron is an example of a lepton, and carries only electric charge. Another type
586 of particle, the neutrino, does not form atomic structures in the same way that
587 quarks and leptons do because it carries no color or electric charge. Collectively,
588 these types of particles are known as fermions, the group of particles with half-
589 integer spin.

590 There are three generations of fermions, although familiar matter is formed
591 predominantly by the first generation. The generations are identical except for
592 their masses, which increase in each generation by convention. In addition, each
593 of these particles is accompanied by an antiparticle, with opposite-sign quantum
594 numbers but the same mass.

595 The fermions comprise what is typically considered matter, but there are
596 additional particles that are mediators of interactions between those fermions.
597 These mediators are known as the gauge bosons, gauge in that their existence
598 is required by gauge invariance (discussed further in Section 2.2) and bosons in
599 that they have integer spin. The boson which mediates the electromagnetic force
600 is the photon, the first boson to be discovered; it has no electric charge, no mass,
601 and a spin of 1. There are three spin-1 mediators of the weak force, the two
602 W bosons and the Z boson. The W bosons have electric charge of ± 1 and a
603 mass of 80.385 ± 0.015 GeV, while the Z boson is neutral and has a mass of

604 91.1876 \pm 0.0021 GeV. The strong force is mediated by eight particles called
 605 gluons, which are massless and electrically neutral but do carry color charge.

606 The final particle present in the SM is the Higgs boson, which was recently
 607 observed for the first time by experiments at CERN in 2012. It is electrically
 608 neutral, has a mass of 125.7 \pm 0.4 GeV, and is the only spin-0 particle yet to be
 609 observed. The Higgs boson is the gauge boson associated with the mechanism
 610 that gives a mass to the W and Z bosons.

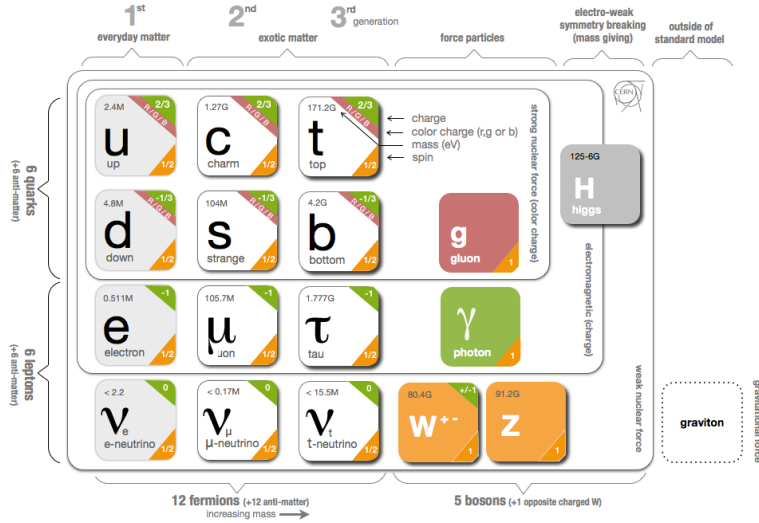


Figure 1: The particle content of the SM.

611 Together these particles form the entire content of the SM, and are summa-
 612 rized in Figure 1. These are the particles that constitute the observable universe
 613 and all the so-far-observed interactions within it.

614 2.2 INTERACTIONS

615 The interactions predicted and described by the SM are fundamentally tied to the
 616 particles within it, both in that they describe the way those particles can influence
 617 each other and also in that the existence of the interactions requires the existence
 618 of some particles (the gauge bosons).

619 2.3 LIMITATIONS

3

620

621 SUPERSYMMETRY

622 3.1 MOTIVATION

623 3.2 STRUCTURE

624 3.3 PHENOMENOLOGY

4

625

626 LONG-LIVED PARTICLES

627 4.1 MECHANISMS

628 4.1.1 EXAMPLES IN SUPERSYMMETRY

629 4.2 PHENOMENOLOGY

630 4.2.1 DISIMILARITIES TO PROMPT DECAYS

631 4.2.2 CHARACTERISTIC SIGNATURES

632

PART III

633

EXPERIMENTAL STRUCTURE AND RECONSTRUCTION

634

You can put some informational part preamble text here.

635

636 THE LARGE HADRON COLLIDER

637 The LHC, a two-ring superconducting hadron accelerator, provides high energy
638 proton-proton collisions for several large experiments at European Organization
639 for Nuclear Research (CERN) in Geneva, Switzerland [1, 2]. It is the largest,
640 highest-luminosity, and highest-energy proton collider ever built, and was con-
641 structed by a collaboration of more than 10,000 scientists from the more than
642 100 countries that contribute to CERN. The original design of the LHC focused on
643 providing collision energies of up to 14 TeV and generating enough collisions to
644 reveal physics beyond the SM which is predicted to exist at higher energy scales.

645 The LHC was installed in an existing 27 km tunnel at CERN which was origi-
646 nally designed to house the Large Electron Positron collider (LEP). This allows
647 the collider to use existing accelerators at the same complex to provide the initial
648 acceleration of protons up to 450 GeV before injecting into LHC. The injected
649 hadrons are accelerated up to as much as 14 TeV while being focused into two
650 beams traveling in opposite directions. During this process the protons circulate
651 around the tunnel millions of times, while the beams are intermittently crossed
652 at the four locations of the experiments to provide collisions. These collision
653 points correspond to the four major LHC experiments: ATLAS, Compact Muon
654 Solenoid (CMS), Large Hadron Collider beauty experiment (LHCb), and A Large
655 Ion Collider Experiment (ALICE), and Figure 2 shows the layout of the exper-
656 iments both on the surface and below. ATLAS and CMS are both general pur-
657 pose, high-luminosity detectors which search for a wide range of new types of
658 physics [3, 4]. LHCb studies the interactions of b-hadrons to explore the asymme-
659 try between matter and antimatter [5]. ALICE focuses on the collisions of lead
660 ions, which the LHC also provides, in order to study the properties of quark-
661 gluon plasma [6].

662 During the first five years of operation, after the LHC turned on in 2010, the
663 LHC has provided four major data collecting periods. In 2010 the LHC generated
664 collisions at several energies, starting at 900 GeV. It increased the energy from
665 900 GeV to 2.76 TeV and then subsequently to 7 TeV, with a peak luminos-
666 ity of $2 \times 10^{32} \text{ cm}^{-2}\text{s}^{-1}$, and a total delivered luminosity of 50 pb^{-1} . The next
667 run, during 2011, continued the operation at 7 TeV and provided an additional 5 fb^{-1}
668 with a peak luminosity of $4 \times 10^{33} \text{ cm}^{-2}\text{s}^{-1}$. The energy was then increased
669 to 8 TeV for the data collection during 2012, which provided 23 fb^{-1} with a peak
670 luminosity of $7.7 \times 10^{33} \text{ cm}^{-2}\text{s}^{-1}$. After the first long shutdown for 2013 and
671 2014, the LHC resumed operation and increased the energy to 13 TeV in 2015,
672 where it delivered 4.2 fb^{-1} with a peak luminosity of $5.5 \times 10^{33} \text{ cm}^{-2}\text{s}^{-1}$. The
673 LHC is currently providing additional 13 TeV collisions in 2016 with higher lu-
674 minosities than during any previous data collection periods. These running peri-
675 ods are summarized in Figure 3, which shows the total delivered luminosity over

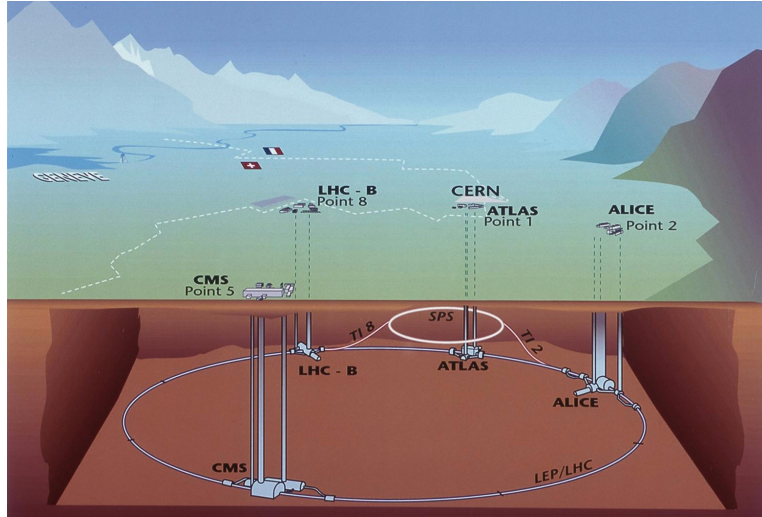


Figure 2: The four collision points and corresponding experiments of the [LHC](#). The image includes the location of the nearby city of Geneva as well as the border of France and Switzerland.

676 time for the [ATLAS](#) experiment during each of the four years of data collection
677 since 2011.

678 5.1 INJECTION CHAIN

679 The [LHC](#) takes advantage of the presence of previously built accelerators at [CERN](#)
680 to work up to the target energy in consecutive stages. The series of accelerators
681 that feed into the [LHC](#) are known collectively as the injection chain, and together
682 with the [LHC](#) form the accelerator complex. The full complex is illustrated in
683 Figure 4, which details the complex series required to reach collisions of 13 or
684 14 TeV.

685 Protons at the [LHC](#) begin as hydrogen atoms in the Linac 2, a linear accelerator
686 which replaced Linac 1 as the primary proton accelerator at CERN in 1978. In
687 Linac 2, the hydrogen atoms are stripped of their electrons by a strong magnetic
688 field, and the resulting protons are accelerated up to 50 MeV by cylindrical con-
689 ductors charged by radio frequency cavities. The protons are then transferred
690 to the Proton Synchrotron Booster ([PSB](#)), which uses a stack of four synchrotron
691 rings to accelerate the protons up to 1.4 GeV. Then the protons are injected
692 into the Proton Synchrotron ([PS](#)) which again uses synchrotron rings to bring
693 the energy up to 25 GeV. The intermediate step between Linac 2 and the [PS](#) is
694 not directly necessary, as the [PS](#) can accelerate protons starting from as low as
695 50 MeV. The inclusion of the [PSB](#) allows the [PS](#) to accept a higher intensity of
696 injection and so increases the deliverable luminosity in the [LHC](#). The penulti-
697 mate stage of acceleration is provided by the Super Proton Synchrotron ([SPS](#)), a
698 large synchrotron with a 7 km circumference that was commissioned at CERN
699 in 1976. During this step the protons increase in energy to 450 GeV, after which
700 they can be directly injected into the [LHC](#).

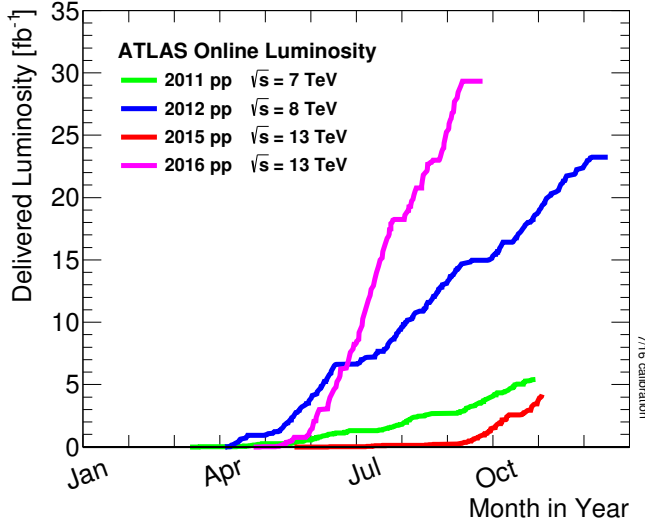


Figure 3: The cumulative luminosity over time delivered to the [ATLAS](#) experiment from high energy proton-proton collisions since 2011. The energies of the collisions are listed for each of the data-taking periods.

The final step is the [LHC](#) itself, which receives protons from the [SPS](#) into two separate beam pipes which circulate in opposite directions. The filling process at this steps takes approximately 4 minutes, and the subsequent acceleration to the final energy (6.5 TeV during 2015 and up to 7 TeV by design) takes approximately half an hour. At this point the protons circulate around the circumference tens of thousands of times a second and continue for up to two hours.

5.2 DESIGN

5.2.1 LAYOUT

Many of the aspects of the [LHC](#) design are driven by the use of the existing [LEP](#) tunnel. This tunnel slopes gradually, with a 1.4% decline, with 90% of its length built into molasse rock which is particularly well suited to the application. The circumference is composed of eight 2987 meter arcs and eight 528 meter straight sections which connect them; this configuration is illustrated in Figure 5. The tunnel diameter is 3.7 m throughout its length.

The design energy is directly limited by the size of this tunnel, with its radius of curvature of 2804 m. A significant magnetic field is required to curve the protons around that radius of curvature; the relationship is given by

$$p \simeq 0.3BR \quad (1)$$

where p is the momentum of the particle in GeV, B is the magnetic field in Tesla, and R is the radius of curvature in meters. From the target design energy of 14 TeV, or 7 TeV of momentum for protons in each beam, the required magnetic field is 8.33 Tesla. This is too large a field strength to be practical with

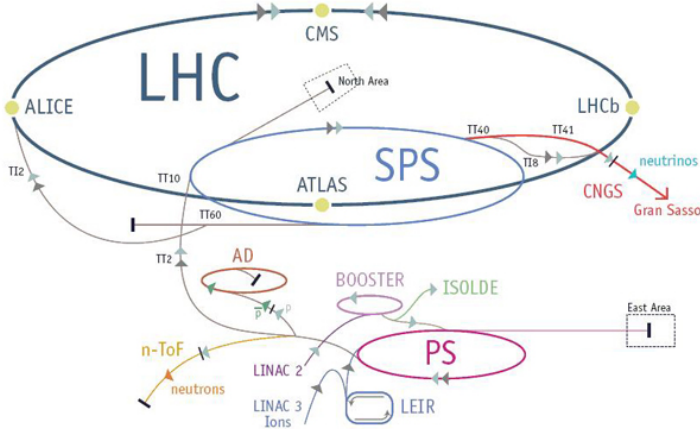


Figure 4: The accelerator complex that builds up to the full design energies at the [LHC](#). The protons are passed in order to Linac 2, the [PSB](#), the [PS](#), the [SPS](#) and then the [LHC](#).

722 iron electromagnets, because of the enormous power required and the resulting
 723 requirements for cooling. Because of these constraints, the [LHC](#) uses supercon-
 724 ducting magnets which can maintain that field strength with significantly less
 725 power consumption.

726 5.2.2 MAGNETS

727 Specifically the magnets chosen were Niobium and Titanium (NbTi) which al-
 728 low for field strengths as high as 10 Tesla when cooled down to 1.9 K. Reaching
 729 the target temperature of 1.9 K for all of the magnets requires superfluid helium
 730 and a large cryogenic system along the entire length of the tunnel. During nor-
 731 mal operation, the [LHC](#) uses 120 tonnes of helium within the magnets, and the
 732 entire system is cooled by eight cryogenic helium refrigerators. The tempera-
 733 ture increase that occurs during transit from the refrigerator along the beam
 734 necessitates that the refrigerators cool the helium down to 1.8 K. Any significant
 735 increase above this temperature range can remove the superconductive proper-
 736 ties of the magnets, which in turn generates drastically larger heat losses from
 737 the current within the magnets and causes a rapid rise in temperature called a
 738 quench.

739 In all there are approximately 8000 superconducting magnets distributed around
 740 the [LHC](#). The 1232 bending magnets, which keep the protons curving along the
 741 length of the beam, are twin bore cryodipoles, which allow both proton beams
 742 to be accommodated by one magnet and all of the associated cooling structure.
 743 Figure 6 shows the cross section of the design for these dipoles. The magnets are
 744 very large, 16.5 m long with a diameter of 0.57 meters and a total weight of 28
 745 tonnes. They are slightly curved, with an angle of 5.1 mrad, in order to carefully
 746 match the beam path. The twin bore accommodates both magnets inside the
 747 two 5 cm diameter holes which are surrounded by the superconducting coils.
 748 The coils require 12 kA of current in order to produce the required magnetic

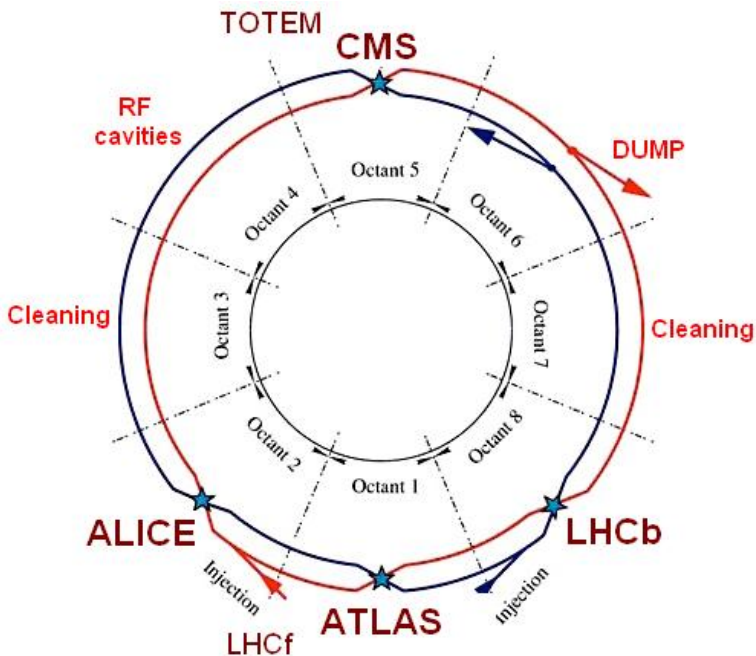


Figure 5: A schematic of the layout of the LHC, not to scale. The arched and straight sections are illustrated at the bottom of the schematic, and all four crossing sites are indicated with their respective experiments.

749 field. These coils are comprised of NbTi cable wound in two layers; the wire in
 750 the inner layer has a diameter of 1.065 mm while the wire in the outer layer has
 751 a diameter of 0.825 mm.

752 The large currents in the wires, along with the magnetic field produced, result
 753 in forces on the magnets which would tend to push them apart with over 10,000
 754 Newtons per meter. Constraining the magnets requires a significant amount of
 755 structure including non-magnetic stainless steel collars. Both the presence of
 756 these electromagnetic forces and the varying thermal contraction coefficient of
 757 the pieces of the magnet produce significant forces on the cold mass structure.
 758 The cold mass is carefully engineered to so that these stresses do not significantly
 759 alter the magnetic field shape, which must be maintained between magnets to a
 760 precision of approximately 10^{-4} for successful operation.

761 The remaining 6800 magnets are a variety of quadrupole, sextapole, octopole,
 762 and single bore dipole magnets. These are used to damp oscillations, correct
 763 beam trajectories, focus the beams during circulation, and to squeeze the beams
 764 before collisions.

765 5.2.3 RF CAVITIES

766 Sixteen RF cavities produce the actual acceleration of the proton beam up to the
 767 design energy. These RF cavities are tuned to operate at 400 MHz, and are pow-
 768 ered by high-powered electron beams modulated at the same frequency, called
 769 klystrons. The resonance within the cavity with the oscillating electric field
 770 establishes a voltage differential of 2 MV per cavity. The sixteen cavities are

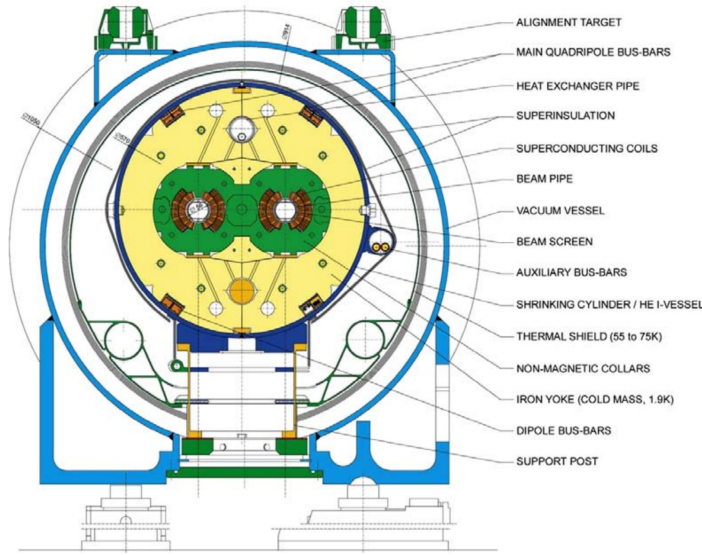


Figure 6: A cross section of the cryodipole magnets which bend the flight path of protons around the circumference of the LHC. The diagram includes both the superconducting coils which produce the magnetic field and the structural elements which keep the magnets precisely aligned.

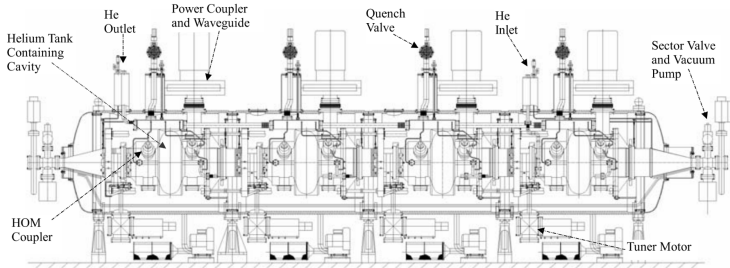


Figure 7: The arrangement of four RF cavities within a cryomodule.

771 split between the two beams, so combined the cavities provide 16 MV per beam,
 772 which accelerate the protons on each consecutive pass through the cavity. This
 773 acceleration is also necessary during circulation even after the target energy has
 774 been reached in order to compensate for losses from synchrotron radiation.

775 The cavities are arranged in cryomodules which contain four cavities, with
 776 two cryomodules per beam; this arrangement is illustrated in Figure 7. These
 777 cryomodules are necessary to maintain the superconducting state of the cavities,
 778 which are also constructed from niobium. The RF cavities use niobium along
 779 with copper to allow for low power losses in the superconductors. The copper
 780 provides a reduced susceptibility to quenching, as it rapidly conducts away heat
 781 generated by imperfections in the niobium, as well as natural shielding from the
 782 earth's magnetic field which can interfere with the RF system.

783 The nature of the radio frequency oscillations tends to group protons together
 784 into buckets. A proton traveling exactly in phase with the RF oscillations will not
 785 be displaced at all during a single circulation, and those slightly ahead or behind

786 of that phase will slightly decelerate or accelerate, respectively. This produces
 787 separate clusters of protons which arrive in phase to the cavities every 2.5 ns,
 788 corresponding to the 400 MHz frequency.

789 5.2.4 BEAM

790 The beams of protons circulate within 54 km of 5 cm diameter beam pipe. This
 791 entire structure is kept under vacuum at 1.9 K to prevent interactions between
 792 the beam pipe and the magnets as well as to prevent any interactions between the
 793 circulating protons and gas in the pipe. The vacuum within the pipe establishes
 794 a pressure as low as 10^{-9} mbar before the protons are introduced.

795 Because of the very high energies of the circulating protons, synchrotron ra-
 796 diation is not negligible in the bending regions. The protons are expected to
 797 radiate 3.9 kW per beam at 14 TeV, with 0.22 W/m, which is enough power to
 798 heat the liquid helium and cause a quench were it absorbed by the magnets. To
 799 prevent this, a copper screen is placed within the vacuum tube that absorb the
 800 emitted photons. This screen is kept between 5 and 20 K by the liquid helium
 801 cooling system.

802 5.3 LUMINOSITY PARAMETERS

803 In addition to the high energy of the collisions, the rate of collisions is extremely
 804 important to enabling the discovery of new physics. Many measurements and
 805 searches require a large number of events in order to be able to make statistically
 806 significant conclusions. The rate of collisions is measured using luminosity, the
 807 number of collisions per unit time and unit cross section for the proton-proton
 808 collisions. From the beam parameters, luminosity is given by

$$\mathcal{L} = \frac{N_b^2 n_b f_{rev} \gamma}{4\pi\epsilon_n \beta^*} F \quad (2)$$

809 where N_b is the number of protons per bunch, n_b is the number of bunches per
 810 beam, f_{rev} is the frequency of revolution, γ is the Lorentz factor for the protons
 811 at the circulating energy, ϵ_n is the emittance, β^* is the amplitude function at the
 812 collision point, and F is a geometric factor that accounts for the crossing angle of
 813 the beams at the collision point. The emittance measures the average spread of
 814 particles in both position and momentum space, while the amplitude function
 815 is a beam parameter which measures how much the beam has been squeezed.
 816 Together ϵ_n and β^* give the size of the beam in the transverse direction, $\sigma =$
 817 $\sqrt{\epsilon\beta^*}$. β changes over the length of the beam as the accessory magnets shape the
 818 distribution of protons, but only the value at the point of collisions, β^* , affects
 819 the luminosity.

820 The luminosity is maximized to the extent possible by tuning the parameters
 821 in Equation 2. A number of these are constrained by the design decisions. The
 822 revolution frequency is determined entirely by the length of the tunnel, as the

Parameter	Unit	Injection	Nominal
Beam Energy	TeV	0.450	7
Peak Instantaneous Luminosity	$\text{cm}^{-2}\text{s}^{-1}$	-	10^{34}
Bunch Spacing	ns	25	25
Number of Filled Bunches	-	2808	2808
Normalized Transverse Emittance	μm	3.75	3.75
Frequency	MHz	400.789	400.790
RF Voltage/Beam	MV	8	16
Stored Energy	MJ	-	362
Magnetic Field	T	0.54	8.33
Operating Temperature	K	1.9	1.9

Table 1: The design parameters of the [LHC](#) beam that determines the energy of collisions and the luminosity, for both the injection of protons and at the nominal circulation.

823 protons travel at very close to the speed of light. The geometric factor F is de-
 824 termined by the crossing angle of the beams at the collision points, again a com-
 825 ponent of the tunnel design; this angle is already very small at $285 \mu\text{rad}$, which
 826 helps to maximize the geometric factor.

827 The major pieces that can be adjusted are the number of protons per bunch,
 828 N_b , the number of bunches in the beam, n_b , and the amplitude function β . In-
 829 creasing either N_b or n_b increases the amount of energy stored in the beam,
 830 which presents a danger if control of the beam is lost. At design specifications,
 831 the beam stores 362 MJ, which is enough energy to damage the detectors or ac-
 832 celerator if the beam were to wander out of the beam pipe. So, the luminosity
 833 is primarily controlled at the [LHC](#) by adjusting β^* , where lowering β^* increases
 834 the luminosity. β^* is tuned to provide the various values of luminosity used at
 835 the [LHC](#) which can be raised to as much as 10^{34} .

836 The nominal bunch structure consists of 3654 bunches, each holding 10^{11} pro-
 837 tons, which cross a collision point in 25 ns. These are further subdivided into the
 838 buckets mentioned in Section 5.2.3 by the clustering properties of the [RF](#) cavities.
 839 The bunches are further grouped into trains of 72 bunches which are separated
 840 by a gap which would otherwise hold 12 bunches. At nominal operation 2808
 841 of the bunches will actually be filled with protons, while the remainder are left
 842 empty to form an abort gap that can be used in case the beam needs to be dumped.

843 The various beam parameters are summarized in Table 1 for the designed op-
 844 eration. In practice the beam has operated at lower energies and lower luminosi-
 845 ties than the design values, but the [LHC](#) is expected to operate at the full design
 846 values during Run 2.

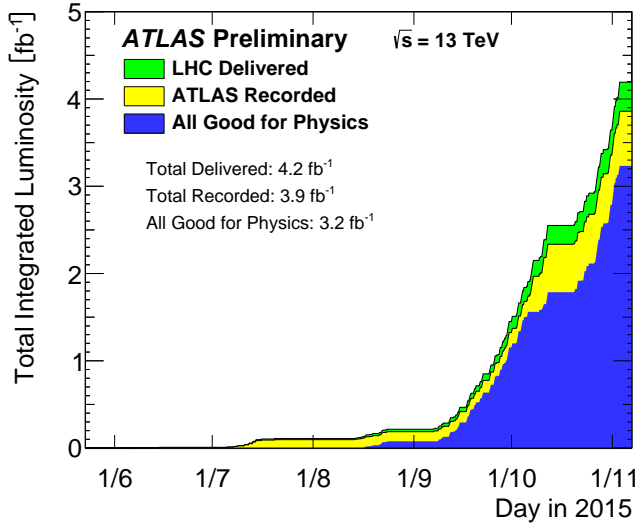


Figure 8: The cumulative luminosity versus time delivered to ATLAS (green), recorded by ATLAS (yellow), and certified to be good quality data (blue) during stable beams for pp collisions at 13 TeV in 2015.

5.4 DELIVERED LUMINOSITY

During the data collection of 2015, the [LHC](#) operated at luminosities as large as 5×10^{33} . It is convenient to refer to the integrated luminosity, the integral of the instantaneous luminosity, which corresponds directly to the number of delivered events for a given process.

$$N = \sigma \times \int \mathcal{L}(t) dt$$

where σ is the cross section for the process of interest. The integrated luminosity over time is shown in Figure 8. This includes the luminosity delivered by the [LHC](#) as well as the luminosity that was recorded by [ATLAS](#). Some of the delivered luminosity is not recorded because [ATLAS](#) is placed in standby until the [LHC](#) reports that the beam conditions are stable, and only then does [ATLAS](#) begin recording. The figure also includes the amount of luminosity marked as good for physics, which includes additional requirements on the operation of the detector during data collection that are necessary for precise measurements.

In addition to the instantaneous luminosity, the beam conditions also influence the number of collisions that occur within a single bunch crossing. The multiple interactions at each crossing are referred to as pileup, often denoted μ , and each of these interactions are present in a single measured event. Figure 9 shows the luminosity-weighted distribution of the mean number of interactions for events collected in 2015. The presence of as many as 20 events in a single collision provides a significant challenge in reconstructing events and isolating the targeted physical processes.

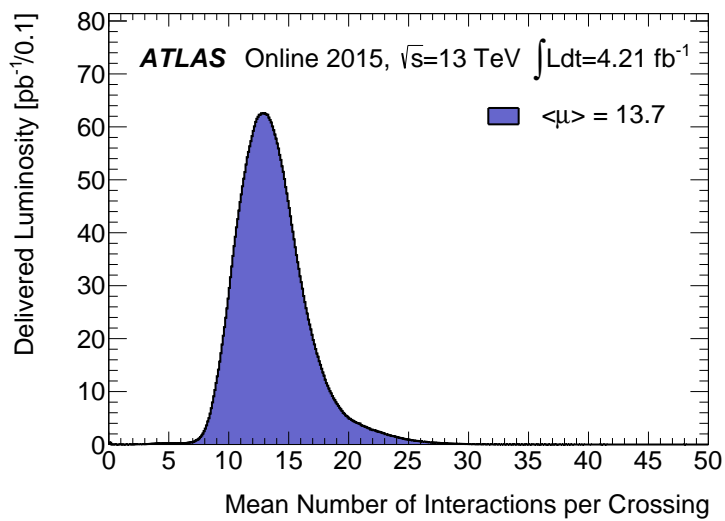


Figure 9: The luminosity-weighted distribution of the mean number of interactions per crossing for the 2015 pp collision data at 13 TeV.

865 THE ATLAS DETECTOR

866 The four major LHC experiments at CERN seek to use the never before matched
867 energies and luminosities of the new collider to explore the boundaries of par-
868 ticle physics and to gain insight into the fundamental forces of nature. Two of
869 these experiments, ATLAS and CMS, are general purpose detectors that seek to
870 measure a variety of processes in the up to 14 TeV proton-proton collisions that
871 occur as much as 40 million times per second at the LHC at the design luminosity
872 of $10^{34} \text{ cm}^{-2}\text{s}^{-1}$. ATLAS employs a hermetic detector design, one which encloses
873 the particle collisions as completely as possible with detecting elements, that al-
874 lows it to study a wide range of physics from SM and Higgs measurements to
875 searches for new physics in models like Supersymmetry [3].

876 Accomodating this wide variety of goals is a challenge for the design of the
877 detector. The wide range of energies involved requires high measurement preci-
878 sion over several orders of magnitude and the ability to measure a variety of par-
879 ticle types. At the time of the construction of ATLAS, the Higgs boson had yet to be
880 discovered, but the diphoton decay mode was (correctly) expected to be impor-
881 tant and necessitated a high resolution photon measurement. The potential for
882 decays of new heavy gauge bosons, W' and Z', required a similarly high momen-
883 tum resolution for leptons with momentum up to several TeV. Hadronic decay
884 modes of several possible new high energy particles could result in very energetic
885 jets, again up to several TeV, and reconstructing the decay resonances would
886 again require good energy resolution. Several models, such as Supersymmetry
887 (SUSY) or Extra Dimensions, predict the existence of particles which would not
888 interact with traditional detecting elements. However these particles can still be
889 observed in a hermetic detector by accurately measuring the remaining event
890 constituents to observe an imbalance in energy called missing energy or E_T^{miss} .
891 Measuring E_T^{miss} implicitly requires a good resolution on all SM particles that can
892 be produced. And at the lower end of the energy spectrum, precision SM mea-
893 surements would require good resolution of a variety of particle types at energies
894 as low as a few GeV, so the design needs to accomodate roughly three orders of
895 magnitude.

896 This broad spectrum of measurements requires a variety of detector systems
897 working together to form a cohesive picture of each collision. Two large magnet
898 systems provide magnetic fields that provide a curvature to the propagation of
899 charged particles and allows for precision momentum measurements by other
900 systems. The inner detector uses a combination of tracking technologies to re-
901 construct particle trajectories and vertexes for charged particles. A variety of
902 calorimeters measure the energies of hadrons, electrons, and photons over a
903 large solid angle. A large muon spectrometer identifies muons and uses the sec-
904 ond magnet system to provide an independent measurement of their momentum

905 from the inner detector and improve the resolution. The layout of all of these
 906 systems is shown in Figure 10.

907 The performance goals needed to achieve the various targeted measurements
 908 and searches discussed above can be summarized as resolution and coverage re-
 909 quirements on each of these systems. Those requirements are listed in Table 2.

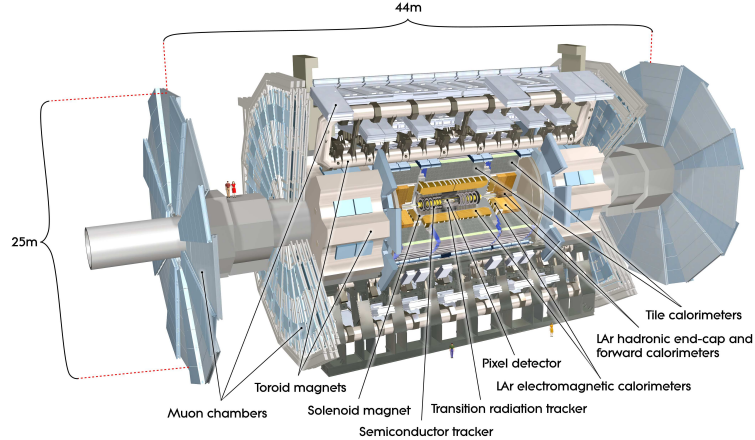


Figure 10: A cut-away schematic of the layout of the [ATLAS](#) detector. Each of the major subsystems is indicated.

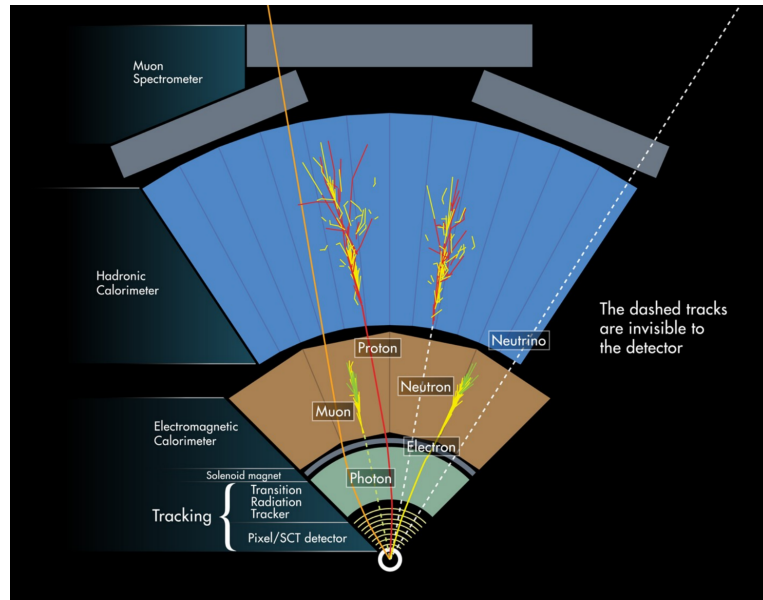


Figure 11: A cross-sectional slice of the [ATLAS](#) experiment which illustrates how the various SM particles interact with the detector systems.

910 Incorporating these various pieces into a single detector is a significant tech-
 911 nical challenge. The resulting detector has a diameter of 22 m, is 46 m long,
 912 and weighs 7,000 tons; it is the largest volume particle detector ever constructed.
 913 The various detector elements need to be constructed and assembled with preci-
 914 sions as low as micrometers. These systems all need to function well even after
 915 exposure to the significant radiation dose from the collisions. Designing, con-

Detector Component	Required Resolution	$ \eta $ Coverage	
		Measurement	Trigger
Tracking	$\sigma_{p_T}/p_T = 0.05\% p_T + 1\%$	2.5	-
EM Calorimetry	$\sigma_E/E = 10\%/\sqrt{E} + 0.7\%$	3.2	2.5
Hadronic Calorimetry			
Barrel and Endcap	$\sigma_E/E = 50\%/\sqrt{E} + 3\%$	3.2	3.2
Forward	$\sigma_E/E = 100\%/\sqrt{E} + 10\%$	3.1 – 4.9	3.1 – 4.9
Muon Spectrometer	$\sigma_{p_T}/p_T = 10\% \text{ at } p_T = 1 \text{ TeV}$	2.7	2.4

Table 2: The performance goals for each of the subsystems of the [ATLAS](#) detector. The $|\eta|$ coverage specifies the range where the subsystem needs to be able to provide measurements with the specified resolution. The resolutions include a p_T or E dependence that is added in quadrature with a p_T/E independent piece.

916 structing, and installing the detector took the combined effort of more than 3000
 917 scientists from 38 countries over almost two decades.

918 6.1 COORDINATE SYSTEM

919 The coordinate system defined for the [ATLAS](#) detector is used throughout all of
 920 the sections of this thesis. The choice of coordinate system reflects the cylind-
 921 rical symmetry of the [ATLAS](#) detector, and is oriented by the direction of the
 922 beamline which defines the z -direction. The positive z side of the detector is
 923 commonly referred to as the A -side, and the negative z side is referred to as
 924 the C -side. The $x - y$ plane is then the plane transverse to the beam direction,
 925 with the x direction defined as pointing from the interaction point to the center
 926 of the [LHC](#) ring and the y direction defined as pointing upwards. The nominal
 927 interaction point is the origin of this system.

928 It is more convenient in practice to use a cylindrical coordinate system. The
 929 angle from the z -axis is θ . The azimuthal angle uses the usual definition, with ϕ
 930 running around the z -axis and $\phi = 0$ corresponding to the x -axis. Many aspects
 931 of the detector are independent of the this coordinate to first order. The re-
 932 maining direction is typically specified using rapidity or pseudorapidity, where
 933 rapidity is defined as

$$y = \frac{1}{2} \ln \frac{E + p_z}{E - p_z} \quad (3)$$

934 Rapidity is particularly useful to indicate the component along the z direction
 935 because differences in rapidity are invariant to boosts along the z -direction. A
 936 similar quantity which depends only the θ is pseudorapidity,

$$\eta = -\ln \tan \frac{\theta}{2} \quad (4)$$

937 which is the same as rapidity when the particle is massless and in the limit where
 938 the energy is much larger than the particle's mass. It is often useful to refer to
 939 differences in solid angle using the pseudorapidity and the azimuthal angle:

$$\Delta R = \sqrt{\Delta\phi^2 + \Delta\eta^2} \quad (5)$$

940 The pseudorapidity is also invariant to boosts along the z -axis for high mo-
 941 mentum particles, and is preferable to rapidity because it does not depend on
 942 the specific choice of particle. Pseudorapidity is also preferable to θ because
 943 of the aforementioned boost-invariance and also because particle production is
 944 roughly uniform in equal-width intervals of η up to about $\eta = 5.0$. A particle
 945 travelling along the beampipe has $\eta = \text{inf}$ and a particle travelling perpendicular
 946 to the beampipe has $\eta = 0$. The extent of the tracker, $|\eta| < 2.5$, corresponds
 947 to approximately $0.05\pi < \theta[\text{rad}] < 0.95\pi$ and the extent of the calorimeters,
 948 $|\eta| < 4.9$ corresponds to approximately $0.005\pi < \theta[\text{rad}] < 0.995\pi$. Many de-
 949 tector components are broken into multiple subsystems to provide coverage at
 950 greater $|\eta|$. The lower $|\eta|$ region is referred to as the barrel, typically with $|\eta| \lesssim 2$,
 951 and the greater $|\eta|$ region is often referred to as the endcap.

952 The initial energy and momentum of a proton-proton collision along the z di-
 953 rection is unknown in hadron colliders because different energies and momen-
 954 tums can be carried by the partons. Along the transverse plane, however, the
 955 vector sum of momentum will be zero. For this reason, many physical quantities
 956 are quantified in terms of their projection onto the transverse plan, such as p_T
 957 or E_T . In addition, p_T alone determines the amount of curvature in the mag-
 958 netic field, and can be measured independently by measuring the curvature of a
 959 particle's propagation.

960 6.2 MAGNETIC FIELD

961 The magnet system used in [ATLAS](#) is designed to provide a substantial magnetic
 962 field in the two regions where the trajectory of particles is measured, the inner
 963 detector and the muon spectrometer. The magnetic field provides a curvature
 964 to the trajectory of charged particles and allows the precision tracking measure-
 965 ments to make high resolutions measurements of p_T . To provide a magnetic field
 966 in these regions, [ATLAS](#) uses a hybrid system with four separate, superconduct-
 967 ing magnets. A single solenoid provides a 2 T axial magnetic field for the inner
 968 detector, while a barrel toroid and two endcap toroids produce a magnetic field
 969 of 0.5 and 1 T, respectively, for the muon detectors. This geometry is illustrated
 970 in Figure 12, and the parameters of the three magnet systems are summarized in
 971 Table ??.

972 The central solenoid uses a single-layer coil with a current of 7.730 kA to gen-
 973 erate the 2 T axial field at the center of the magnet. The single-layer coil design
 974 enables a minimal amount of material to be used in the solenoid's construction,
 975 which is important because the solenoid is placed between the inner detector
 976 and the calorimeters. At normal incidence the magnet has only 0.66 radiation
 977 lengths worth of material, where one radiation length is the mean distance over

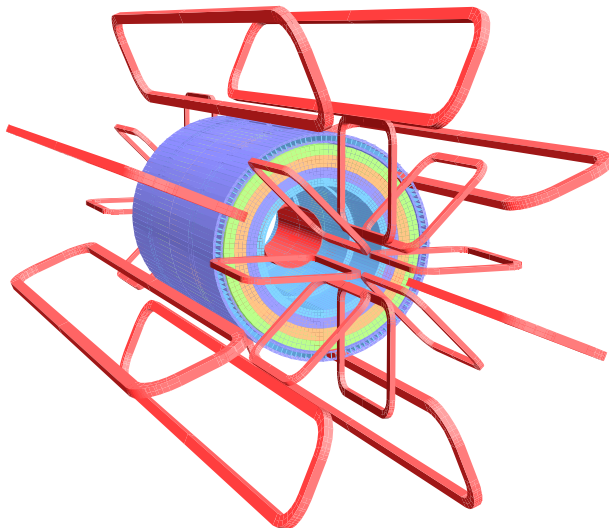


Figure 12: The layout of the four superconducting magnets in the [ATLAS](#) detector.

Parameter	Unit	Solenoid	Barrel Toroid	Endcap Toroids
Inner Diameter	m	2.4	9.4	1.7
Outer Diameter	m	2.6	20.1	10.7
Axial Length	m	5.3	25.3	5.0
Weight	tons	5.7	830	239
Conductor Size	mm ²	30×4.25	57×12	41×4.25
Peak Field	T	2.6	3.9	4.1
Heat Load	W	130	990	330
Current	kA	7.7	20.5	20.0
Stored Energy	MJ	38	1080	206

978 which a high-energy electron loses all but $1/e$ of its energy through material in-
 979 teractions [7]. The coil is made of a high-strength aluminum stabilized NbTi
 980 superconductor which was optimized to achieve a high field with minimal thick-
 981 ness. The axial magnetic field produced by the solenoid bends charged particles
 982 in the ϕ direction.

983 The barrel toroid consists of eight coils which generate a 0.5 T magnetic field
 984 in the cylindrical region around the calorimeters with an approximately 20 kA
 985 current. The coils are separated only by air to reduce the scattering of muons as
 986 they propagate through the region. The coils are made of an aluminum stabilized
 987 NbTiCu superconductor and each is separately housed in a vacuum and cold
 988 chamber. This magnetic configuration produces a field in the ϕ and so curves
 989 muons traversing the volume primarily in the η direction.

990 The endcap toroids follow a similar design to the barrel toroid, with eight
 991 separate NbTiCu coils, but in this case all eight are housed within a single cold
 992 mass. This extra structure is necessary to withstand the Lorentz forces exerted
 993 by the magnets. These magnets are rotated 22.5% relative to the barrel toroid to
 994 provide a uniform field in the transition between the two systems. The endcap
 995 toroids also produce a field in the ϕ direction and curve muons primarily in the
 996 η direction.

997 6.3 INNER DETECTOR

998 The [ATLAS](#) inner detector provides excellent momentum resolution as well as
 999 accurate primary and secondary vertex measurements through robust pattern
 1000 recognition that identifies tracks left by charged particles. These tracks fulfill a
 1001 number of important roles in the [ATLAS](#) measurement system: they measure the
 1002 momentum of charged particles including electrons and muons, they can iden-
 1003 tify electrons or photon conversions, they assign various particles and jets to
 1004 different vertices, and they provide a correction to E_T^{miss} measurements from
 1005 low energy particles. The system has to be accurate enough to separate tracks
 1006 from dozens of vertices and to resolve each vertex individually, as well as accu-
 1007 rate enough to measure the p_T of very high momentum tracks which curve very
 1008 little even in the large magnetic field. This is accomplished by several indepen-
 1009 dent layers of tracking systems. Closest to the interaction point is the very high
 1010 granularity Pixel detector, which is followed by the [SCT](#) layers. These subdetec-
 1011 tors both use discrete space-points to reconstruct track patterns. The final layer,
 1012 the transition radiation tracker ([TRT](#)), uses many layers of straw tube elements
 1013 interleaved with transition radiation material to provide continuous tracking.
 1014 The arrangement of these subdetectors is shown in Figure 13. To provide the
 1015 desired hermetic coverage, the subdetectors are divided into barrel and endcap
 1016 geometries. Figure 14 shows the layout of the subdetectors in more detail, and
 1017 illustrates how tracks at various pseudorapidities can traverse the subdetectors;
 1018 tracks with $\eta > 1.1$ begin to traverse the endcap subdetectors rather than those
 1019 in the barrel, and tracks with $\eta > 1.7$ use primarily endcap elements. The [IBL](#)
 1020 was not present during the original commissioning of the inner detector and is
 1021 not shown in this figure.

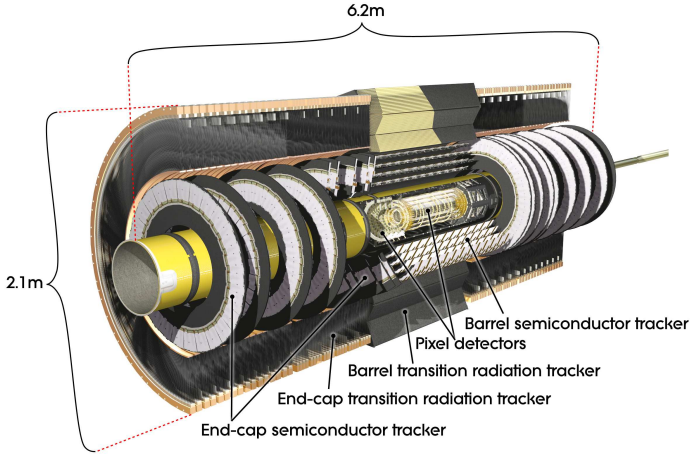


Figure 13: The arrangement of the subdetectors of the ATLAS inner detector. Each of the subdetectors is labelled in the cut-away view of the system.

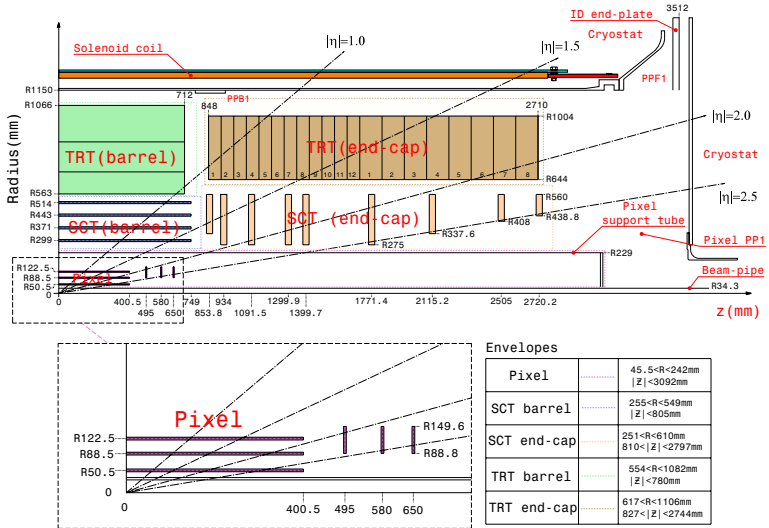


Figure 14: A quarter section of the ATLAS inner detector which shows the layout of each of the subdetectors in detail. The lower panel shows an enlarged view of the pixel detector. Example trajectories for a particle with $\eta = 1.0, 1.5, 2.0, 2.5$ are shown. The IBL, which was added after the original detector commissioning, is not shown.

1022 Figure 15 shows a computer generated three-dimensional view of the inner
 1023 detector along the beam axis, which emphasizes the straw tube structure of the
 1024 **TRT** as well as the overlapping geometry of the **SCT**. This figure also includes
 1025 the **IBL**, which was added during the long shutdown and provides an additional
 1026 measurement layer in the Pixel detector as of the beginning of Run 2. Figure 16
 1027 shows an alternative computer generated three-dimensional view transverse to
 1028 the beam axis which emphasizes the endcap structures of the **SCT** and **TRT**.

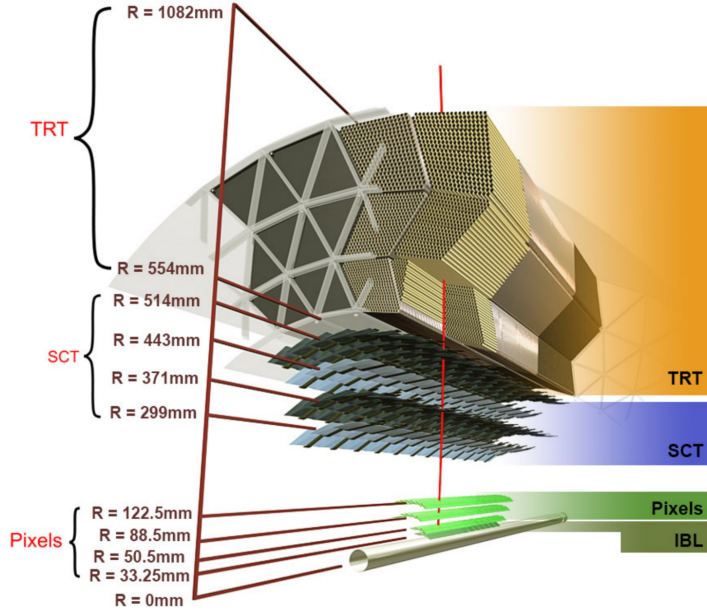


Figure 15: A computer generated three-dimensional view of the inner detector along the line of the beam axis. The subdetectors and their positions are labelled.

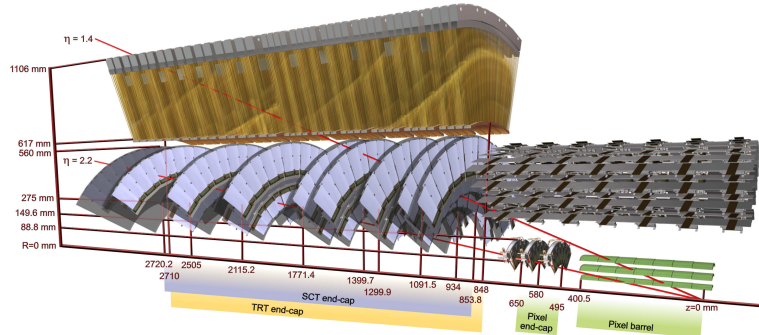


Figure 16: An alternative computer generated three-dimensional view of the inner detector transverse to the beam axis. The subdetectors and their positions are labelled.

1029 As the closest system to the interaction point, it is crucial for the inner de-
 1030 tector to use as little material as possible to avoid scattering of charged parti-
 1031 cles or photon conversions before they reach the remaining subdetectors. The
 1032 various components, including the readout electronics, cooling infrastructure,
 1033 gas volumes, and support structures, were designed to use as little material as

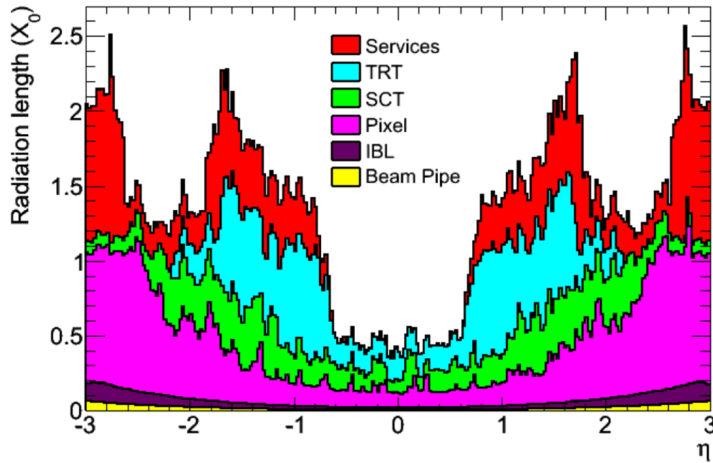


Figure 17: The integrated radiation lengths traversed by a straight track at the exit of the ID envelope, including the services and thermal enclosures. The distribution is shown as a function of $|\eta|$ and averaged over ϕ . The breakdown indicates the contributions of individual sub-detectors, including services in their active volume.

possible. Even with these optimizations, the combination of stringent performance requirements and the harsh radiation environment in the inner detector requires a significant amount of material. This material causes many electrons to lose most of their energy before reaching the electromagnetic calorimeter and approximately 40% of photons convert into an electron-positron pair while traversing the inner detector. Figure 17 shows the integrated radiation lengths traversed by a straight track in the inner detector as a function of η , grouped by subdetector. There is a large increase in the amount of material for support structures around $|\eta| = 1.7$, where the inner detector transitions from barrel to endcap.

The inner detector is designed to work as a cohesive unit to provide complete tracking information for charged particulars, and the subdetectors are complementary. Table ?? summarizes the parameters of each of the subdetectors as well as the parameters of the combined inner detector. Table ?? summarizes the expected performance that can be achieved by the inner detector as a whole.

6.3.1 PIXEL DETECTOR

The Pixel detector is the closest detector to the interaction point and therefore is designed to provide extremely high granularity while simultaneously handling a very large dose of radiation from collisions. It consists of four layers of silicon pixel modules, each of which provides a precision measurement on the trajectory of any charged particle. In the barrel region, the four layers are located at radial distances of 31 mm, 51 mm, 89 mm, and 123 mm. The three outer layers also include endcap elements, illustrated in Figure 14, which are located at 495 mm, 580 mm, and 650 mm away from the interaction point.

Parameter	Inner Detector	Pixel	SCT	TRT
Inner Radius	3.1 cm	3.1 cm	30 cm	56 cm
$ \eta $ Coverage	-	2.5	2.5	2.0
Cell Width	-	50 μm	80 μm	4 mm
Cell Length	-	400 μm	12 cm	70 cm
Material at $ \eta = 0.0$	0.3 X/X_0			
Material at $ \eta = 1.7$	1.2 X/X_0			
Material at $ \eta = 2.5$	0.5 X/X_0			
Number of Hits	48	4	8	36
Channels	99 M	92 M	6.3 M	350 k

Table 3: A summary of the parameters of the inner detector and each of the subdetectors [3].

1058 The pixel sensor technology uses a p-n junction of n-type bulk that contains
 1059 both p⁺ and n⁺ impurities. This combination is crucial in maintaining perfor-
 1060 mance after a significant radiation dose, as the n⁺ implants allow the sensor to
 1061 continue function after the n-type bulk has been converted to a p-type bulk by
 1062 the accumulation of radiation.

1063 The size of the pixels in the original three layers are 50 $\mu\text{m} \times$ 400 μm in the
 1064 $r - \phi$ and z directions, respectively. Those pixels are bump-bonded to front-end
 1065 readout chips, the FE-I3, which contains a total of 2880 pixels per chip. In the
 1066 three original pixel layers, the chips are grouped into modules composed of 16
 1067 chips each with 46,080 pixels per module and a total size of 20 mm x 60 mm
 1068 x 250 μm . The modules are further arranged into long rectangular structures
 1069 that run parallel to the beamline called staves. By tiling several staves with an
 1070 offset of 20°, the stave geometry provides full azimuthal coverage in the barrel
 1071 region while accomodating the readout and cable systems. The endcap regions
 1072 are instead arranged into petals and then into wheels. This arrangement can
 1073 be seen in Figure 18 which shows a computer-generated, cut-away image of the
 1074 outer three layers of the pixel detector. Together these three layers contain 1744
 1075 modules between the barrel and two endcap sections.

1076 The innermost layer, the IBL, was added during the long shutdown before Run
 1077 2, and provides the fourth track measurement. It was inserted directly into the
 1078 existing pixel detector by removing the existing beam pipe and replacing it with
 1079 a significantly smaller version. This insertion can be seen in action in Figure 19,
 1080 which emphasizes the extreme precision required to place the the 70 cm long
 1081 layer with only 2 mm of clearance. The IBL was commissioned to provide con-
 1082 tinued tracking robustness and high precision in the higher luminosity environ-
 1083 ment of Run 2 [9]. The proximity of this layer to the collisions necessitated an
 1084 even higher granularity and better radiation hardness than the other pixel lay-
 1085 ers. And the strict space requirements to add an active sensing layer so close to
 1086 the interaction point required a sensor chip with a much higher active area and
 1087 a larger overall area per chip. These requirements led to the development of a

Parameter	Particle	Value
Reconstruction Efficiency	Muon, $p_T = 1 \text{ GeV}$	96.8%
	Pion, $p_T = 1 \text{ GeV}$	84.0%
	Electron, $p_T = 5 \text{ GeV}$	90.0%
Momentum Resolution	$p_T = 1 \text{ GeV}, \eta \approx 0$	1.3%
	$p_T = 1 \text{ GeV}, \eta \approx 2.5$	2.0%
	$p_T = 100 \text{ GeV}, \eta \approx 0$	3.8%
	$p_T = 100 \text{ GeV}, \eta \approx 2.5$	11%
Transverse IP Resolution	$p_T = 1 \text{ GeV}, \eta \approx 0$	$75 \mu\text{m}\%$
	$p_T = 1 \text{ GeV}, \eta \approx 2.5$	$200 \mu\text{m}$
	$p_T = 1000 \text{ GeV}, \eta \approx 0$	$11 \mu\text{m}$
	$p_T = 1000 \text{ GeV}, \eta \approx 2.5$	$11 \mu\text{m}$
Longitudinal IP Resolution	$p_T = 1 \text{ GeV}, \eta \approx 0$	$150 \mu\text{m}\%$
	$p_T = 1 \text{ GeV}, \eta \approx 2.5$	$900 \mu\text{m}$
	$p_T = 1000 \text{ GeV}, \eta \approx 0$	$90 \mu\text{m}$
	$p_T = 1000 \text{ GeV}, \eta \approx 2.5$	$190 \mu\text{m}$

Table 4: A summary of the expected performance of the combined inner detector [8]. Included are the reconstruction efficiencies for multiple particle types as well as the momentum and IP resolution for various momenta.

1088 new chip type, the FE-I4 (compared to the FE-I3 chips used in the original pixel
 1089 detector) with improved radiation hardness and a larger active footprint of 90%.
 1090 The IBL is comprised of 448 of these individual chips arranged in 14 staves, with
 1091 26,880 pixels per chip and a chip size of 18.5 mm x 41.3 mm x 200 μm . The
 1092 staves, like in the other layers of the pixel detector, are offset by 14° to provide
 1093 full azimuthal coverage. This arrangement can be seen in Figure 20, which shows
 1094 two computer-generated images of the IBL geometry and includes the some of
 1095 the remaining pixel layers.

1096 6.3.2 SEMICONDUCTOR TRACKER

1097 The SCT, the subdetector which immediately surrounds the Pixel detector, pro-
 1098 vides additional discrete measurements of the trajectory of a charged particle.
 1099 Because the SCT is further away from the interaction point, the spatial resolution
 1100 does not need to be as high as in the pixel detector, and so the SCT uses micro-
 1101 strips instead of pixels. Although pixels provide a more accurate measurement,
 1102 the number of pixels and readout channels required to cover the cylindrical area
 1103 at the radius of the SCT layers would be prohibitively complicated and expensive.

1104 Each individual silicon strip sensor contains 768 individual readout strips
 1105 with a total area of 6.36 cm x 6.40 cm and a pitch of 80 μm . Pairs of these sen-
 1106 sors are then bonded together to form a combined strip with a length of 12.8 cm.
 1107 Two of these combined strips are then placed back to back with a relative tilt

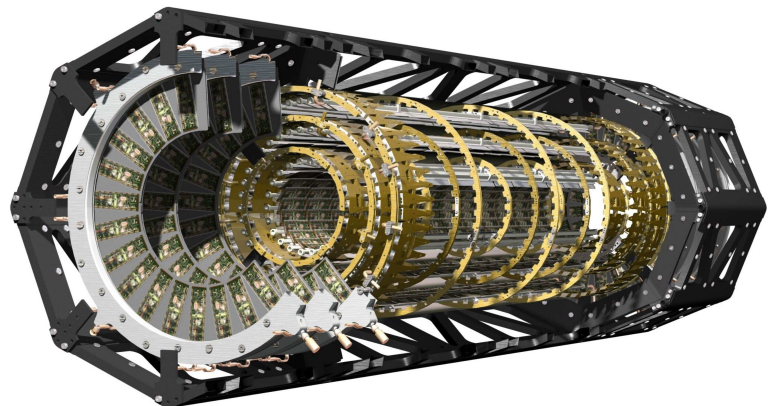


Figure 18

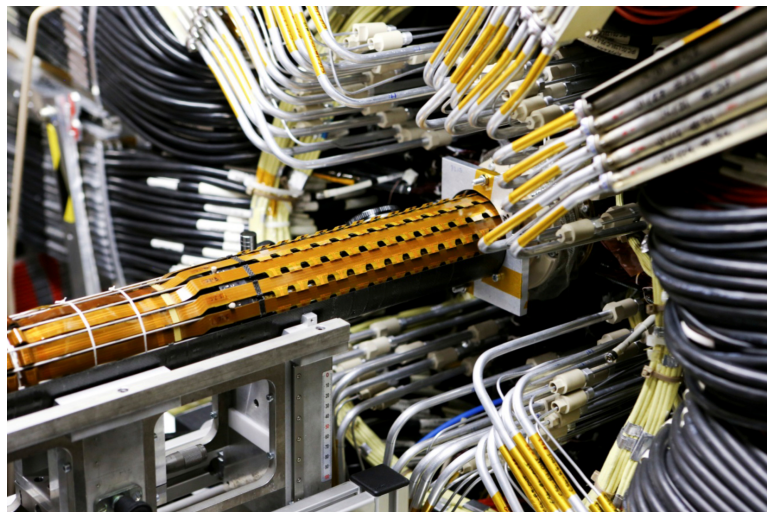


Figure 19: An image of the insertion of the [IBL](#) into the current pixel detector.

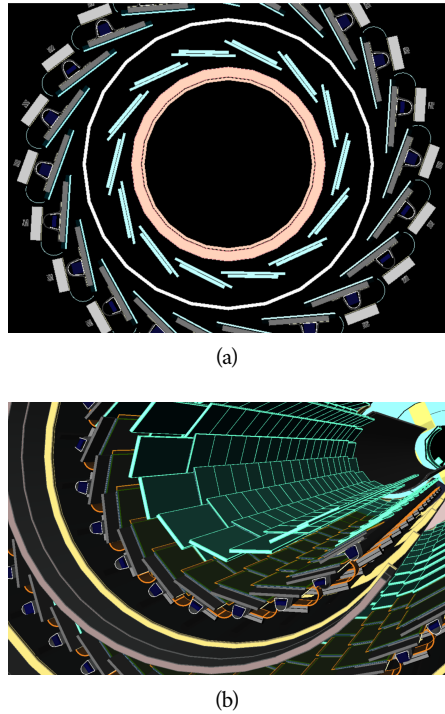


Figure 20: A three-dimensional computer-generated image of the geometry of the [IBL](#) with a view (a) mostly transverse to the beam pipe (b) mostly parallel to the beam pipe.

of 40 mrad. This geometry is illustrated in an exploded-out view in Figure 21. The purpose of angular offset of the consecutive layers is to allow the strip sensor areas to more accurately measure the position of a particle by comparing the overlap of the two strips which were traversed by a track.

Four of these double layers are placed in the barrel region, with radii of 284 mm, 355 mm, 427 mm, and 498 mm. Together these layers provide eight additional measurements for each track that traverses the central $|\eta|$ region. In the endcap region, the layers are arranged in wheels, with the double layers similarly offset to provide improved resolution. With these configurations, the [SCT](#) achieves a spatial resolution of $17 \mu\text{m}$ in the $r - \phi$ direction and $580 \mu\text{m}$ in the z direction.

6.3.3 TRANSITION RADIATION TRACKER

The final component of the inner detector, the [TRT](#), provides continuous tracking using straw drift tubes. The tubes are made of Kapton and aluminum with a diameter of 4 mm and are filled with a gas mixture of 70% Xe, 27% CO₂, and 3% O₂. At the center of each tube is a gold-plated anode tungsten wire $30 \mu\text{m}$ in diameter. When a charged particle passes through these tubes, it ionizes the gas within. The ions produced drift in the electric field established between the wire and the tube wall, and the large electric field near the wire produces avalanche multiplication and results in an electric current on the wire that is read out by the electronics and provides a track measurement. The time it takes the ioniza-

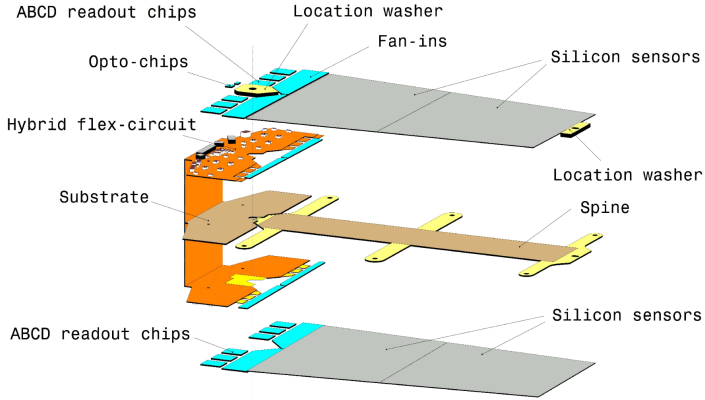


Figure 21: An exploded view of the geometry of the [SCT](#) double layers in the barrel region.

tion to drift to the wire can be used to estimate the distance from the wire that the particle passed through the tube; this gives a resolution on the distance of approximately $130\mu\text{m}$. Combining several such measurements between consecutive hits in the [TRT](#) tubes allows the trajectory of the particle to be reconstructed.

In addition to the continuous tracking, the detector can use transition radiation produced when a particle passes between the layers to distinguish between electrons and heavier charged particles. The space between the tubes is filled with CO_2 , and so has a different dielectric constant than the gas within the tubes which contains Xe. At the transition between those media, a relativistic particle emits radiation proportional to γ , so inversely proportional to mass at a fixed momentum. The photons produced in this transition then produces an ionization cascade which is significantly larger than the signal for the minimally-ionizing charged particles. To distinguish between these two cases, the [TRT](#) defines two signal thresholds, a low threshold for the typical signal produced by a minimally ionizing particle ([MIP](#)) and a high threshold for the the signal produced by transition radiation. A high momentum electron is expected to produce approximately 7 to 10 high threshold hits as it traverses the [TRT](#), and thus these hits provide a way to distinguish electrons from other charged particles.

The [TRT](#) contains 351,000 tubes in total, divided between the barrel and endcap regions. In the barrel region, the tubes are 144 cm long and arranged in 73 layers parallel to the beampipe. In the endcap region, the tubes are 37 cm long and arranged in 160 layers transverse to the beampipe. These configurations can be seen in Figure 15 and Figure 16. With this geometry the [TRT](#) achieves a resolution of $130\mu\text{m}$ in the $r - \phi$ direction.

6.4 CALORIMETRY

The combination of calorimeter systems used in [ATLAS](#) can measure the energy of electrons, photons, hadrons, and hadronic jets with complete coverage up to $|\eta| < 4.9$ and across ϕ . Unlike the inner detector, the calorimeters are capable of measuring neutral particles. To accomplish precision measurements of these

1158 particle types, the [ATLAS](#) calorimeter system uses four individual calorimeters,
 1159 a [LAr](#) electromagnetic calorimeter in the barrel region, a tile hadronic calorime-
 1160 ter in the barrel region, a [LAr](#) hadronic endcap calorimeter, and a [LAr](#) forward
 1161 calorimeter. Together these provide hermetic coverage for the [ATLAS](#) detector.
 1162 The configuration of these calorimeters is illustrated in Figure 22. **Note: I could**
 1163 **make this section much longer. It might be nice to include a more com-**
 1164 **plete description of showers for example. I will extend this section if their**
 1165 **is space at the end.**

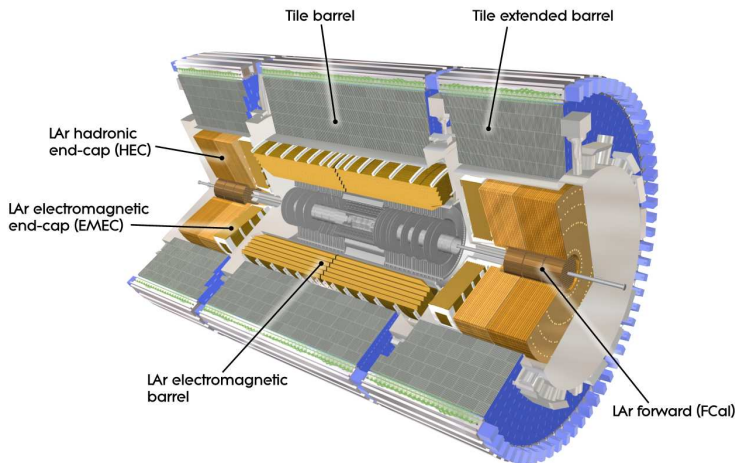


Figure 22

1166 The calorimeters are designed to absorb and measure the energy carried by
 1167 a particle, and completely stop the particle's propagation in the process. This
 1168 requires a significant amount of material to provide interactions. These interac-
 1169 tions then produce secondary particles, which can produce secondary particles
 1170 in turn, and thus form a cascade of particles called an electromagnetic ([EM](#)) or
 1171 hadronic shower, depending on the governing mechanism. Electromagnetic and
 1172 hadronic showers have very different properties and require different technolo-
 1173 gies to measure them accurately. All of the calorimeters in the [ATLAS](#) calorimeter
 1174 system are sampling calorimeters, that is they use alternating layers of absorbing
 1175 and active material. The dense absorbing layers initiate the showers while the ac-
 1176 tive layers measure the energy of the produced particles. A fraction of the energy
 1177 is lost in the inactive layers, so the energy measurement from the active layers
 1178 has to be corrected to estimate the actual energy of the particle.

1179 The [EM](#) calorimeter provides around 20 radiation lengths (X_0) while the hadronic
 1180 calorimeter provides around 10 interaction lengths (λ_0). As mentioned previ-
 1181 ously, radiation lengths measure the distance over which an electromagnetically
 1182 interacting particle loses a characteristic fraction of its energy. Interaction lengths,
 1183 on the other hand, measure the mean distance travelled by a hadronic particle be-
 1184 fore undergoing a nuclear interaction [7]. Figure 23 show the radiation lengths
 1185 in the layers of the [EM](#) calorimeter in the barrel region as well as the interaction
 1186 lengths for all calorimeters.

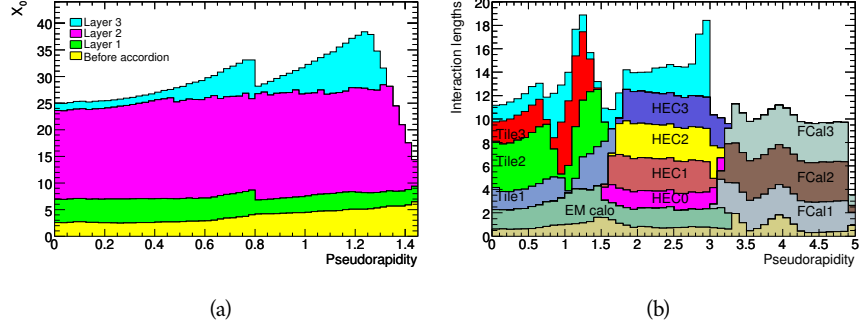


Figure 23: The depth of (a) the electromagnetic barrel calorimeter in radiation lengths and (b) all calorimeters in interaction lengths as a function of pseudorapidity.

1187 6.4.1 ELECTROMAGNETIC CALORIMETER

1188 The electromagnetic calorimeters use alternating layers of Liquid Argon and
 1189 lead in an accordion shape. The accordion shape allows a construction that pro-
 1190 vides complete coverage in the ϕ direction while also providing many alterna-
 1191 ting layers for the a particle to pass through. The configuration is detailed in
 1192 Figure 24. When an electron or photon passes through the lead, it produces an
 1193 electromagnetic shower. The particles produced in those showers then pass into
 1194 and ionize the Liquid Argon; the ions produced can then be collected by an elec-
 1195 trode in the Liquid Argon layer to provide the actual energy measurement.

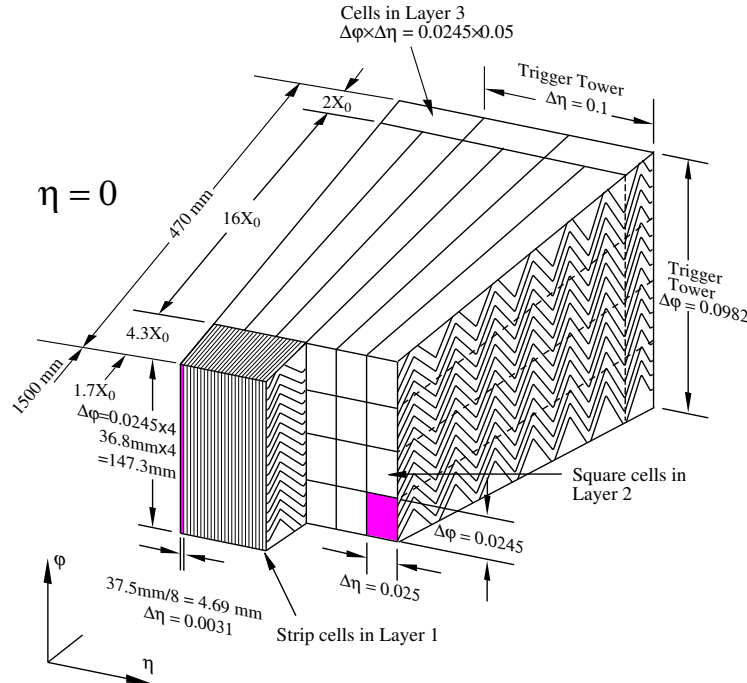


Figure 24: A schematic of the LAr calorimeter in the barrel region, highlighting the ac-
 cordion structure.

The barrel region is covered by a presampler and three separate sampling layers with decreasing segmentation. The presampler is just a thin layer of Liquid Argon which measures the energy of any electromagnetic showers which are initiated before the particle reaches the calorimeter due to interactions with the detector material. The first layer is the strip layer, which has fine segmentation in η to enhance the identification of shower shapes and to provide a precise η measurement for reconstructing photons and electrons. The strip layer has only 4 radiation lengths worth of material, and has a segmentation of $\Delta\eta = 0.003$ and $\Delta\phi = 0.1$. The second layer is also finely segmented, with a segmentation of $\Delta\eta = 0.025$ and $\Delta\phi = 0.025$, and a thickness of $16 X_0$. This layer is designed to contain an electromagnetic shower and to measure the majority of the energy for photons and electrons. The third layer is only $2 X_0$ thick and measures the energy of electromagnetic showers which leak out of the second layer, and helps to separate electromagnetic showers from hadronic showers. The structure of the LAr endcap calorimeter is similar except that the layers are arranged parallel to the beampipe to measure energy deposits from high η particles.

6.4.2 HADRONIC CALORIMETERS

The hadronic calorimeters use a few different technologies to satisfy the resolution demands in the different areas of the detector, and together they cover the region $|\eta| < 2.7$. In the barrel region, for $|\eta| < 1.7$, the hadronic calorimeters are constructed of alternating tiles of steel and plastic scintillator. Like in the electromagnetic calorimeter, the dense layer initiates a shower (in this case the dense layer is the steel and the shower is hadronic) of particles which pass into and ionize the following layer. The ionization in the plastic scintillator instead produces a light signal proportional to the amount of ionization produced by the shower, and this signal is measured using photomultipliers and provides the actual energy measurement. The construction of a tile in the calorimeter is shown Figure ??, which highlights the alternating layers of steel and scintillator.

This tile calorimeter, as well as the remaining hadronic calorimeters, have a much coarser granularity than the electromagnetic calorimeters. The high granularity is not needed for an accurate energy measurement, and the hadronic calorimeters are not designed to distinguish particle types like the electromagnetic calorimeters. The tile granularity is approximately $\Delta\eta = 0.1$ and $\Delta\phi = 0.1$, and the segmentation in depth and η is shown in Figure 26.

The remaining hadronic calorimeters all use the same alternating, sampling structure but with different active and inactive materials. The hadronic endcap calorimeter covers the range of $1.5 < |\eta| < 3.2$ and uses an inactive layer of copper and an active layer of **liquid argon!**. The forward calorimeter covers the range of $3.1 < |\eta| < 4.9$ and uses a dense matrix of copper and tungsten filled with Liquid Argon.

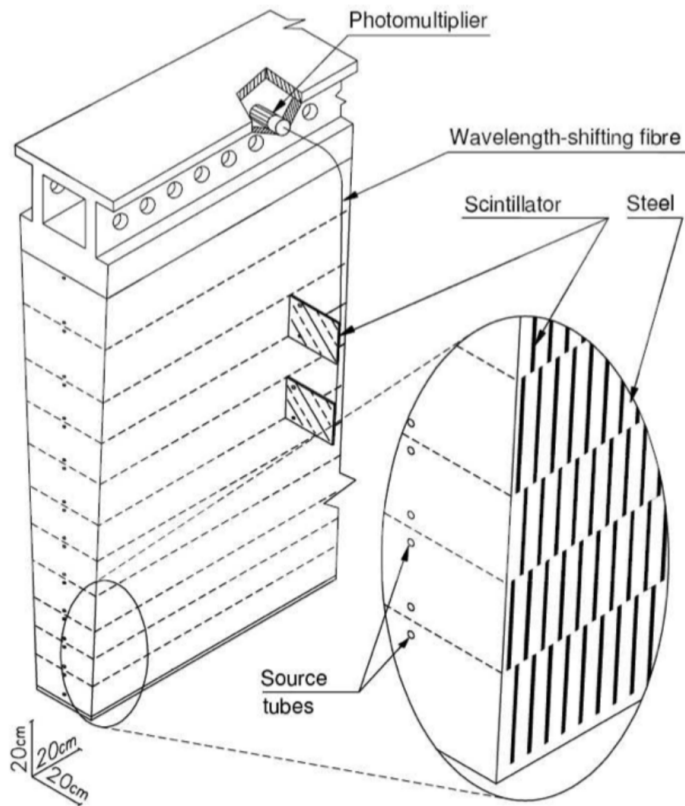


Figure 25: A schematic of a hadronic tile module which shows the alternating layers of steel and plastic scintillator.

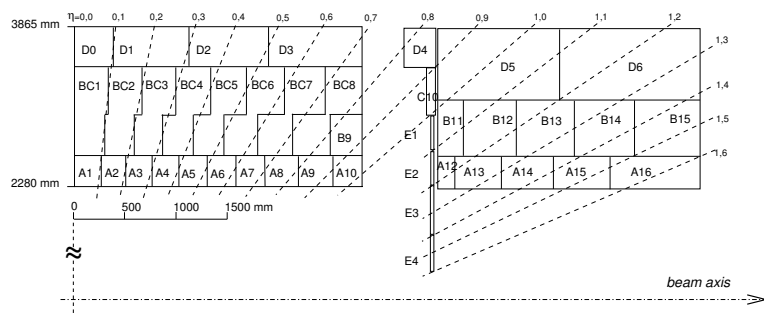


Figure 26: The segmentation in depth and η of the tile-calorimeter modules in the central (left) and extended (right) barrels.

1236 6.5 MUON SPECTROMETER

1237 Among SM particles, only muons and neutrinos consistently pass through the
 1238 calorimeters. Because the neutrinos are also electrically neutral, there is no fea-
 1239 sible option to measure them directly in ATLAS. The muons, on the other hand,
 1240 are charged and are thus already measured as a track in the inner detector. The
 1241 muon spectrometer provides a way to consistently identify those muon tracks
 1242 and to also provide an additional measurement of their momentum.

1243 The muon spectrometer contains four subdetectors that cover the barrel and
 1244 endcap regions up to $|\eta| < 2.7$. In the barrel region, the muon spectrometer uses
 1245 a combination of RCP!s (RCP!)s and MDTs to provide both a coarse, fast measure-
 1246 ment for triggering and a precise momentum measurement for offline event re-
 1247 construction. Similarly, in the endcap region, the Thin Gap Chambers (TGCs),
 1248 MDTs, and Cathode Strip Chambers (CSCs) allow for triggering and precise mea-
 1249 surements. The overall layout of the muon systems are shown in the cut-away
 1250 diagram in Figure 27, and Figure 28 shows a precise schematic of the layout of
 1251 each of the detecting elements.

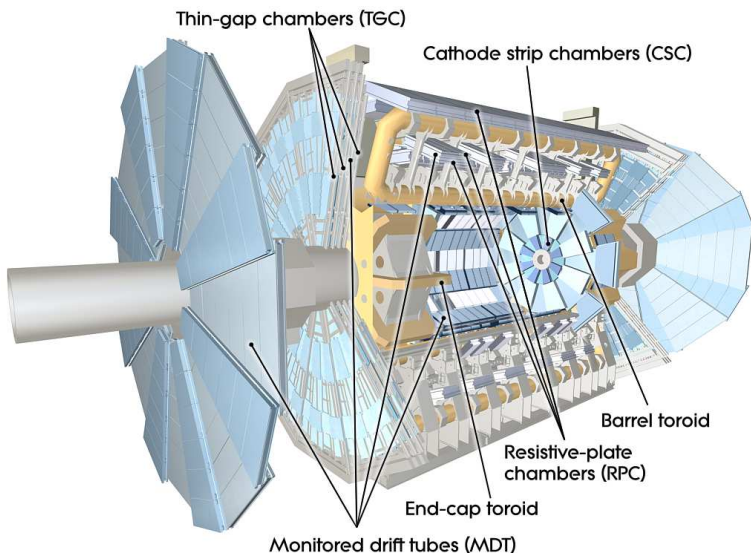


Figure 27: A cut-away diagram of the muon systems on ATLAS.

1252 6.5.1 RESISTIVE PLATE CHAMBER AND THIN GAP CHAMBER

1253 The Resistive Plate Chamber (RPC) and TGC detectors are designed to provide
 1254 coarse measurements of the positions of muons within 15-25 ns, so that they
 1255 can be used for triggering.

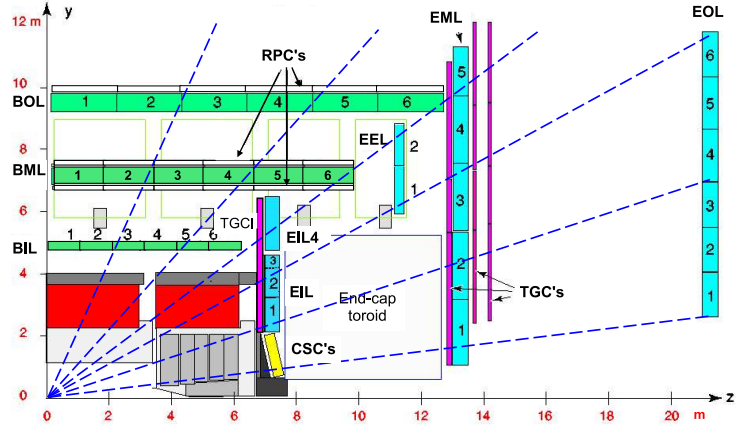


Figure 28: A quarter view of the muon spectrometer which highlights the layout of each of the detecting elements. The BOL, BML, BIL, EML, and EOL are all MDT elements, where the acronyms encode their positions.

1256 6.6 TRIGGER

1257 6.6.1 TRIGGER SCHEME

1258 6.6.2 MISSING TRANSVERSE ENERGY TRIGGERS

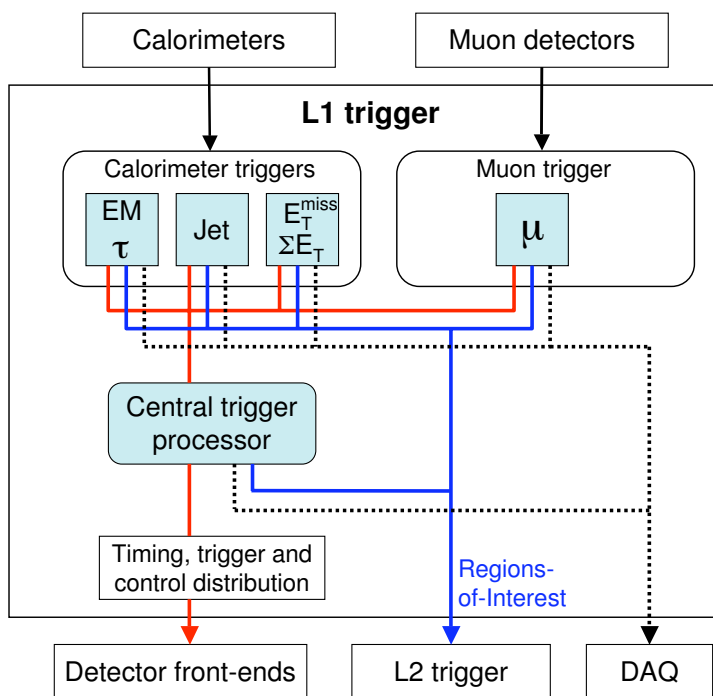


Figure 29

7

1259

1260 EVENT RECONSTRUCTION

1261 The ATLAS experiment combines measurements in the subdetectors to form a
1262 cohesive picture of each physics event.

1263 7.1 TRACKS AND VERTICES

1264 7.1.1 TRACK RECONSTRUCTION

1265 7.1.1.1 NEURAL NETWORK

1266 7.1.1.2 PIXEL DE/DX

1267 7.1.2 VERTEX RECONSTRUCTION

1268 7.2 JETS

1269 7.2.1 TOPOLOGICAL CLUSTERING

1270 7.2.2 JET ENERGY SCALE

1271 7.2.3 JET ENERGY SCALE UNCERTAINTIES

1272 7.2.4 JET ENERGY RESOLUTION

1273 7.3 ELECTRONS

1274 7.3.1 ELECTRON IDENTIFICATION

1275 7.4 MUONS

1276 7.4.1 MUON IDENTIFICATION

1277 7.5 MISSING TRANSVERSE ENERGY

1278

PART IV

1279

CALORIMETER RESPONSE

1280

You can put some informational part preamble text here.

8

1281

1282 RESPONSE MEASUREMENT WITH SINGLE HADRONS

1283 As discussed in Section 7.2, colored particles produced in collisions hadronize
1284 into jets of multiple hadrons. One approach to understanding jet energy mea-
1285 surements in the ATLAS calorimeters is to evaluate the calorimeter response to
1286 those individual hadrons; measurements of individual hadrons can be used to
1287 build up an understanding of the jets that they form. The redundancy of the
1288 momentum provided by the tracking system and the energy provided by the
1289 calorimeter provides an opportunity to study calorimeter response using real
1290 collisions, as described further in Section 8.2.

1291 Calorimeter response includes a number of physical effects that can be ex-
1292 tracted to provide insight into many aspects of jet modeling. First, many charged
1293 hadrons interact with the material of the detector prior to reaching the calorime-
1294 ters and thus do not deposit any energy. Comparing this effect in data and simu-
1295 lation is a powerful tool in validating the interactions of particles with the mate-
1296 rial of the detector and the model of the detector geometry in simulation, see Sec-
1297 tion 8.2.2. The particles which do reach the calorimeter deposit their energy into
1298 several adjacent cells, which are then clustered together. The energy of the clus-
1299 ter is then the total energy deposited by that particle. Comparing the response of
1300 hadrons in data to that of simulated hadrons provides a direct evaluation of the
1301 showering of hadronic particles and the energy deposited by particles in matter
(Section 8.2.4).

1303 The above studies all use an inclusive selection of charged particles, which are
1304 comprised predominantly of pions, kaons, and (anti)protons. It is also possible to
1305 measure the response to various identified particle types separately to evaluate
1306 the simulated interactions of each particle, particularly at low energies where
1307 differences between species are very relevant. Pions and (anti)protons can be
1308 identified through decays of long-lived particles, in particular Λ , $\bar{\Lambda}$, and K_S^0 , and
1309 then used to measure response as described above. This is discussed in detail in
1310 Section 8.3.

1311 The results in this chapter use data collected at 7 and 8 TeV collected in 2010
1312 and 2012, respectively. Both are included as the calorimeter was repaired and
1313 recalibrated between those two data-taking periods. Both sets of data are com-
1314 pared to an updated simulation that includes new physics models provided by
1315 Geant4 [10] and improvements in the detector description [11, 12]. The present
1316 results are published in European Physical Journal C (EPJC) [13] and can be com-
1317 pared to a similar measurement performed in 2009 and 2010 [14], which used
1318 the previous version of the simulation framework [15].

1319 8.1 DATASET AND SIMULATION

1320 8.1.1 DATA SAMPLES

1321 The two datasets used in this chapter are taken from dedicated low-pileup runs
 1322 where the fraction of events with multiple interactions was negligible. These
 1323 datasets are used rather than those containing full-pileup events to facilitate mea-
 1324 surement of isolated hadrons. The 2012 dataset at $\sqrt{s} = 8$ TeV contains 8 mil-
 1325 lion events and corresponds to an integrated luminosity of 0.1 nb^{-1} . The 2010
 1326 dataset at $\sqrt{s} = 7$ TeV contains 3 million events and corresponds to an inte-
 1327 grated luminosity of 3.2 nb^{-1} . The latter dataset was also used for the 2010 re-
 1328 sults [14], but it has since been reanalyzed with an updated reconstruction in-
 1329 cluding the final, best understanding of the detector description for the material
 1330 and alignment from Run 1.

1331 8.1.2 SIMULATED SAMPLES

1332 The two datasets above are compared to simulated single-, double-, and non-
 1333 diffractive events generated with Pythia8 [16] using the A2 configuration of
 1334 hadronization [17] and the MSTW 2008 parton-distribution function set [18,
 1335 19]. The admixture of the single-, double-, and non-diffractive events uses the
 1336 default relative contributions from Pythia8. The conditions and energies for
 1337 the two simulations are chosen so that they match those of the corresponding
 1338 dataset.

1339 To evaluate the interaction of hadrons with detector material, the simulation
 1340 uses two different collections of hadronic physics models, called physics lists, in
 1341 Geant4 9.4 [20]. The first, QGSP_BERT, combines the Bertini intra-nuclear
 1342 cascade [21–23] below 9.9 GeV, a parametrized proton inelastic model from 9.5
 1343 to 25 GeV [24], and a quark-gluon string model above 12 GeV [25–29]. The
 1344 second, FTFP_BERT, combines the Bertini intra-nuclear cascade [21–23] below
 1345 5 GeV and the Fritiof model [30–33] above 4 GeV. In either list, Geant4 en-
 1346 forces a smooth transition between models where multiple models overlap.

1347 8.1.3 EVENT SELECTION

1348 The event selection for this study is minimal, as the only requirement is selecting
 1349 good-quality events with an isolated track. Such events are triggered by requir-
 1350 ing at least two hits in the minimum-bias trigger scintillators. After trigger, each
 1351 event is required to have exactly one reconstructed vertex, and that vertex is re-
 1352 quired to have four or more associated tracks.

1353 The particles which are selected for the response measurements are first iden-
 1354 tified as tracks in the inner detector. The tracks are required to have at least 500
 1355 MeV of transverse momentum. To ensure a reliable momentum measurement,
 1356 these tracks are required to have at least one hit in the pixel detector, six hits in
 1357 the SCT, and small longitudinal and transverse impact parameters with respect
 1358 to the primary vertex [14]. For the majority of the measurements in this chapter,

1359 the track is additionally required to have 20 hits in the TRT, which significantly
 1360 reduces the contribution from tracks which undergo nuclear interactions. This
 1361 requirement and its effect is discussed in more detail in Section 8.2.5. In addition,
 1362 tracks are rejected if there is any other reconstructed track which extrapolates
 1363 to the calorimeter within a cone of $\Delta R = \sqrt{(\Delta\phi)^2 + (\Delta\eta)^2} < 0.4$. This require-
 1364 ment guarantees that the contamination of energy from nearby charged particles
 1365 is negligible [14].

1366 8.2 INCLUSIVE HADRON RESPONSE

1367 The calorimeter response is more precisely defined as the ratio of the measured
 1368 calorimeter energy to the true energy carried by the particle, although this true
 1369 energy is unknown. For charged particles, however, the inner detector provides
 1370 a very precise measurement of momentum (with uncertainty less than 1%) that
 1371 can be used as a proxy for true energy. The ratio of the energy deposited by
 1372 the charged particle in the calorimeter, E , to its momentum measured in the
 1373 inner detector p , forms the calorimeter response measure called E/p . Though
 1374 the distribution of E/p contains a number of physical features, this study focuses
 1375 on the trends in two aggregated quantities: $\langle E/p \rangle$, the average of E/p for the
 1376 selected tracks, and the zero fraction, the fraction of tracks with no associated
 1377 energy in the calorimeter for those tracks.

1378 The calorimeter energy assigned to a track is defined using clusters. The clus-
 1379 ters are formed using a 4–2–0 algorithm [34] that begins with seeds requiring
 1380 at least 4 times the average calorimeter cell noise. The neighboring cells with
 1381 at least twice that noise threshold are then added to the cluster, and all bound-
 1382 ing cells are then added with no requirement. This algorithm minimizes noise
 1383 contributions through its seeding process, and including the bounding cells im-
 1384 proves the energy resolution [35]. The clusters are associated to a given track
 1385 if they fall within a cone of $\Delta R = 0.2$ of the extrapolated position of the track,
 1386 which includes about 90% of the energy on average [14]. This construction is
 1387 illustrated in Figure 30.

1388 8.2.1 E/P DISTRIBUTION

1389 The E/p distributions measured in both data and simulation are shown in Fig-
 1390 ure 31 for two example bins of track momentum and for tracks in the central
 1391 region of the detector. These distributions show several important features of
 1392 the E/p observable. The large content in the bin at $E = 0$ comes from tracks that
 1393 have no associated cluster, which occurs due to interactions with detector mate-
 1394 rial prior to reaching the calorimeter or the energy deposit being insufficiently
 1395 large to generate a seed, and are discussed in Section 8.2.2. The small negative
 1396 tail also comes from tracks that do not deposit any energy in the calorimeter but
 1397 are randomly associated to a cluster with an energy below the noise threshold.
 1398 The long positive tail above 1.0 comes from the contribution of neutral parti-
 1399 cles. Nearby neutral particles deposit (sometimes large) additional energy in the
 1400 calorimeter but do not produce tracks in the inner detector, so they cannot be

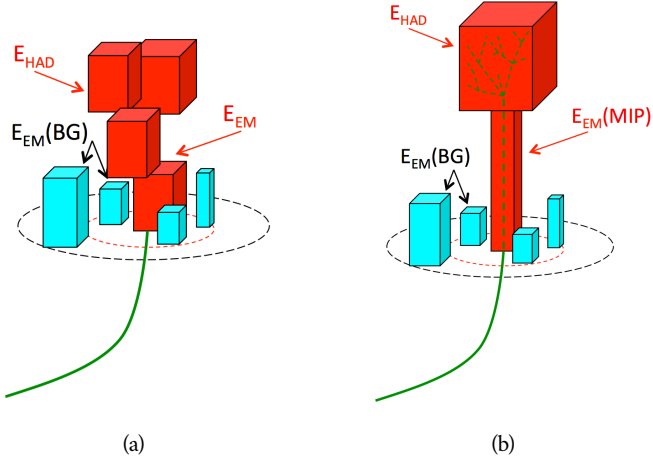


Figure 30: An illustration (a) of the E/p variable used throughout this paper. The red energy deposits come from the charged particle targeted for measurement, while the blue energy deposits are from nearby neutral particles and must be subtracted. The same diagram (b) for the neutral-background selection, described in Section 8.2.3.

1401 rejected by the track isolation requirement. Additionally the peak and mean of
1402 the distribution falls below 1.0 because of the loss of energy not found within
1403 the cone as well as the non-compensation of the calorimeter.

1404 The data and simulation share the same features, but the high and low tails
1405 are significantly different. The simulated events tend to overestimate the con-
1406 tribution of neutral particles to the long tail, an effect which can be isolated and
1407 removed as discussed in Section 8.2.3. Additionally, the simulated clusters have
1408 less noise on average, although this is a small effect on the overall response.

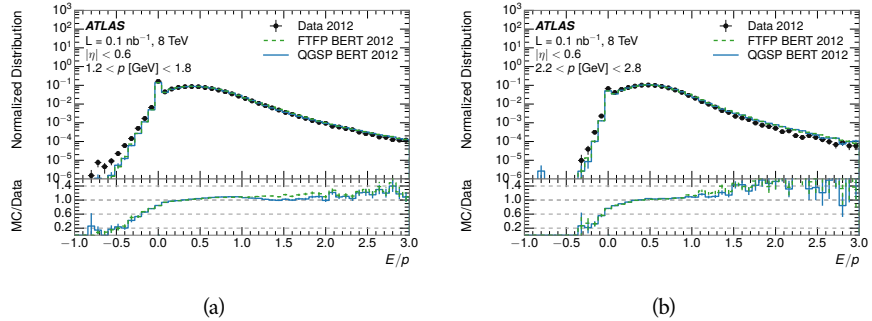


Figure 31: The E/p distribution and ratio of simulation to data for isolated tracks with (a) $|\eta| < 0.6$ and $1.2 < p/\text{GeV} < 1.8$ and (b) $|\eta| < 0.6$ and $2.2 < p/\text{GeV} < 2.8$.

1409 8.2.2 ZERO FRACTION

1410 The fraction of particles with no associated clusters, or similarly those with $E \leq$
1411 0, reflects the modeling of both the detector geometry and hadronic interactions.

1412 The zero fraction is expected to rise as the amount of material a particle traverses
 1413 increases, while it is expected to decrease as the particle energy increases. This
 1414 dependence can be seen in Figure 32, where the zero fraction in data and simulation
 1415 is shown as a function of momentum and the amount of material measured
 1416 in interaction lengths. The trends are similar between 2010 and 2012 and for
 1417 positively and negatively charged particles. The zero fraction decreases with
 1418 energy as expected. The absolute discrepancy in zero fraction decreases with
 1419 momentum from 5% to less than 1%, but this becomes more pronounced in the
 1420 ratio as the zero fraction shrinks quickly with increasing momentum. There is
 1421 a small constant difference between the data and simulation in both interaction
 1422 models that becomes more pronounced. The amount of material in the detector
 1423 increases with η , which is used to obtain results for interaction lengths ranging
 1424 between 0.1 and 0.65 λ . As the data and simulation have significant disagree-
 1425 ment in the zero fraction over a number of interaction lengths, the difference
 1426 must be primarily from the modeling of hadronic interactions with detector ma-
 1427 terial and not just the detector geometry. Although two different hadronic in-
 1428 teraction models are shown in the figure, they have very similar discrepancies to
 1429 data because both use the same description (the BERT model) at low momentum.

1430 8.2.3 NEUTRAL BACKGROUND SUBTRACTION

1431 The isolation requirement on hadrons is only effective in removing an energy
 1432 contribution from nearby charged particles. Nearby neutral particles, predomi-
 1433 nantly photons from π^0 decays, also add their energy to the calorimeter clusters,
 1434 but mostly in the electromagnetic calorimeter. It is possible to measure this con-
 1435 tribution, on average, using late-showering hadrons that minimally ionize in the
 1436 electromagnetic calorimeter. Such particles are selected by requiring that they
 1437 deposit less than 1.1 GeV in the EM calorimeter within a cone of $\Delta R < 0.1$
 1438 around the track. To ensure that these particles are well measured, they are addi-
 1439 tionally required to deposit between 40% and 90% of their energy in the hadronic
 1440 calorimeter within the same cone.

1441 These particles provide a clean sample to measure the nearby neutral back-
 1442 ground because they do not deposit energy in the area immediately surrounding
 1443 them in the EM calorimeter, as shown in Figure 30. So, the energy deposits in the
 1444 region $0.1 < \Delta R < 0.2$ can be attributed to neutral particles alone. To estimate
 1445 the contribution to the whole cone considered for the response measurement,
 1446 that energy is scaled by a geometric factor of $4/3$. This quantity, $\langle E/p \rangle_{BG}$, mea-
 1447 sured in aggregate over a number of particles, gives the contribution to $\langle E/p \rangle$
 1448 from neutral particles in the EM calorimeter. Similar techniques were used in
 1449 the individual layers of the hadronic calorimeters to show that the background
 1450 from neutrals is negligible in those layers [14].

1451 The distribution of this background estimate is shown in Figure 33 for data
 1452 and simulation with the two different physics lists. The contribution from neu-
 1453 tral particles falls from 0.1 at low momentum to around 0.03 for particles above
 1454 7 GeV. Although the simulation captures the overall trend, it significantly over-
 1455 estimates the neutral contribution for tracks with momentum between 2 and 8

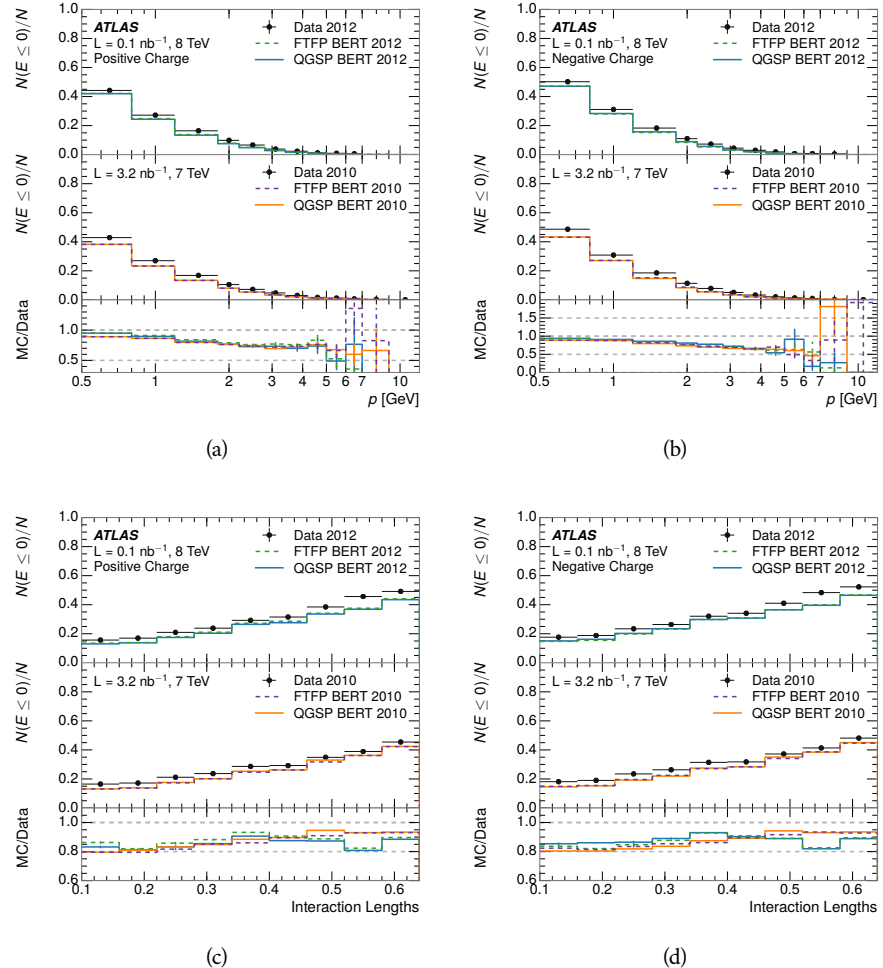


Figure 32: The fraction of tracks as a function (a, b) of momentum, (c, d) of interaction lengths with $E \leq 0$ for tracks with positive (on the left) and negative (on the right) charge.

1456 GeV. This effect was also seen in the tails of the E/p distributions in Figure 31.
 1457 This difference is likely due to modeling of coherent neutral particle radiation
 1458 in Pythia8 that overestimates the production of π^0 near the production of the
 1459 charged particles. The discrepancy does not depend on η and thus is unlikely to
 1460 be a mismodeling of the detector. This difference can be subtracted to form a
 1461 corrected average E/p , as in Section 8.2.4.

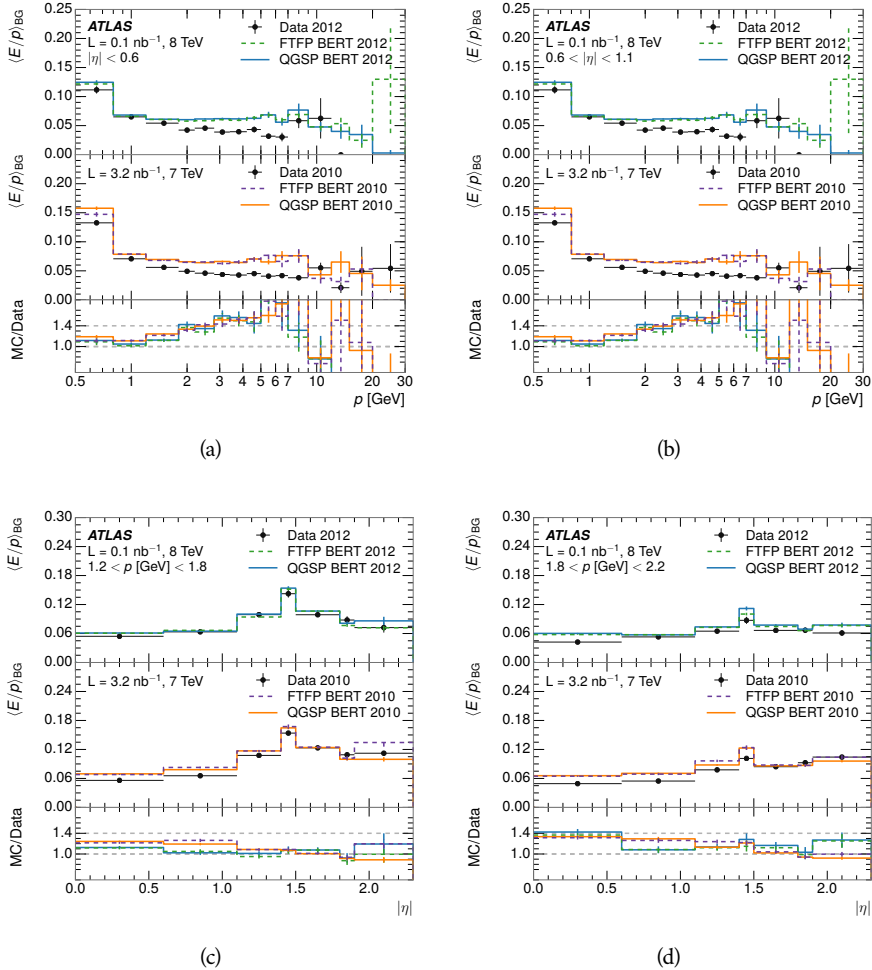


Figure 33: $\langle E/p \rangle_{BG}$ as a function of the track momentum for tracks with (a) $|\eta| < 0.6$,
 (b) $0.6 < |\eta| < 1.1$, and as a function of the track pseudorapidity for tracks
 with (c) $1.2 < p/\text{GeV} < 1.8$, (d) $1.8 < p/\text{GeV} < 2.2$.

1462 8.2.4 CORRECTED RESPONSE

1463 Figure 34 shows $\langle E/p \rangle_{COR}$ as a function of momentum for several bins of pseudo-
 1464 rapidity. This corrected $\langle E/p \rangle_{COR} \equiv \langle E/p \rangle - \langle E/p \rangle_{BG}$ measures the average
 1465 calorimeter response without the contamination of neutral particles. It is the
 1466 most direct measurement of calorimeter response in that it is the energy mea-
 1467 sured for fully isolated hadrons. The correction is performed separately in data
 1468 and simulation, so that the mismodeling of the neutral background in simulation

is removed from the comparison of response. The simulation overestimates the response at low momentum by about 5%, an effect that can be mostly attributed to the underestimation of the zero fraction mentioned previously. For $|\eta| < 0.6$, the data-simulation agreement has a larger discrepancy by about 5% for 2010 than 2012, although this is not reproduced in at higher pseudorapidity.

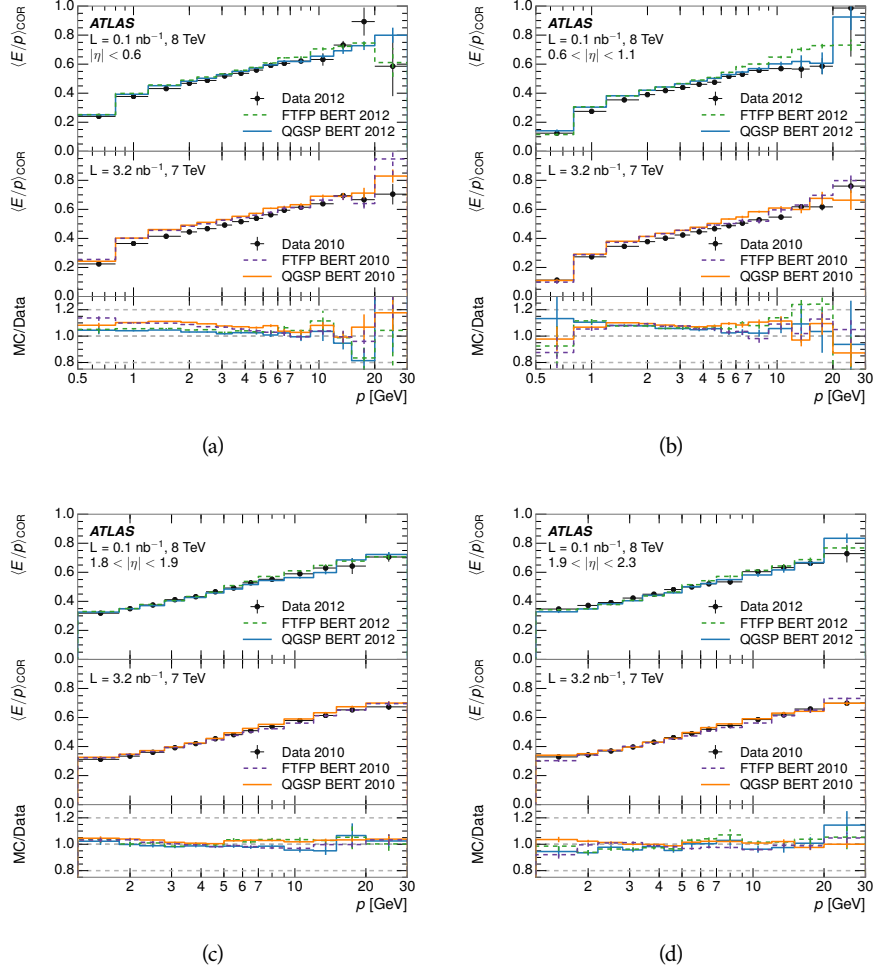


Figure 34: $\langle E/p \rangle_{\text{COR}}$ as a function of track momentum, for tracks with (a) $|\eta| < 0.6$, (b) $0.6 < |\eta| < 1.1$, (c) $1.8 < |\eta| < 1.9$, and (d) $1.9 < |\eta| < 2.3$.

The response measurement above used topological clustering at the EM scale, that is clusters were formed to measure energy but no corrections were applied to correct for expected effects like energy lost outside of the cluster or in uninstrumented material. It is also interesting to measure $\langle E/p \rangle_{\text{COR}}$ using local cluster weighted (LCW) energies, which accounts for those effects by calibrating the energy based on the properties of the cluster such as energy density and depth in the calorimeter. Figure 35 shows these distributions for tracks with zero or more clusters and separately for tracks with one or more clusters. The calibration moves the mean value of $\langle E/p \rangle_{\text{COR}}$ significantly closer to 1.0 as desired. The agreement between data and simulation improves noticeably when at least one cluster is required, as this removes the contribution from the mismodeling of

1485 the zero fraction. The good agreement in that case again demonstrates that the
 1486 difference in $\langle E/p \rangle_{\text{COR}}$ between data and simulation is caused predominantly
 1487 by the difference in zero fraction.

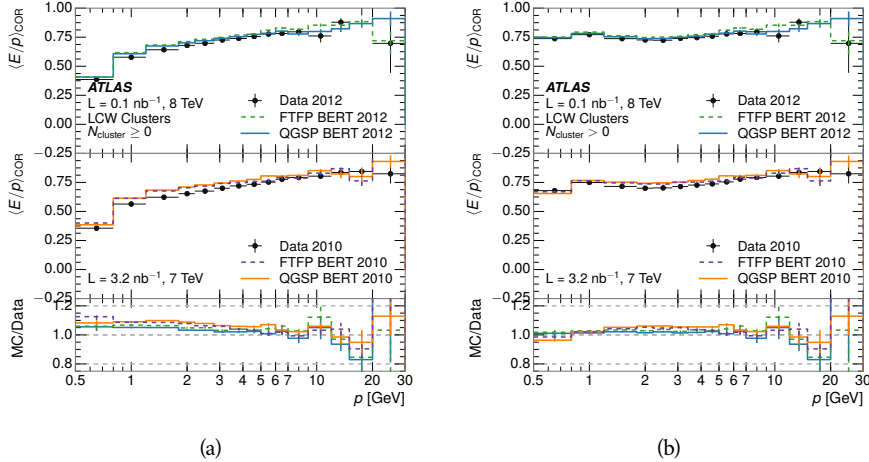


Figure 35: $\langle E/p \rangle_{\text{COR}}$ calculated using LCW-calibrated topological clusters as a function of track momentum for tracks with (a) zero or more associated topological clusters or (b) one or more associated topological clusters.

1488 8.2.5 ADDITIONAL STUDIES

1489 As has been seen in several measurements in previous sections, the simulation
 1490 does not correctly model the chance of a low momentum hadron to reach the
 1491 calorimeter. Because of the consistent discrepancy across pseudorapidity and
 1492 interaction lengths, this can be best explained by incomplete understanding of
 1493 hadronic interactions with the detector [13]. For example, a hadron that scat-
 1494 ters off of a nucleus in the inner detector can be deflected through a significant
 1495 angle and not reach the expected location in the calorimeter. In addition, these
 1496 interactions can produce secondary particles that are difficult to model.

1497 The requirement used throughout the previous sections on the number of
 1498 hits in the TRT reduces these effects by preferentially selecting tracks that do
 1499 not undergo nuclear interactions. It is interesting to check how well the sim-
 1500 ulation models tracks with low numbers of TRT hits, which selects tracks that
 1501 are more likely to have undergone a hadronic interaction. Figure 36 compares
 1502 the distributions with $N_{\text{TRT}} < 20$ to $N_{\text{TRT}} > 20$ for real and simulated particles.
 1503 As expected, the tracks with fewer hits are poorly modeled in the simulation as
 1504 $\langle E/p \rangle_{\text{COR}}$ differs by as much as 25% at low momentum.

1505 Another interesting aspect of the simulation is the description of antiprotons
 1506 at low momentum, where QGSP_BERT and FTFP_BERT have significant differ-
 1507 ences. This can be seen to have an effect in the inclusive response measurement
 1508 when separated into positive and negative charge. The $\langle E/p \rangle_{\text{COR}}$ distributions
 1509 for positive and negative particles are shown in Figure 37, where a small differ-
 1510 ence between QGSP_BERT and FTFP_BERT can be seen in the distribution for

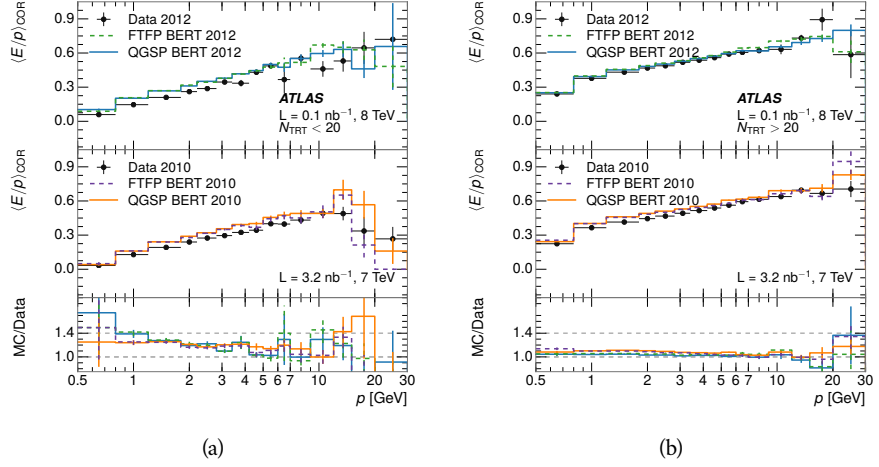


Figure 36: Comparison of the $\langle E/p \rangle_{\text{COR}}$ for tracks with (a) less than and (b) greater than 20 hits in the TRT.

negative tracks. This is demonstrated more clearly in Figure 38, which shows the E/p distribution in the two simulations separated by charge. There is a clear difference around $E/p > 1.0$, which can be explained by the additional energy deposited by the annihilation of the antiproton in the calorimeter that is modeled well only in FTFP_BERT. This is also explored with data using identified antiprotons in Section 8.3.

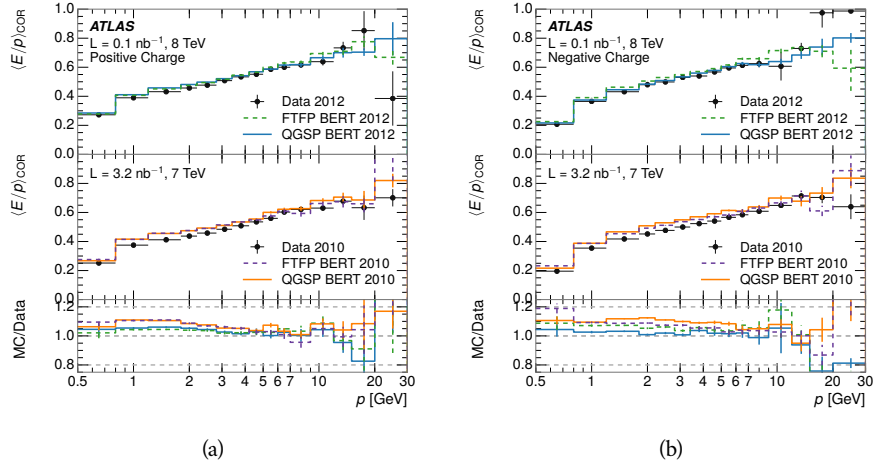


Figure 37: Comparison of the $\langle E/p \rangle_{\text{COR}}$ for (a) positive and (b) negative tracks as a function of track momentum for tracks with $|\eta| < 0.6$.

The $\langle E/p \rangle$ results in previous sections have considered the electromagnetic and hadronic calorimeters together as a single energy measurement, to emphasize the total energy deposited for a given particle. However, the deposits in each calorimeter are available separately and $\langle E/p \rangle$ can be constructed for each layer. As the layers are composed of different materials and are modeled separately in the detector geometry, confirmation that the simulation matches the data well

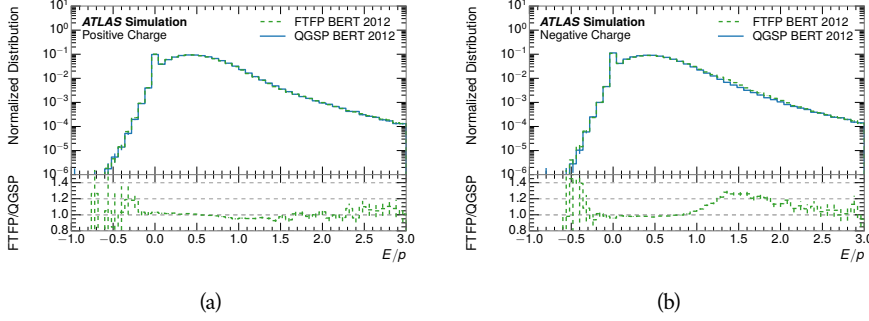


Figure 38: Comparison of the E/p distributions for (a) positive and (b) negative tracks with $0.8 < p/\text{GeV} < 1.2$ and $|\eta| < 0.6$, in simulation with the FTFP_BERT and QGSP_BERT physics lists.

in each layer adds confidence in both the description of hadronic interactions with the two different materials and also the geometric description of each.

The technique discussed in Section 8.2.3 for selecting MIPs in the electromagnetic calorimeter is also useful in studying deposits in the hadronic calorimeter. Those MIPs deposit almost all of their energy exclusively in the hadronic calorimeter. Figure 39 shows $\langle E/p \rangle_{\text{RAW}}^{\text{Had}}$, where RAW indicates that no correction has been applied for neutral backgrounds and Had indicates that only clusters for the hadronic calorimeter are included. The RAW and COR versions of $\langle E/p \rangle$ in this case are the same, as the neutral background is negligible in that calorimeter layer. The distributions are shown both for the original EM scale calibration and after LCW calibration. The data and simulation agree very well in this comparison, except in the lowest momentum bin which has 5% discrepancy that has already been seen in similar measurements.

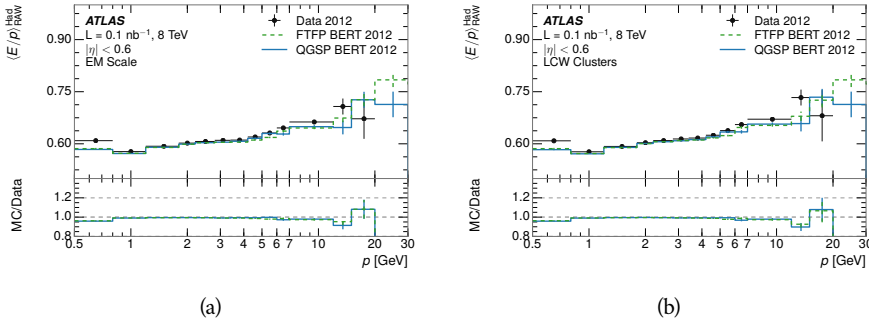


Figure 39: Comparison of the response of the hadronic calorimeter as a function of track momentum (a) at the EM-scale and (b) after the LCW calibration.

A similar comparison can be made in the electromagnetic calorimeter by selecting particles which have no associated energy in the hadronic calorimeter. These results are measured in terms of $\langle E/p \rangle_{\text{COR}}^{\text{EM}}$, where EM designates that only clusters in the electromagnetic calorimeter are included and COR designates that the neutral background is subtracted as the neutral background is present in this case. Figure 40 shows the analogous comparisons to Figure 39 in

1542 the electromagnetic calorimeter. In this case the disagreement between data and
 1543 simulation is more pronounced, with discrepancies as high as 5% over a larger
 1544 range of momenta. This level of discrepancy indicates that the description of
 1545 the electromagnetic calorimeter is actually the dominant source of discrepancy
 1546 in the combined distributions in Section 8.2.4.

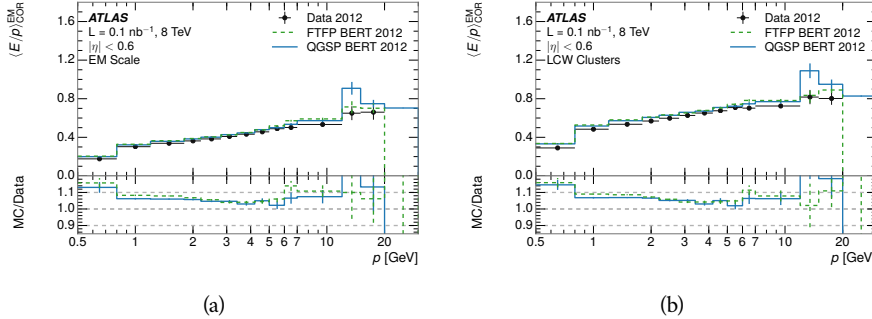


Figure 40: Comparison of the response of the EM calorimeter as a function of track momentum (a) at the EM-scale and (b) with the LCW calibration.

1547 **NOTE: There are more studies that I skipped for brevity that could be in-**
 1548 **cluded if interesting. E/p at different cluster threshold settings, E/p with**
 1549 **pileup, E/p with cells. I also left out a lot of eta bins that appear in the**
 1550 **paper so that this section didn't turn into 20 pages of plots.**

1551 8.3 IDENTIFIED PARTICLE RESPONSE

1552 The inclusive response measurement for hadrons can be augmented by measur-
 1553 ing the response for specific particle species. The simulation models each parti-
 1554 cle type separately, and understanding the properties of each is important in con-
 1555 straining the uncertainty on jets. In order to select and measure specific hadrons,
 1556 this section relies on the displaced decays of long-lived particles. Such decays
 1557 can be identified by reconstructing secondary vertices with a requirement on
 1558 mass. In particular, Λ , $\bar{\Lambda}$, and K_S^0 can be used to select a pure sample of protons,
 1559 antiprotons, and pions, respectively.

1560 8.3.1 DECAY RECONSTRUCTION

1561 The measurement of response for identified particles uses the same selection as
 1562 for inclusive particles (Section 8.1.3) with a few additions. Each event used is
 1563 required to have at least one secondary vertex, and the tracks are required to
 1564 match to that vertex rather than the primary vertex. Pions are selected from
 1565 decays of $K_S^0 \rightarrow \pi^+ \pi^-$, which is the dominant decay for K_S^0 to charged particles.
 1566 Protons are selected from decays of $\Lambda \rightarrow \pi^- p$ and antiprotons from $\bar{\Lambda} \rightarrow \pi^+ \bar{p}$,
 1567 which are similarly the dominant decays of Λ and $\bar{\Lambda}$ to charged particles. The
 1568 species of parent hadron in these decays is determined by reconstructing the
 1569 mass of the tracks associated to the secondary vertex. The sign of the higher

1570 momentum decay particle can distinguish between Λ and $\bar{\Lambda}$, which of course
 1571 have the same mass, as the proton or antiproton is kinematically favored to have
 1572 higher momentum. Examples of the reconstructed masses used to select these
 1573 decays are shown in Figure 41.

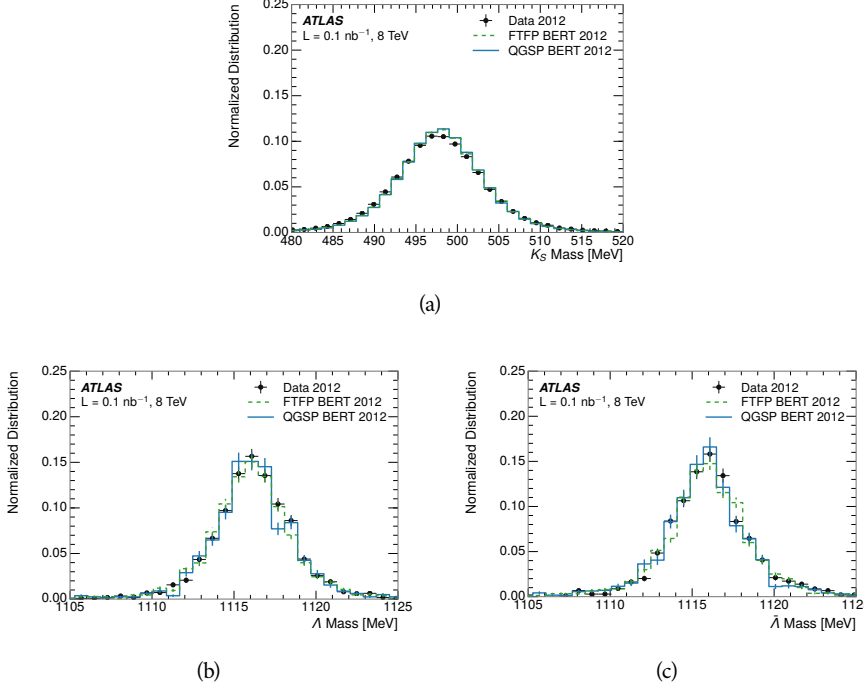


Figure 41: The reconstructed mass peaks of (a) K_S^0 , (b) Λ , and (c) $\bar{\Lambda}$ candidates.

1574 The dominant backgrounds for the identified particle decays are nuclear in-
 1575 teractions and combinatoric sources. These are suppressed by the kinematic re-
 1576 quirements on the tracks as well as an additional veto which removes candidates
 1577 that are consistent with both a Λ or $\bar{\Lambda}$ and a K_S^0 hypothesis, which is possible
 1578 because of the different assumptions on particle mass in each case [14]. After
 1579 these requirements, the backgrounds are found to be negligible compared to the
 1580 statistical errors on these measurements.

1581 8.3.2 IDENTIFIED RESPONSE

1582 With these techniques the E/p distributions are extracted in data and simulation
 1583 for each particle species and shown in Figure 42. These distributions are shown
 1584 for a particular bin of E_a ($2.2 < E_a/\text{GeV} < 2.8$), rather than p . E_a is the energy
 1585 available to be deposited in the calorimeter: for pions $E_a = \sqrt{p^2 + m^2}$, for pro-
 1586 tons $E_a = \sqrt{p^2 + m^2} - m$, and for antiprotons $E_a = \sqrt{p^2 + m^2} + m$. The features
 1587 of the E/p distributions are similar to the inclusive case. There is a small nega-
 1588 tive tail from noise and a large fraction of tracks with zero energy from particles
 1589 which do not reach the calorimeter. The long positive tail is noticeably more
 1590 pronounced for antiprotons because of the additional energy generated by the
 1591 annihilation in addition to the neutral background.

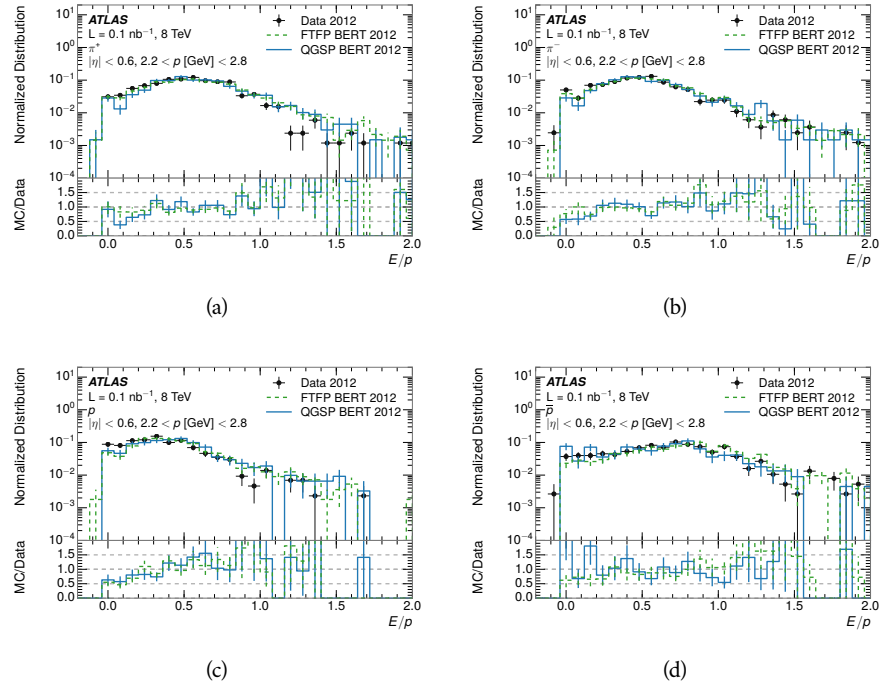


Figure 42: The E/p distribution for isolated (a) π^+ , (b) π^- , (c) proton, and (d) anti-proton tracks.

1592 The zero fraction is further explored in Figure 43 for pions and protons in data
 1593 and simulation. The simulation consistently underestimates the zero fraction
 1594 independent of particle species, which implies that this discrepancy is not caused
 1595 by the model of a particular species but rather a feature common to all.

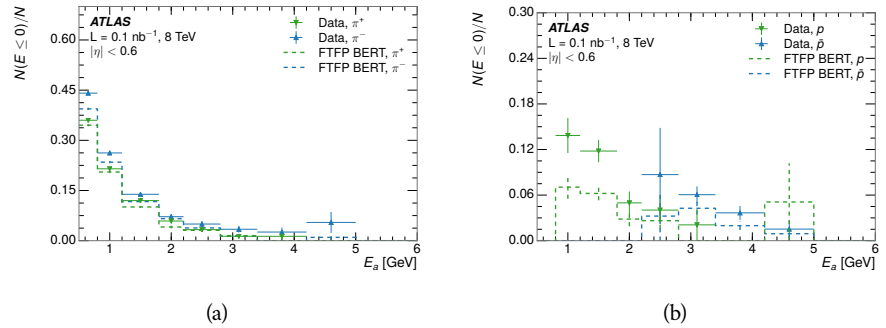


Figure 43: The fraction of tracks with $E \leq 0$ for identified (a) π^+ and π^- , and (b) proton and anti-proton tracks

1596 It is also interesting to compare the response between the different particle
 1597 species. One approach to do this is to measure the difference in $\langle E/p \rangle$ between
 1598 two types, which has the advantage of removing the neutral background. These
 1599 differences are shown in various combinations in Figure 44. The response for
 1600 π^+ is greater on average than the response to π^- because of a charge-exchange
 1601 effect which causes the production of additional neutral pions in the showers of

1602 π^+ [36]. The response for π^+ is also greater on average than the response to p ,
 1603 because a large fraction of the energy of π^+ hadrons is converted to an electro-
 1604 magnetic shower [37, 38]. However, the \bar{p} response is significantly higher than
 1605 the response to π^- because of the annihilation of the antiproton. FTFP_BERT
 1606 does a better job of modeling this effect than QGSP_BERT because of their differ-
 1607 ent descriptions of \bar{p} interactions with material.

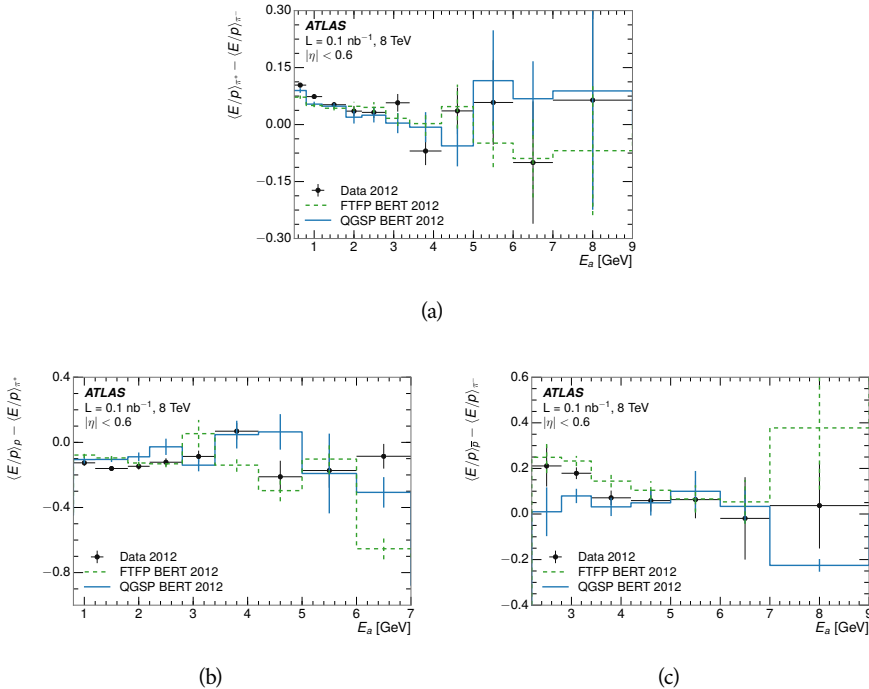


Figure 44: The difference in $\langle E/p \rangle$ between (a) π^+ and π^- (b) p and π^+ , and (c) \bar{p} and π^- .

1608 It is also possible to remove the neutral background from these response dis-
 1609 tributions using the same technique as in Section 8.2.3. The technique is largely
 1610 independent of the particle species and so can be directly applied to $\langle E/p \rangle$ for
 1611 pions. The $\langle E/p \rangle_{\text{COR}}$ distributions for pions are shown in Figure 45, which are
 1612 very similar to the inclusive results. The inclusive hadrons are comprised mostly
 1613 of pions, so this similarity is not surprising. It is also possible to see the small
 1614 differences between π^+ and π^- response here, where $\langle E/p \rangle_{\text{COR}}$ is higher on av-
 1615 erage for π^+ . The agreement between data and simulation is significantly worse
 1616 for the π^- distributions than for the π^+ , with a discrepancy greater than 10%
 1617 below 2-3 GeV.

1618 8.3.3 ADDITIONAL SPECIES IN SIMULATION

1619 The techniques above provide a method to measure the response separately for
 1620 only pions and protons. However the hadrons which forms jets include a num-
 1621 ber of additional species such as kaons and neutrons. The charged kaons are
 1622 an important component of the inclusive charged hadron distribution, which is
 1623 comprised of roughly 60-70% pions, 15-20% kaons, and 5-15% protons. These

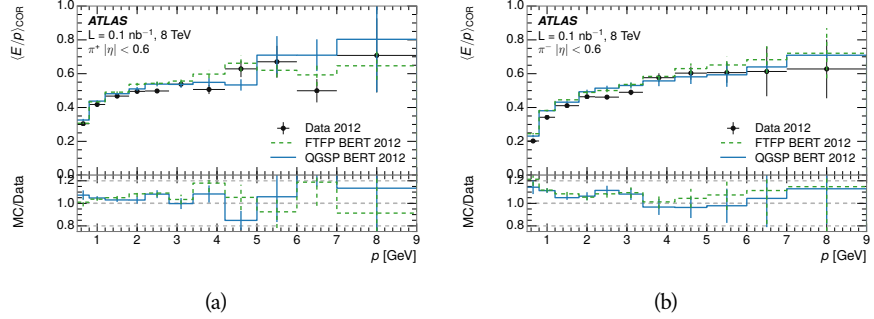


Figure 45: $\langle E/p \rangle_{\text{COR}}$ as a function of track momentum for (a) π^+ tracks and (b) π^- tracks.

1624 are difficult to measure in data at the ATLAS detector, although a template sub-
 1625 traction technique has been proposed which may be effective with larger sample sizes [13]. The simulation of these particles includes noticeable differences in
 1626 response at low energies, which are shown in Figure 46 for FTFP_BERT. The
 1627 significant differences in response between low energy protons and antiprotons
 1628 are accounted for above in the definitions of E_a .
 1629

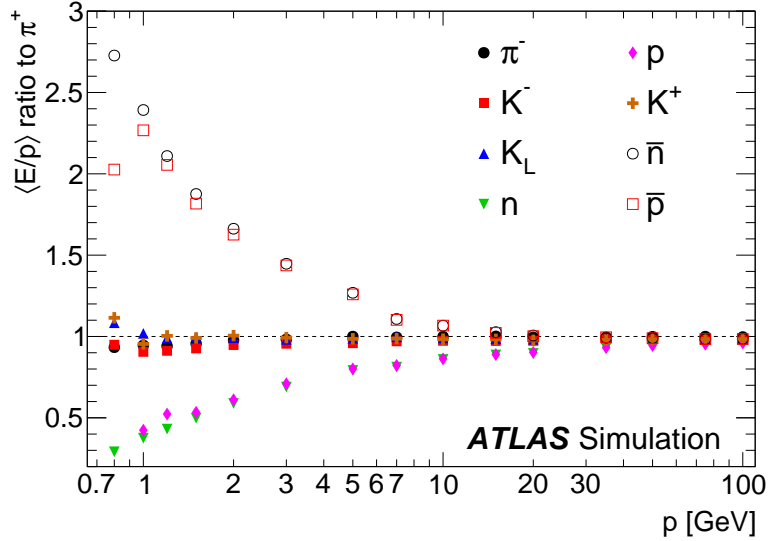


Figure 46: The ratio of the calorimeter response to single particles of various species to the calorimeter response to π^+ with the physics list FTFP_BERT.

1630 8.4 SUMMARY

1631 These various measurements of calorimeter response shown above for data and
 1632 simulation illuminate the accuracy of the simulation of hadronic interactions at
 1633 the ATLAS detector. The results were done using 2010 and 2012 data at 7 and 8
 1634 TeV, but reflect the most current understanding of the detector alignment and
 1635 geometry. A number of measurements focusing on a comparison between pro-

1636 tons and antiprotons suggest that FTFP_BERT models those interaction more
1637 accurately than QGSP_BERT. These measurements, among others, were the moti-
1638 vation to switch the default Geant4 simulation from FTFP_BERT to QGSP_BERT
1639 for all ATLAS samples.

1640 Even with these updates, there are a number of small, approximately 5%, dis-
1641 crepancies in response between the data and simulation at low energies. At
1642 higher energies the simulation of hadronic interactions is very consistent with
1643 data. Chapter 9 discusses how to use these observed differences to constrain the
1644 jet energy scale and its associated uncertainties.

1645

1646 JET ENERGY RESPONSE AND UNCERTAINTY

1647 9.1 MOTIVATION

1648 As jets form a major component of many physics analyses at ATLAS, it is crucial
 1649 to carefully calibrate the measurement of jet energies and to derive an uncer-
 1650 tainty on that measurement. These uncertainties have often been the dominant
 1651 systematic uncertainty in high-energy analyses at the LHC. Dijet and multijet
 1652 balance techniques provide a method to constrain the JES and its uncertainty in
 1653 data, and provide the default values used for ATLAS jet measurements at most
 1654 energies [39]. These techniques are limited by their reliance on measuring jets
 1655 in data, so they are statistically limited in estimating the jet energy scale at the
 1656 highest jet energies. This chapter presents another method for estimating the jet
 1657 energy scale and its uncertainty which builds up a jet from its components and
 1658 thus can be naturally extended to high jet momentum. Throughout this chapter
 1659 the jets studied are simulated using Pythia8 with the CT10 parton distribution
 1660 set [40] and the AU2 tune [17], and corrections are taken from the studies includ-
 1661 ing data and simulation in Chapter 8.

1662 As described in Section 7.2, jets are formed from topological clusters of energy
 1663 in the calorimeters using the anti- k_t algorithm. These clusters originate from a
 1664 diverse spectrum of particles, in terms of both species and momentum, leading to
 1665 significantly varied jet properties and response between jets of similar produced
 1666 momentum. Figure 47 shows the simulated distribution of particles within jets
 1667 at a few examples energies. The E/p measurements provide a thorough under-
 1668 standing of the dominant particle content of jets, the charged hadrons.

1669 9.2 UNCERTAINTY ESTIMATE

1670 Simulated jets are not necessarily expected to correctly model the energy de-
 1671 posits in the calorimeters, because of the various discrepancies discussed in Chap-
 1672 ter 8. To evaluate a jet energy response, the simulated jet energies are compared
 1673 to a corrected jet built up at the particle level. Each cluster in a jet is associated
 1674 to the truth particle which deposited it, and the energy in that cluster is then
 1675 corrected for a number of effects based on measurements in data. The primary
 1676 corrections come from the single hadron response measurements in addition to
 1677 response measured using the combined test beam which covers higher momen-
 1678 tum particles [41]. These corrections include both a shift (Δ), in order to make
 1679 the simulation match the average response in data, and an uncertainty (σ) asso-
 1680 ciated with the ability to constrain the difference between data and simulation.
 1681 Some of the dominant sources of uncertainty are itemized in Table 5 with typi-
 1682 cal values, and the full list considered is described in detail in the associated pa-

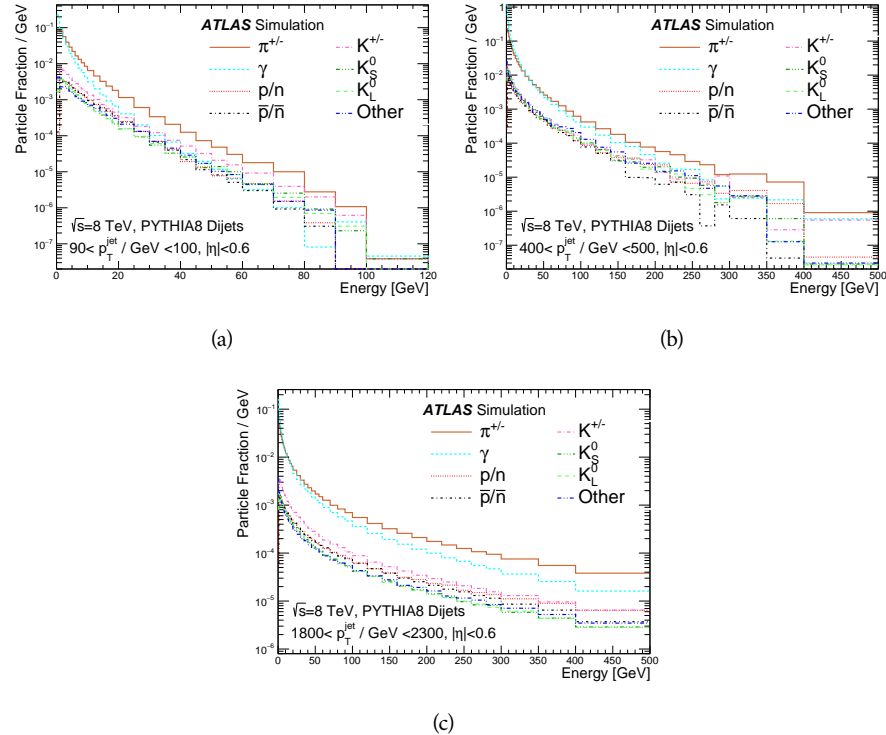


Figure 47: The spectra of true particles inside anti- k_t , $R = 0.4$ jets with (a) $90 < p_T/\text{GeV} < 100$, (b) $400 < p_T/\text{GeV} < 500$, and (c) $1800 < p_T/\text{GeV} < 2300$.

1683 per [13]. These uncertainties cover differences between the data and simulation
 1684 in the modeling of calorimeter response to a given particle. No uncertainties are
 1685 added for the difference between particle composition of jets in data and simu-
 1686 lation.

1687 From these terms, the jet energy scale and uncertainty is built up from indi-
 1688 vidual energy deposits in simulation. Each uncertainty term is treated indepen-
 1689 dently, and are taken to be gaussian distributed. The resulting scale and uncer-
 1690 tainty is shown in Figure 48, where the mean response is measured relative to
 1691 the calibrated energy reported by simulation. The dominant uncertainties come
 1692 from the statistical uncertainties on the E/p measurements at lower energies and
 1693 the additional uncertainty for out of range measurements at higher energies. The
 1694 total uncertainty from this method at intermediate jet energies is comparable to
 1695 other simulation-based methods [42] and is about twice as large as in-situ meth-
 1696 ods using data [39]. This method is the only one which provides an estimation
 1697 above 1.8 TeV, however, and so is still a crucial technique in analyses that search
 1698 for very energetic jets.

1699 These techniques can also be used to measure the correlation between bins of
 1700 average reconstructed jet momentum across a range of p_T and $|\eta|$, where cor-
 1701 relations are expected because of a similarity in particle composition at similar
 1702 energies. Figure 49 shows these correlations, where the uncertainties on jets in
 1703 neighboring bins are typically between 30% and 60% correlated. The uncertainty
 1704 on all jets becomes significantly correlated at high energies and larger pseudora-

Abbrev.	Description	Δ (%)	σ (%)
In situ E/p	The comparison of $\langle E/p \rangle_{\text{COR}}$ as described in Chapter 8 with statistical uncertainties from 500 MeV to 20 GeV.	0-3	1-5
CTB	The main $\langle E/p \rangle$ comparison uncertainties, binned in p and $ \eta $, as derived from the combined test beam results, from 20 to 350 GeV [41].	0-3	1-5
E/p Zero Fraction	The difference in the zero-fraction between data and MC simulation from 500 MeV to 20 GeV.	5-25	1-5
E/p Threshold	The uncertainty in the EM calorimeter response from the potential mismodeling of threshold effects in topological clustering.	0	0-10
Neutral	The uncertainty in the calorimeter response to neutral hadrons based on studies of physics model variations.	0	5-10
K_L	An additional uncertainty in the response to neutral K_L in the calorimeter based on studies of physics model variations.	0	20
E/p Misalignment	The uncertainty in the p measurement from misalignment of the ID.	0	1
Hadrons, $p > 350$ GeV	A flat uncertainty for all particles above the energy range or outside the longitudinal range probed with the combined test beam.	0	10

Table 5: The dominant sources of corrections and systematic uncertainties in the [JES](#) estimation technique, including typical values for the correcting shift (Δ) and the associated uncertainty (σ).

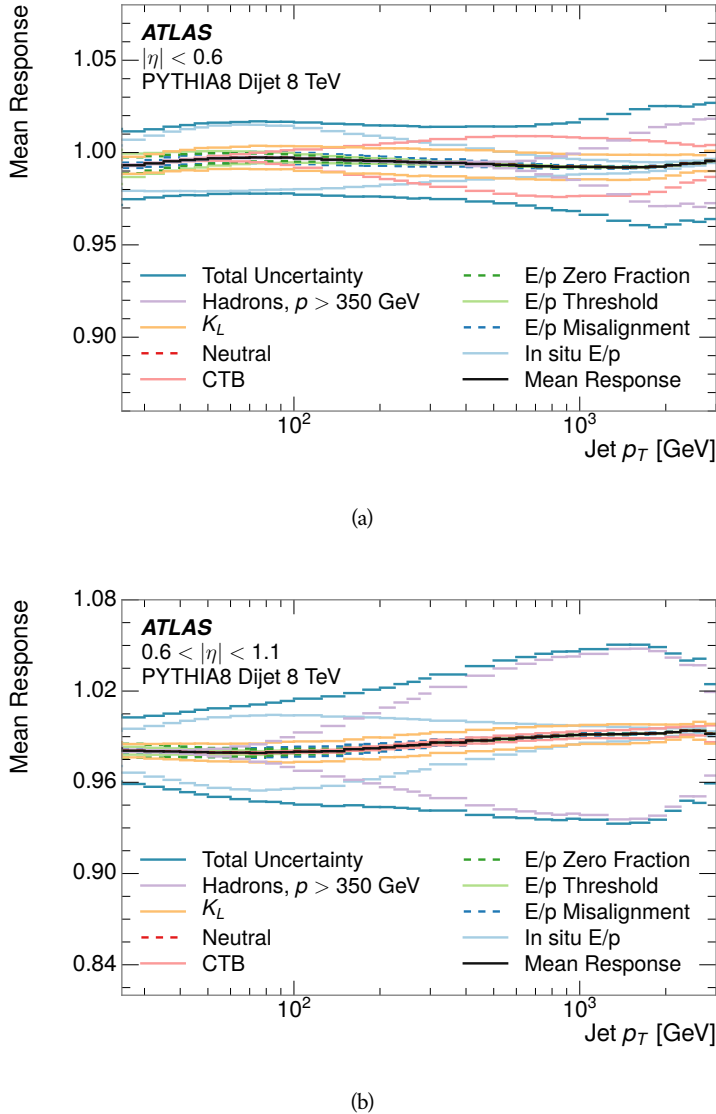


Figure 48: The [JES](#) uncertainty contributions, as well as the total [JES](#) uncertainty, as a function of jet p_T for (a) $|\eta| < 0.6$ and (b) $0.6 < |\eta| < 1.1$.

1705 pidities, when the uncertainty becomes dominated by the single term reflecting
 1706 out of range particles.

1707 9.3 SUMMARY

1708 The technique described above provides a jet energy scale and uncertainty by
 1709 building up jet corrections from the energy deposits of constituent particles. The
 1710 E/p measurements are crucial in providing corrections for the majority of parti-
 1711 cles in the jets. The uncertainty derived this way is between 2 and 5% and is about
 1712 twice as large at corresponding momentum than jet balance methods. However
 1713 this is the only uncertainty available for very energetic jets using 2012 data and
 1714 simulation, and repeating this method with Run 2 data and simulation will be

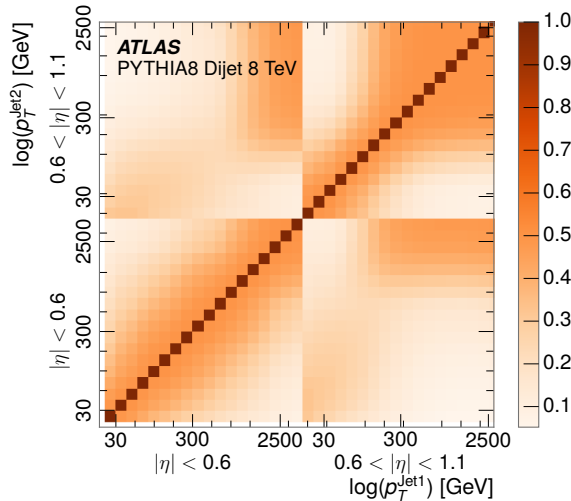


Figure 49: The JES correlations as a function of jet p_T and $|\eta|$ for jets in the central region of the detector.

1715 important in providing an uncertainty for the most energetic jets in 13 TeV col-
 1716 lisions.

1717

PART V

1718

SEARCH FOR LONG-LIVED PARTICLES

1719

You can put some informational part preamble text here.

1720

1721 LONG-LIVED PARTICLES IN ATLAS

1722 As discussed in Section 2.3, various limitations in the SM suggest a need for new
 1723 particles at the TeV scale. A wide range of extensions to the Standard Model
 1724 predict that these new particles can have lifetimes greater than approximately
 1725 one-hundredth of a nanosecond. These include theories with universal extra-
 1726 dimensions [43, 44], with new fermions [45], and with leptoquarks [46]. Many
 1727 SUSY theories also produce these Long-Lived Particles (LLPs), in both R-Parity
 1728 violating [47–49] and R-Parity conserving [50–53] formulations. Split super-
 1729 symmetry [54, 55], for example, predicts long-lived gluinos with O(TeV) masses.
 1730 This search focuses specifically on the SUSY case, but many of the results are
 1731 generic to any model with LLPs.

1732 Long-lived gluinos or squarks carry color-charge and will thus hadronize into
 1733 color neutral bound states called R-Hadrons. These are composit particles like
 1734 the usual hadrons but with one supersymmetric constituent, for example $\tilde{g}q\bar{q}$
 1735 and $\tilde{q}\bar{q}$. Through this hadronization process, the neutral gluino can acquire a
 1736 charge. Gluino pair production, $pp \rightarrow \tilde{g}\tilde{g}$ has the largest cross sectional increase
 1737 with the increase in energy to 13 TeV, and so this search focuses on gluino R-
 1738 Hadrons. Planned future updates will extend the case to explicitly include squark
 1739 and chargino models, but the method covers any long-lived, charged, massive
 1740 particle.

1741 10.1 EVENT TOPOLOGY

1742 The majority of SUSY models predict that gluinos will be produced in pairs at
 1743 the LHC, through processes like $pp \rightarrow q\bar{q} \rightarrow \tilde{g}\tilde{g}$ and $pp \rightarrow gg \rightarrow \tilde{g}\tilde{g}$, where the
 1744 gluon mode dominates for the collision energy and gluino masses considered
 1745 for this search. During their production, the long-lived gluinos hadronize into
 1746 color singlet bound states including $\tilde{g}q\bar{q}$, $\tilde{g}qqq$, and even $\tilde{g}g$ [56]. The probability
 1747 to form the gluon-only bound states is a free parameter usually taken to be 0.1,
 1748 while the meson states are favored among the R-Hadrons [57]. The charged and
 1749 neutral states are approximately equally likely for mesons, so the R-Hadrons will
 1750 be charged roughly 50% of the time.

1751 These channels produce R-Hadrons with large p_T , comparable to their mass,
 1752 so that they typically propagate with $0.2 < \beta < 0.9$ [57]. The fragmentation that
 1753 produces these hadrons is very hard, so the jet structure around the R-Hadron
 1754 is minimal, with less than 5 GeV of summed particle momentum expected in a
 1755 cone of $\Delta R < 0.25$ around the R-Hadron [57]. After hadronization, depending
 1756 on the gluino lifetime, the R-Hadrons then decay into hadrons and a LSP [56].

1757 In summary, the expected event for pair-produced long-lived gluinos is very
 1758 simple: two isolated, high-momentum R-Hadrons that propagate through the
 1759 detector before decaying into jets. The observable features of such events depend

1760 strongly on the interaction of the R-Hadron with the material of the detector and
 1761 also its lifetime. Section 10.1.1 describes the interactions of R-Hadrons which
 1762 reach the various detector elements in ATLAS and Section 10.1.2 provides a sum-
 1763 mary of the observable event descriptions for R-Hadrons of various lifetimes.

1764 10.11 DETECTOR INTERACTIONS

1765 After approximately 0.2 ns, the R-Hadron reaches the pixel detector. If charged,
 1766 it deposits energy into the material through repeated single collisions that result
 1767 in ionization of the silicon substrate [7]. Because of its comparatively low β , the
 1768 ionization energy can be significantly greater than expected for SM particles be-
 1769 cause the most-probable energy loss grows significantly as β decreases [7]. This
 1770 large ionization can be measured through the time over threshold (ToT) read out
 1771 from the pixel detector as described in Section 7.1.1.2. Large ionization in the
 1772 inner detector is one of the major characteristic features of LLPs.

1773 Throughout the next few nanoseconds, the R-Hadron propagates through the
 1774 remainder of the inner detector. A charged R-Hadron will provide hits in each
 1775 of these systems as would any other charged particle, and can be reconstructed
 1776 as a track. The track reconstruction provides a measurement of its trajectory
 1777 and thus its momentum as described in Section 7.1. The large momentum is
 1778 another characteristic feature of massive particles produced at the LHC. **Note: At**
1779 this point I am failing to mention that the TRT provides a possible dE/dx
1780 measurement, because no one uses it as far as I know.

1781 As of roughly 20 ns, the R-Hadron enters the calorimeter where it interacts
 1782 hadronically with the material. Because of its large mass and momentum, the
 1783 R-Hadron does not typically stop in the calorimeter, but rather deposits a small
 1784 fraction of its energy through repeated interactions with nucleons. The proba-
 1785 bility of interaction between the gluino itself and a nucleon is low because the
 1786 cross section drops off with the inverse square of its mass, so the interactions are
 1787 primarily governed by the light constituents [58]. Each of these interactions can
 1788 potentially change that quark content and thus change the sign of the R-Hadron,
 1789 so that the charge at exit is typically uncorrelated with the charge at entry [57].
 1790 The total energy deposited in the calorimeters during the propagation is small
 1791 compared to the kinetic energy of the R-Hadron, around 20-40 GeV, so that
 1792 E/p is typically less than 0.1 [57].

1793 Then, 30 ns after the collision, it reaches the muon system, where it again
 1794 ionizes in the material if charged and can be reconstructed as a muon track. Be-
 1795 cause of the charge-flipping interactions in the calorimeter, this track may have
 1796 the opposite sign of the track reconstructed in the inner detector, or there may
 1797 be a track present when there was none in the inner detector and vice-versa. The
 1798 propagation time at the typically lower β results in a significant delay compared
 1799 to muons, and that delay can be assessed in terms of a time-of-flight measure-
 1800 ment. Because of the probability of charge-flip and late arrival, there is a signif-
 1801 icant chance that an R-Hadron which was produced with a charge will not be
 1802 identified as a muon. The long time-of-flight is another characteristic feature of
 1803 R-Hadrons which are reconstructed as muons.

1804 10.1.2 LIFETIME DEPENDENCE

1805 The above description assumed a lifetime long enough for the R-Hadron to exit
 1806 the detector, which through this search is referred to as “stable”, even though
 1807 the particle may decay after exiting the detector. There are several unique sig-
 1808 natures at shorter lifetimes where the R-Hadron decays in various parts of the
 1809 inner detector; these lifetimes are referred to as “metastable”.

1810 The shortest case where the R-Hadron is considered metastable is for life-
 1811 times around 0.01 ns, where the particle decays before reaching any of the de-
 1812 tector elements. Although the R-Hadrons are produced opposite each other in
 1813 the transverse plane, each R-Hadron decays to a jet and an [LSP](#). The [LSPs](#) are not
 1814 measured, so the produced jets can be significantly imbalanced in the transverse
 1815 plane which results in large missing energy. That missing energy can be used
 1816 to trigger candidate events, and provides the most efficient trigger option for
 1817 shorter lifetimes. Additionally, the precision of the tracking system allows the
 1818 displaced vertex of the R-Hadron decay to be reconstructed from the charged
 1819 particles in the jet. The distance of that vertex from the interaction point can
 1820 be used to distinguish R-Hadron decays from other processes. Figure 50 shows
 1821 a schematic diagram of an example R-Hadron event with such a lifetime. The
 1822 diagram is not to scale, but instead illustrates the detector interactions in the
 1823 pixel detector, calorimeters, and muon system. It includes a representation of
 1824 the charged R-Hadron and the neutral R-Hadron, as well as the [LSPs](#) and jets
 1825 (shown as charged hadrons) produced in the decay. Neutral hadrons may also
 1826 be produced in the decay but are not depicted. Previous searches on [ATLAS](#) have
 1827 used the displaced vertex to target [LLP](#) decays [59].

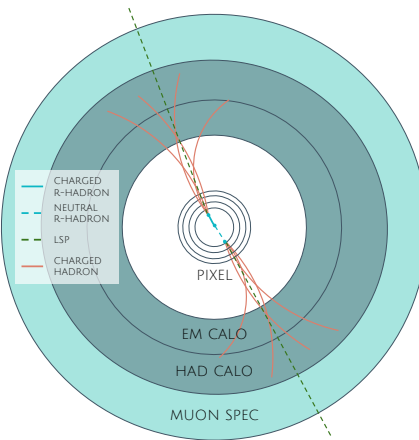


Figure 50: A schematic diagram of an R-Hadron event with a lifetime around 0.01 ns.
 The diagram includes one charged R-Hadron (solid blue), one neutral R-Hadron (dashed blue), [LSPs](#) (dashed green) and charged hadrons (solid orange).
 The pixel detector, calorimeters, and muon system are illustrated but not to scale.

1828 The next distinguishable case occurs at lifetimes greater than 0.1 ns, where
 1829 the R-Hadron forms a partial track in the inner detector. If the decay products
 1830 are sufficiently soft, they may not be reconstructed, and this forms a unique sig-

1831 nature of a disappearing track. An example of such an event is illustrated in
 1832 Figure 51, which shows the short track in the inner detector and the undetected
 1833 soft charged hadron and LSP that are produced. A dedicated search on ATLAS used
 1834 the disappearing track signature to search for LLP in Run 1 [60]. **zNote: might**
 1835 **not be worth mentioning the disappearing track here since it is actually a**
 1836 **chargino search, the soft pion is pretty unique to charginos.**

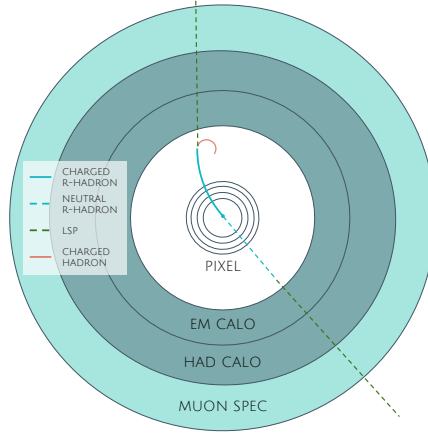


Figure 51: A schematic diagram of an R-Hadron event with a lifetime around 4 ns. The diagram includes one charged R-Hadron (solid blue), one neutral R-Hadron (dashed blue), LSPs (dashed green) and a charged hadron (solid orange). The pixel detector, calorimeters, and muon system are illustrated but not to scale.

1837 If the decay products are not soft, the R-Hadron daughters form jets, resulting
 1838 in an event-level signature of up to two high-momentum tracks, jets, and signif-
 1839 icant missing energy. The missing energy has the same origin as in the case of
 1840 0.01 ns lifetimes, from the decay to unmeasured particles, and again can be large.
 1841 The high-momentum tracks will also have the characteristically high-ionization
 1842 of massive, long-lived particles in the inner detector. Figure 52 illustrates an ex-
 1843 ample event with one charged R-Hadron which decays after approximately 10 ns,
 1844 and shows how the jets from the decay can still be reconstructed in the calorime-
 1845 ter. Several previous searches on ATLAS from Run 1 have used this signature to
 1846 search for R-Hadrons [61, 62], including a dedicated search for metastable parti-
 1847 cles [63].

1848 If the lifetime is longer than several nanoseconds, in the range of 15-30 ns,
 1849 the R-Hadron decay can occur in or after the calorimeters, but prior to reaching
 1850 the muon system. This case is similar to the above, although the jets may not be
 1851 reconstructed, and is covered by many of the same search strategies. The events
 1852 still often have large missing energy, although it is generated through different
 1853 mechanisms. The R-Hadrons do not deposit much energy in the calorimeters, so
 1854 a neutral R-Hadron will not enter into the missing energy calculation. A charged
 1855 R-Hadron opposite a neutral R-Hadron will thus generate significant missing en-
 1856 ergy, and close to 50% of pair-produced R-Hadron events fall into this category.
 1857 If both R-Hadrons are neutral then the missing energy will be low because nei-
 1858 ther is detected. Two charged R-Hadrons will also result in low missing energy
 1859 because both are reconstructed as tracks and will balance each other in the trans-

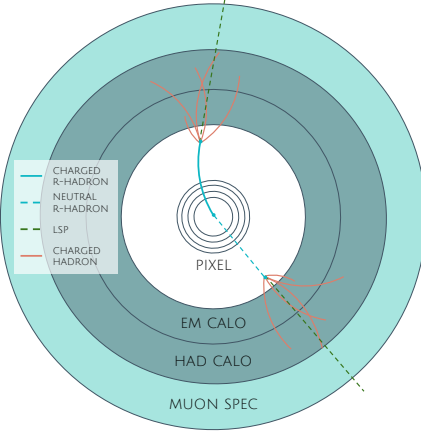


Figure 52: A schematic diagram of an R-Hadron event with a lifetime around 5 ns. The diagram includes one charged R-Hadron (solid blue), one neutral R-Hadron (dashed blue), LSPs (dashed green) and charged hadrons (solid orange). The pixel detector, calorimeters, and muon system are illustrated but not to scale.

1860 verse plane. A small fraction of the time, one of the charged R-Hadron tracks may
 1861 fail quality requirements and thus be excluded from the missing energy calcula-
 1862 tion and again result in significant missing energy. Figure 53 illustrates another
 1863 example event with one charged R-Hadron which decays after approximately 20
 1864 ns, and shows how the jets from the decay might not be reconstructed.

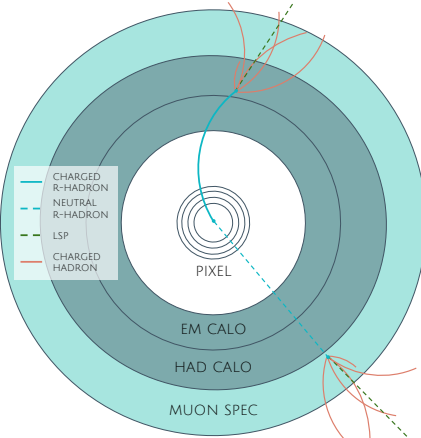


Figure 53: A schematic diagram of an R-Hadron event with a lifetime around 20 ns. The diagram includes one charged R-Hadron (solid blue), one neutral R-Hadron (dashed blue), LSPs (dashed green) and charged hadrons (solid orange). The pixel detector, calorimeters, and muon system are illustrated but not to scale.

1865 The longest lifetimes, the stable case, has all of the features of the 30-50 ns case
 1866 but with the addition of muon tracks for any R-Hadrons that exit the calorimeter
 1867 with a charge. That muon track can provide additional information from time-
 1868 of-flight measurements to help identify LSPs. An example of the event topology
 1869 for one charged and one neutral stable R-Hadron is shown in Figure 54. Some
 1870 searches on ATLAS have included this information to improve the search reach
 1871 for stable particles [62, 64].

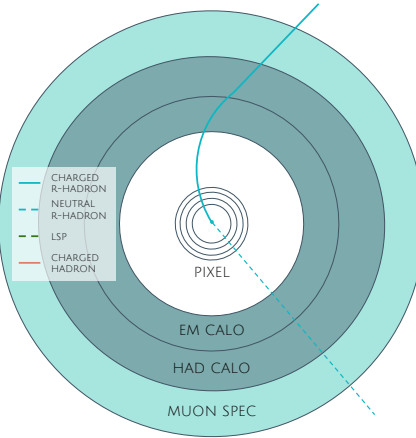


Figure 54: A schematic diagram of an R-Hadron event with a lifetime around 20 ns. The diagram includes one charged R-Hadron (solid blue) and one neutral R-Hadron (dashed blue). The pixel detector, calorimeters, and muon system are illustrated but not to scale.

1872 10.2 SIMULATION

1873 All of the event topologies discussed above are explored by simulations of R-
 1874 Hadron events in the [ATLAS](#) detector. A large number of such samples are gen-
 1875 erated to determine signal efficiencies, to measure expected yields, and to esti-
 1876 mate uncertainties. The primary interaction, pair production of gluinos with
 1877 masses between 400 and 3000 GeV, is simulated using [Pythia 6.4.27](#) [65]
 1878 with the AUET2B [66] set of tuned parameters for the underlying event and
 1879 the CTEQ6L1 [40] parton distribution function ([PDF](#)) set. The simulated inter-
 1880 actions include a modeling of pileup by adding secondary, minimum bias in-
 1881 teractions from both the same (in-time pileup) and nearby (out-of-time pileup)
 1882 bunch crossings. This event generation is then augmented with a dedicated
 1883 hadronization routine to hadronize the long-lived gluinos into final states with
 1884 R-Hadrons [67], with the probability to form a gluon-gluino bound set at 10% [68].

1885 The cross sections used for these processes are calculated at next-to-leading
 1886 order ([NLO](#)) in the strong coupling constant with a resummation of soft-gluon
 1887 emmission at next-to-leading logarithmic ([NLL](#)) [69–73]. The nominal predic-
 1888 tions and the uncertainties for each mass point are taken from an envelope of
 1889 cross-section predictions using different [PDF](#) sets and factorization and renor-
 1890 malization scales [74].

1891 The R-Hadrons then undergo a full detector simulation [], where the interac-
 1892 tions of the R-Hadrons with the material of the detector are described by dedi-
 1893 cated [Geant4](#) [10] routines. These routines model the interactions described in
 1894 Section 10.1.1, including the ionizing interactions in the silicon modules of the
 1895 inner detector and the R-Hadron-nucleon interactions in the calorimeters [75,
 1896 76]. The specific routine chosen to describe the interactions of the R-Hadrons
 1897 with nucleons, the “generic model”, uses a pragmatic approach where the scatter-
 1898 ing cross section is taken to be a constant 12 mb per light quark. In this model

1899 the gluino itself does not interact at all except through its role as a reservoir of
1900 kinetic energy.

1901 The lifetimes of these R-Hadrons are then simulated at several working points,
1902 $\tau = 0.1, 1.0, 3.0, 10, 30, 50$ and detector stable, where the particle is required to
1903 decay after propagating for a time compatible with its lifetime. Only one decay
1904 mode is simulated for these samples, $\tilde{g} \rightarrow q\bar{q}\tilde{\chi}_1^0$ with the neutralino mass set to
1905 100 GeV, which is chosen because it has the highest sensitivity among all of the
1906 modes studied in previous searches [63]. Heavier neutralinos have similar results
1907 but generate less missing energy which reduces the efficiency of triggering.

1908 All of the simulated events are then reconstructed using the same software
1909 used for collision data. The fully reconstructed events are then reweighted to
1910 match the distribution of initial state radiation in an alternative sample of events,
1911 generated with MG5_aMC@NLO [77], which has a more accurate description of ra-
1912 diate effects than Pythia6. This reweighting provides a more accurate descrip-
1913 tion of the momentum of the gluino-gluino system and is important in modeling
1914 the efficiency of triggering and offline event selection.

1915

1916 EVENT SELECTION

1917 The [LLPs](#) targeted by this search differ in their interactions with the detector from
 1918 [SM](#) particles primarily because of their large mass. When produced at the ener-
 1919 gies available at the [LHC](#), that large mass results in a low β (typically $0.2 < \beta <$
 1920 0.9). Such slow-moving particles heavily ionize in detector material. Each layer
 1921 of the pixel detector provides a measurement of that ionization, through [ToT](#), as
 1922 discussed in Section 7.1.1.2. The ionization in the pixel detector, quantified in
 1923 terms of dE/dx , provides the major focus for this search technique, along with
 1924 the momentum measured in the entire inner detector. It is effective both for its
 1925 discriminating power and its use in reconstructing a particle's mass, and it can
 1926 be used for a wide range of masses and lifetimes as discussed in Section 10.1.2.
 1927 However dE/dx needs to be augmented with a few additional selection require-
 1928 ments to provide a mechanism for triggering and to further reduce backgrounds.

1929 Ionization itself is not currently accessible for triggering, so this search in-
 1930 stead relies on E_T^{miss} to trigger signal events. Although triggering on E_T^{miss} can
 1931 be inefficient, E_T^{miss} is often large for many production mechanisms of [LLPs](#), as
 1932 discussed in Section 10.1.

1933 The use of ionization to reject [SM](#) backgrounds relies on well-measured, high-
 1934 momentum tracks, so some basic requirements on quality and kinematics are
 1935 placed on the tracks considered in this search. These quality requirements have
 1936 been significantly enhanced in Run 2 by a newly introduced tracking variable
 1937 that is very effective in removing highly-ionizing backgrounds caused by over-
 1938 lapping tracks. A few additional requirements are placed on the tracks consid-
 1939 ered for [LLP](#) candidates that increase background rejection by targeting specific
 1940 types of [SM](#) particles. These techniques provide a significant analysis improve-
 1941 ment over previous iterations of ionization-based searches on ATLAS by provid-
 1942 ing additional background rejection with minimal loss in signal efficiency.

1943 The ionization measurement with the Pixel detector can be calibrated to pro-
 1944 vide an estimator of $\beta\gamma$. That estimate, together with the momentum measure-
 1945 ment provided by tracking, can be used to reconstruct a mass for each track
 1946 which traverses the pixel detector. That mass variable will be peaked at the [LLP](#)
 1947 mass for any signal, and provides an additional tool to search for an excess. In
 1948 addition to an explicit requirement on ionization, this search constructs a mass-
 1949 window for each targeted signal mass in order to evaluate any excess of events
 1950 and to set limits.

1951 The strategy discussed here is optimized for lifetimes of $O(1) - O(10)$ ns.
 1952 Pixel ionization is especially useful in this regime as particles only need to prop-
 1953 agate through the first seven layers of the inner detector, about 37 cm from the
 1954 beam axis. The search is still competitive with other searches for [LLPs](#) at longer
 1955 lifetimes, because the primary discriminating variables are still applicable even
 1956 for particles that do not decay within the detector [64]. Although the majority of

1957 the requirements will be the same for all lifetimes, two signal regions are defined
 1958 to optimize separately for intermediate and long lifetime particles.

1959 11.1 TRIGGER

1960 Triggering remains a significant difficulty in defining an event selection with
 1961 high signal efficiency in a search for LLPs. There are no triggers available in
 1962 the current ATLAS system that can fire directly from a high momentum track
 1963 with large ionization (Section 6.6). Although in some configurations a charged
 1964 LLP can fire muon triggers, this requirement introduces significant model depen-
 1965 dence on both the allowed lifetimes and the interactions in the calorimeter [57],
 1966 as discussed in Section 10.1.1.

1967 For a search targeting particles which may decay prior to reaching the muon
 1968 system, the most efficient available trigger is based on missing energy [57]. As
 1969 discussed in Section 10.1, signal events can produce significant E_T^{miss} by a few
 1970 mechanisms. At the trigger level however, the missing energy is only calculated
 1971 using the calorimeters (Section 6.6) where the R-Hadrons deposit little energy.
 1972 So, at short lifetimes, E_T^{miss} measured in the calorimeter is generated by an im-
 1973 balance between the jets and undetected LSPs produced in R-Hadron decays. At
 1974 longer lifetimes, without the decay products, missing energy is only produced in
 1975 the calorimeters when the R-Hadrons recoil against an initial state radiation (ISR)
 1976 jet.

1977 These features are highlighted in Figure 55, which shows the E_T^{miss} distribu-
 1978 tions for simulated short lifetime (3 ns) and stable R-Hadron events. The figure
 1979 includes both the offline E_T^{miss} , the missing energy calculated with all available
 1980 information, and Calorimeter E_T^{miss} , the missing energy calculated using only
 1981 information available at the calorimeter which approximates the missing energy
 1982 available at the trigger. The short lifetime sample has significantly greater E_T^{miss}
 1983 and Calorimeter E_T^{miss} than the stable sample as expected. For the stable sam-
 1984 ple, a small fraction of events with very large E_T^{miss} (about 5%) migrate into the
 1985 bin with very small Calorimeter E_T^{miss} because the E_T^{miss} produced by a charged
 1986 R-Hadron track opposite a neutral R-Hadron track does not contribute any miss-
 1987 ing energy in the calorimeters.

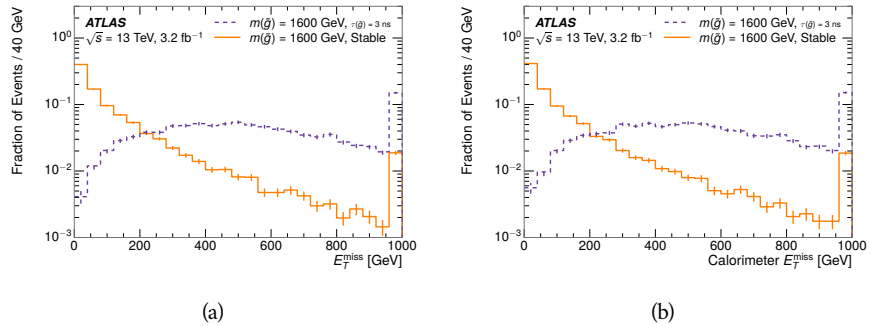


Figure 55: The distribution of (a) E_T^{miss} and (b) Calorimeter E_T^{miss} for simulated signal events before the trigger requirement.

1988 So, either case to some extent relies on kinematic degrees of freedom to pro-
 1989 duce missing energy, as the pair-produced LLPs tend to balance each other in
 1990 the transverse plain. That balance results in a relatively low efficiency for long-
 1991 lifetime particles, roughly 40%, and efficiencies between 65% and 95% for shorter
 1992 lifetimes depending on both the mass and the lifetime. For long lifetimes in par-
 1993 ticular, the presence of ISR is important in providing an imbalance in the trans-
 1994 verse plane, and is an important aspect of modeling the selection efficiency for
 1995 R-Hadron events.

1996 The missing energy trigger with the lowest threshold available is chosen for
 1997 this selection in order to maximize the trigger efficiency. During 2015 data col-
 1998 lection this was the HLT_xe70 trigger, which used a 50 GeV threshold on miss-
 1999 ing energy at LVL1 and a 70 GeV threshold on missing energy at the HLT. These
 2000 formation of the trigger decision for missing energy was discussed in more detail
 2001 in Section 6.6.

2002 11.2 KINEMATICS AND ISOLATION

2003 After the trigger requirement, each event is required to have a primary vertex
 2004 reconstructed from at least two well-measured tracks in the inner detector, each
 2005 with $p_T > 400$ MeV. If more than one such vertex exists, the primary vertex
 2006 is taken to be the one with the largest summed track momentum for all tracks
 2007 associated to that vertex. The offline reconstructed E_T^{miss} is required to be above
 2008 130 GeV to additionally reject SM backgrounds. The transverse missing energy
 2009 is calculated using fully reconstructed and calibrated offline objects, as described
 2010 in Section 7.5. In particular the E_T^{miss} definition in this selection uses jets recon-
 2011 structed with the anti- k_t algorithm with radius $R = 0.4$ from clusters of energy
 2012 in the calorimeter (Section 7.2) and with $p_T > 20$ GeV, as well as reconstructed
 2013 muons, electrons, and tracks not identified as another object type.

2014 The E_T^{miss} distributions are shown for data and a few simulated signals in Fig-
 2015 ure 56, after the trigger requirement. The cut placed at 130 GeV is 95% effi-
 2016 cient for metastable and 90% efficient for stable particles, after the trigger re-
 2017 quirement, because of the missing energy generating mechanisms discussed pre-
 2018 viously. The distribution of data in this figure and subsequent figures in this sec-
 2019 tion can be interpreted as the distribution of backgrounds, as any signal contam-
 2020 ination would be negligible if present at these early stages of the selection (prior
 2021 to the final requirement on ionization). The background falls rapidly with miss-
 2022 ing energy, motivating the direct requirement on E_T^{miss} for the signal region. Al-
 2023 though a tighter requirement than the specified value of 130 GeV would seem to
 2024 increase the search potential from these early distributions, other requirements
 2025 are more optimal when taken as a whole. The specific values for each require-
 2026 ment in signal region were optimized considering the increase in discovery reach
 2027 for tightening the requirement on each discriminating variable. **NOTE: If space**
 2028 **and time permit, I will add a whole section about signal region optimiza-**
 2029 **tion..**

2030 It is typically the practice for searches for new physics on ATLAS to place an
 2031 offline requirement on the triggering variable that is sufficiently tight to guar-

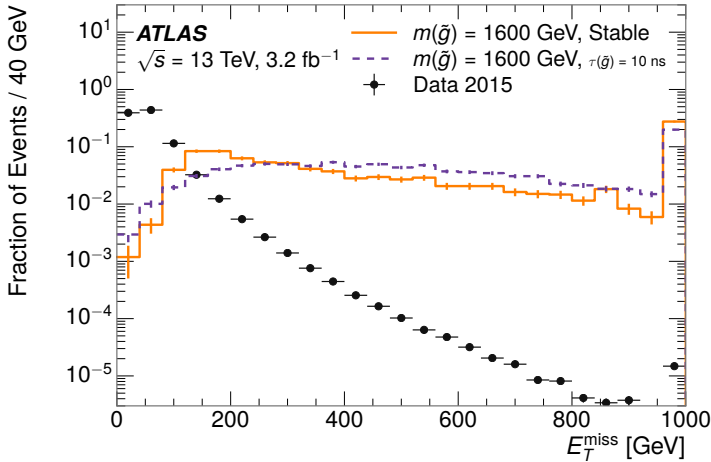


Figure 56: The distribution of E_T^{miss} for data and simulated signal events, after the trigger requirement.

2032 antee that the event would pass the trigger. Such a tight requirement makes the
 2033 uncertainty on the trigger efficiency of the simulation negligible, as modeling the
 2034 regime where the trigger is only partially efficient can be difficult. In this analy-
 2035 sis, however, because of the atypical interactions of R-Hadrons with the tracker
 2036 and the calorimeter, the offline requirement on E_T^{miss} is not sufficient to guar-
 2037 antee a 100% trigger efficiency even at large values, as can be seen in Figure 57.
 2038 This figure shows the efficiency for passing the HLT_xe70 trigger as a function
 2039 of the requirement on E_T^{miss} , which plateaus to roughly 85% even at large values.
 2040 This plateau does not reach 100% because events which have large offline miss-
 2041 ing energy from a neutral R-Hadron produced opposite of a charged R-Hadron
 2042 can have low missing energy in the calorimeters. The Calorimeter E_T^{miss} , on the
 2043 other hand, does not have this effect and reaches 100% efficiency at large values
 2044 because it is the quantity that directly corresponds to the trigger threshold. In
 2045 both cases the efficiency of triggering is greater for the short lifetime sample be-
 2046 cause the late decays to hadrons and LSPs produce an imbalance in the calorime-
 2047 ters even though they may not be reconstructed offline as tracks or jets. For this
 2048 reason, the requirement on E_T^{miss} is determined by optimizing the background
 2049 rejection even though it corresponds to a value of trigger efficiency significantly
 2050 below 1.0.

2051 Potential signal events are then required to have at least one candidate LLP
 2052 track. Although the LLPs are produced in pairs, many models do not consistently
 2053 yield two charged particles. For example, in the R-Hadron model highlighted
 2054 here, only 20% of events have two charged R-Hadrons while 47% of events have
 2055 just one. A signal region requiring two charged candidates could be a powerful
 2056 improvement in background rejection for a larger dataset, but it is not consid-
 2057 ered in this version of the analysis as it was found to be unnecessary to reject the
 2058 majority of backgrounds.

2059 For a track to be selected as a candidate, it must have $p_T > 50 \text{ GeV}$ and pass
 2060 basic quality requirements. The track must be associated to the primary vertex.

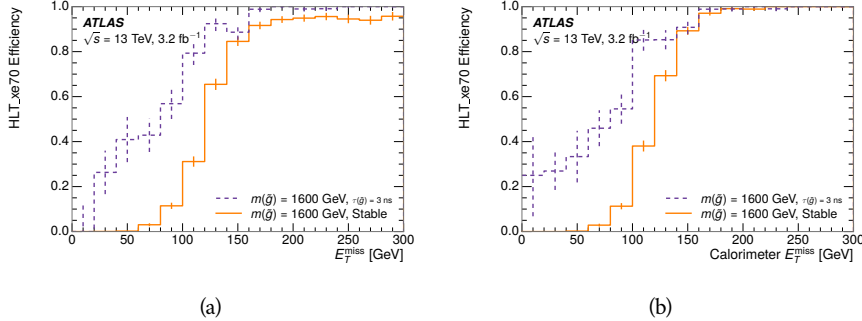


Figure 57: The trigger efficiency for the HLT_xe70 trigger requirement as a function of (a) E_T^{miss} and (b) Calorimeter E_T^{miss} for simulated signal events.

It must also have at least seven clusters in the silicon layers in the inner detector to ensure an accurate measurement of momentum. Those clusters must include one in the innermost layer if the extrapolated track is expected to pass through that layer. And to ensure a reliable measurement of ionization, the track is required to have at least two clusters in the pixel detector that provide a measurement of dE/dx .

At this point in the selection, there is a significant high-ionization background from multiple tracks that significantly overlap in the inner detector. Previous version of this analysis have rejected these overlaps by an explicit overlap rejection between pairs of fully reconstructed tracks, typically by requiring no additional tracks within a cone around the candidate. This technique, however, fails to remove the background from tracks that overlap so precisely that the tracks cannot be separately resolved, which can be produced in very collimated photon conversions or decays of pions.

A new method, added in Run 2, identifies cluster shapes that are likely formed by multiple particles based on a neural network classification algorithm. The number of clusters that are classified this way in the pixel detector for a given track is called N_{split} . As the shape of clusters requires significantly less spatial separation to identify overlaps than it does to reconstruct two fully resolved tracks, this variable is more effective at rejecting backgrounds from overlaps. Figure 58 shows the dependence of ionization on N_{split} ; as N_{split} increases the most probable value of dE/dx grows significantly up to twice the expected value when $N_{\text{split}} = 4$.

This requirement is very successful in reducing the long positive tail of the dE/dx distributions, as can be seen in Figure 59. Comparing the distribution for “baseline tracks”, tracks with only the above requirements on clusters applied and before the requirement on N_{split} , to the distribution with $N_{\text{split}} = 0$, it is clear that the fraction of tracks with large dE/dx is reduced be several orders of magnitude. The tracks without split hits are very close to the dE/dx distribution of identified muons, which are extremely well isolated on average. Figure 59 also includes the distribution of dE/dx in an example signal simulation to demonstrate how effective dE/dx is as a discriminating variable with this isolation applied. The background falls rapidly for $dE/dx > 1.8 \text{ MeVg}^{-1}\text{cm}^2$

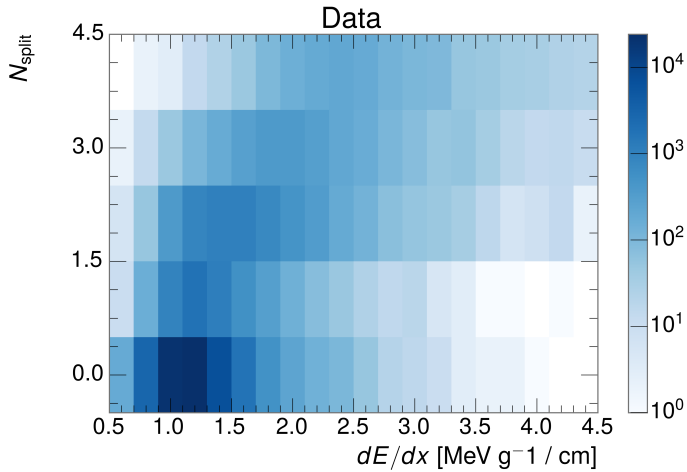


Figure 58: The dependence of dE/dx on N_{split} in data after basic track hit requirements have been applied.

2094 while the majority of the signal, approximately 90% depending on the mass, falls
 2095 above that threshold. Over 90% of [LLP](#) tracks in simulated signal events pass the
 2096 N_{split} -based isolation requirement.

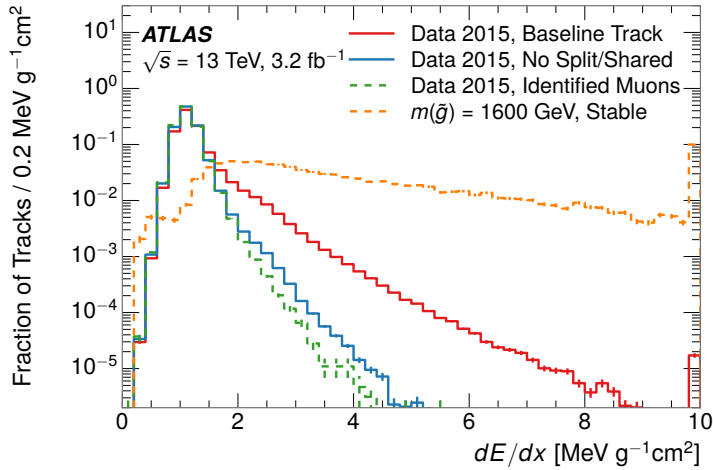


Figure 59: The distribution of dE/dx with various selections applied in data and simulated signal events.

2097 A few additional kinematic requirements are imposed to help reduce [SM](#) back-
 2098 grounds. The momentum of the candidate track must be at least 150 GeV, and
 2099 the uncertainty on that measurement must be less than 50%. The distribution of
 2100 momentum is shown in Figure 60 for tracks in data and simulated signal events
 2101 after the previously discussed requirements on clusters, transverse momentum,
 2102 and isolation have been imposed. The signal particles are much harder on aver-

age than their backgrounds because of the high energy interactions required to produce them. The transverse mass, M_T , defined as

$$M_T = \sqrt{2p_T E_T^{\text{miss}}(1 - \cos(\Delta\phi(E_T^{\text{miss}}, \text{track})))} \quad (6)$$

estimates the mass of a decay of to a single charged particle and an undetected particle and is required to be greater than 130 GeV to reject contributions from the decay of W bosons. Figure 61 shows the distribution of M_T for data and simulated signal events. The signal is distributed over a wide range of M_T , with about 90% above the threshold value of 130 GeV. The data shows a dual-peaked structure, where the first peak comes from W boson decays and the second peak is a kinematic shaping from the requirements on E_T^{miss} and the track p_T in dijet events.

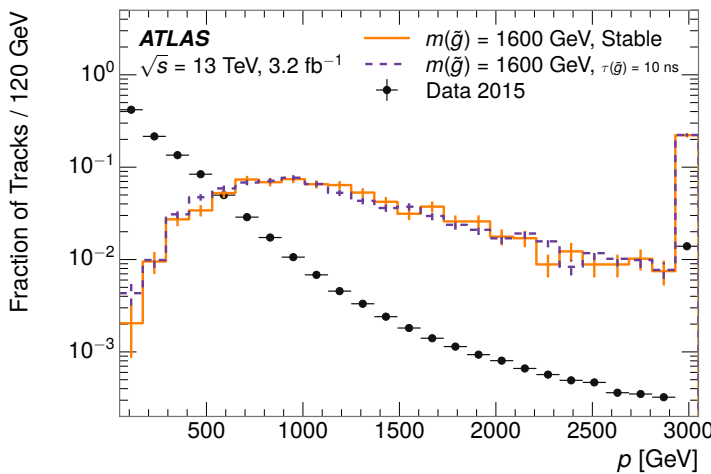


Figure 60: The distribution of track momentum for data and simulated signal events, after previous selection requirements have been applied.

11.3 PARTICLE SPECIES REJECTION

The amount of ionization deposited by particles with low mass and high momentum has a large positive tail [7], so backgrounds can be formed by a wide variety of SM processes when various charged particles have a few randomly large deposits of energy in the pixel detector. Those backgrounds can be additionally reduced by targeting other interactions with the detector where they are expected to have different behavior than R-Hadrons. The interactions with the detector depend on the types of particles produced rather than the processes which produce them, so this search forms a series of rejections to remove backgrounds from individual particle species. These rejections focus on using additional features of the event, other than the kinematics of the candidate track, as they can provide a powerful source of background rejection with very high signal efficiency. However, the lifetime of an R-Hadron can significantly change its

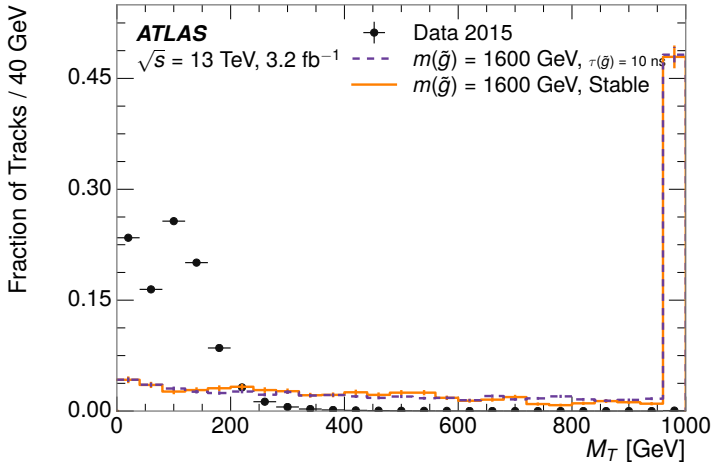


Figure 61: The distribution of M_T for data and simulated signal events, after previous selection requirements have been applied.

detector characteristics, as discussed in Section 10.1.2. To accommodate these differences, the SM rejections defined in this section are split to form two signal regions, one for long-lifetimes particles, the stable region ($50 \leq \tau[\text{ns}] < \infty \text{ ns}$), and one for intermediate lifetime particles, the metastable region ($0.4 < \tau[\text{ns}] < 50$).

Jets can be very effectively rejected by considering the larger-scale isolation of the candidate track. In this case the isolation focuses on the production of nearby particles as a jet-veto, rather than the isolation from overlapping tracks based on N_{split} that was used to reduce high-ionization backgrounds. As explained in Section 10.1, the fragmentation process which produces an R-Hadron is very hard and thus is not expected to produce additional particles with a summed momentum of more than 5 GeV. The jet-veto uses the summed momentum of tracks with a cone of $\Delta R < 0.25$, referred to as p_T^{Cone} , which is shown in Figure 62 for data and simulated signal events. In the data this value has a peak at zero from isolated tracks such as leptons, and a long tail from jets which contains as much as 80% of the background above 20 GeV at this stage of the selection. In signal events p_T^{Cone} is strongly peaked at zero and significantly less than 1% of signal events have p_T^{Cone} above 20 GeV. This makes a requirement of $p_T^{\text{Cone}} < 20 \text{ GeV}$ a very effective method to reject background without losing signal efficiency. For the stable signal region, this cut is further tightened to $p_T^{\text{Cone}} < 5 \text{ GeV}$ as it is the most effective variable remaining to extend the search reach for long lifetimes.

Even for fully isolated particles, there are additional methods to reject each type of particle using information in the muon system and calorimeters. Muons can be identified very reliably using the tracks in the muon system, as described in Section 7.4. For intermediate lifetimes the LLPs do not survive long enough to reach the muon system, and so muons are vetoed by rejecting tracks that associate to a muon with medium muon identification requirements (Section 7.4). For longer lifetimes, this rejection is not applied because LLPs which reach the

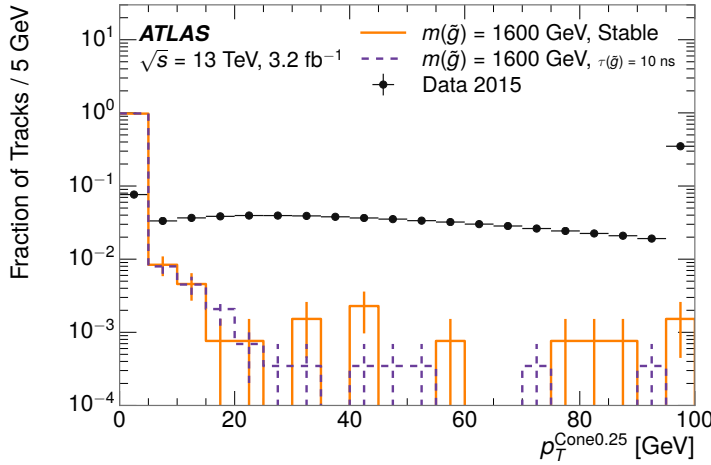


Figure 62: The distribution of summed tracked momentum within a cone of $\Delta R < 0.25$ around the candidate track for data and simulated signal events, after previous selection requirements have been applied.

muon system can be identified as muons as often as 30% of the time in simulated samples.

Calorimeter-based particle rejection relies on the expected small deposits of energy from LLPs. When the lifetime is long enough to reach the calorimeter, a LLP deposits little of its energy as it traverses the material, as discussed in Section 10.1. Even when the particle does decay before the calorimeter, the majority of its energy is carried away by the LSP and not deposited in the calorimeter. In both cases the energy is expected to be distributed across the layers of the calorimeters and not peaked in just one layer. This can be quantified in terms of E/p , the ratio of calorimeter energy of a nearby jet to the track momentum, and f_{EM} , the fraction of energy in that jet within the electromagnetic calorimeter. When no jets fall within a cone of 0.05 of the particle, E/p and f_{EM} are both defined as zero. E/p is expected to be above 1.0 for typical SM particles because of calibration and the contributions from other nearby particles, as discussed in Chapter ???. At these momenta there is no significant zero fraction due to interactions with the detector or insufficient energy deposits (see Section 8.2.2). f_{EM} is peaked close to 1.0 for electrons, and distributed between 10% and 90% for hadrons.

These trends can be seen in the two dimensional distribution for signal in Figure 63 for stable and metastable (10 ns) events. The majority of R-Hadrons in both samples fall into the bin for $E/p = 0$ and $f_{\text{EM}} = 0$ because the majority of the time there is no associated jet. In the stable sample, when there often is an associated jet, E/p is typically still below 0.1, and the f_{EM} is predominantly under 0.8. In the metastable sample, on the other hand, E/p is larger but still typically below 0.1 because of actual jets produced during the decay. The f_{EM} is much lower on average in this case, below 0.1, because the 10 ns lifetime particles rarely decay before passing through the electromagnetic calorimeter. Figure 63 also includes simulated Z decays to electrons or tau leptons. From the decays

2183 to electrons it is clear that the majority of electrons have f_{EM} above 0.9. The
 2184 tau decays include a variety of products. Muons can be seen in the bin where
 2185 $E/p = 0$ and $f_{\text{EM}} = 0$ because they do not have an associated jet. Electrons fall
 2186 into the range where $E/p > 1$ and $f_{\text{EM}} > 0.9$. Hadronic tau decays are the most
 2187 common, and fall in the range of $0.1 < f_{\text{EM}} < 0.9$ and $E/p > 1.0$.

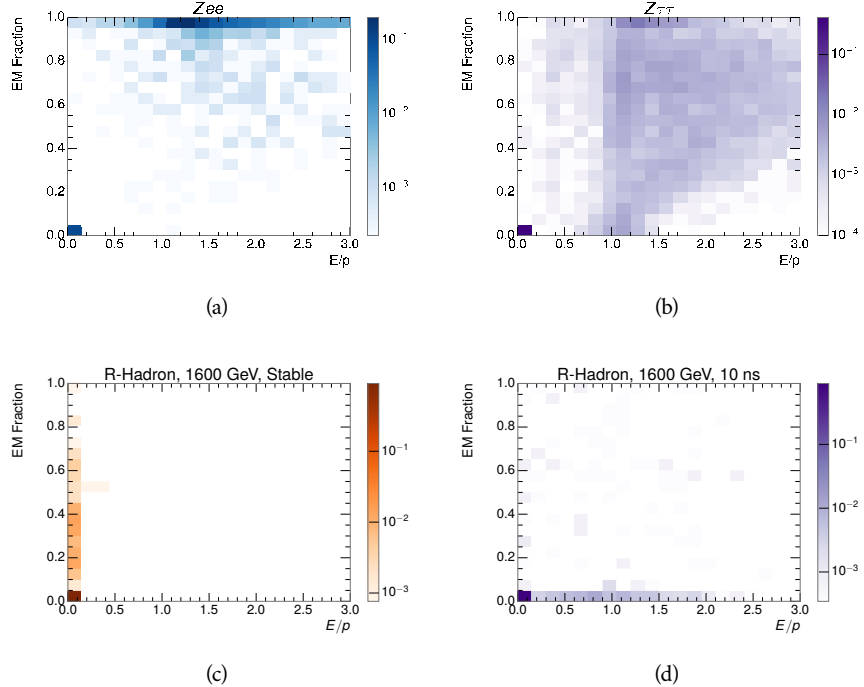


Figure 63: The normalized, two-dimensional distribution of E/p and f_{EM} for simulated
 (a) $Z \rightarrow ee$, (b) $Z \rightarrow \tau\tau$, (c) 1200 GeV Stable R-Hadron events, and (d) 1200
 GeV, 10 ns R-Hadron events.

2188 These differences motivate an electron rejection by requiring an f_{EM} below
 2189 0.9. Similarly, isolated hadrons are rejected by requiring $E/p < 1.0$. These re-
 2190 quirements combine to remove the majority of isolated electrons and hadrons
 2191 but retain over 95% of the simulated signal across a range of masses and lifetimes.

2192 11.4 IONIZATION

2193 The final requirement on the candidate track is the primary discriminating vari-
 2194 able, the ionization in the pixel detector. That ionization is measured in terms
 2195 of dE/dx , which was shown for data and simulated signal events in Figure 59.
 2196 dE/dx is dramatically greater for the high mass signal particles than the back-
 2197 grounds, which start to fall immediately after the minimally ionizing peak at 1.1
 2198 $\text{MeV g}^{-1} \text{cm}^2$. The dE/dx for candidate tracks must be greater than a pseudorapidity-
 2199 dependent threshold, specifically $1.80 - 0.11|\eta| + 0.17\eta^2 - 0.05\eta^3 \text{ MeV g}^{-1} \text{ cm}^{-2}$,
 2200 in order to correct for an approximately 5% dependence of the MIP peak on η .
 2201 The requirement was chosen as part of the signal region optimization, and man-

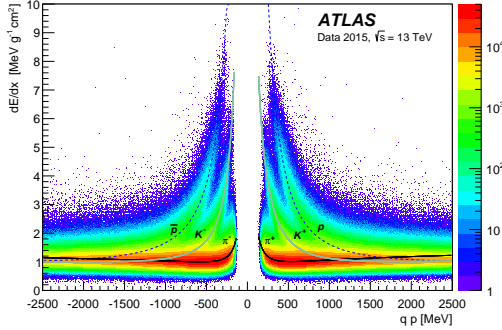


Figure 64: Two-dimensional distribution of dE/dx versus charge signed momentum (qp) for minimum-bias tracks. The fitted distributions of the most probable values for pions, kaons and protons are superimposed.

ages to reduce the backgrounds by a factor of 100 while remaining 70-90% efficient for simulated signal events depending on the mass.

11.4.1 MASS ESTIMATION

The mean value of ionization in silicon is governed by the Bethe equation and the most probable value follows a Landau-Vavilov distribution [7]. Those forms inspire a parametric description of dE/dx in terms of $\beta\gamma$,

$$(dE/dx)_{MPV}(\beta\gamma) = \frac{p_1}{\beta^{p_3}} \ln(1 + [p_2 \beta\gamma]^{p_5}) - p_4 \quad (7)$$

which performs well in the range $0.3 < \beta\gamma < 1.5$. This range includes the expected range of $\beta\gamma$ for the particles targeted for this search, with $\beta\gamma \approx 2.0$ for lower mass particles ($O(100 \text{ GeV})$) and up to $\beta\gamma \approx 0.5$ for higher mass particles ($O(1000 \text{ GeV})$). The parameters, p_i , are fit using a 2015 data sample of low-momentum pions, kaons, and protons as described in Ref. [78]. Figure 64 shows the two-dimensional distribution of dE/dx and momentum along with the above fitted values for $(dE/dx)_{MPV}$.

The above equation (7) is then numerically inverted to estimate $\beta\gamma$ and the mass for each candidate track. In simulated signal events, the mean of this mass value reproduces the generated mass up to around 1800 GeV to within 3%, and 3% shift is applied to correct for this difference. The mass distributions prior to this correction are shown for a few stable mass points in Figure 65. The large widths of these distributions come from the high variability in energy deposits in the pixel detector as well as the uncertainty on momentum measurements at high momentum, but the means converge to the expected values.

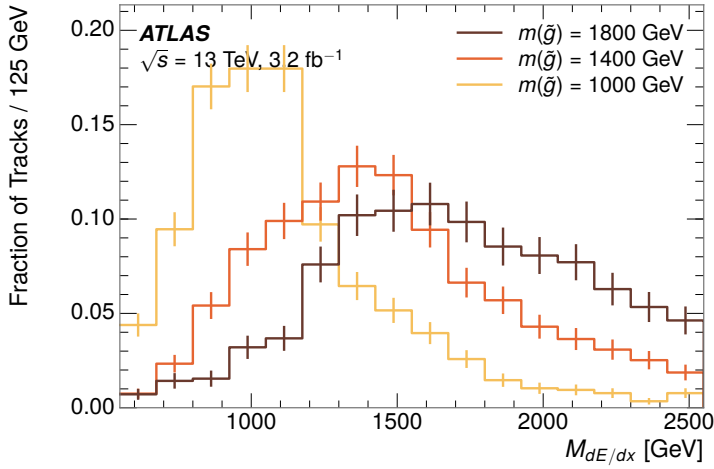


Figure 65: The distribution of mass estimated using dE/dx for simulated stable R-Hadrons with masses between 1000 and 1600 GeV.

This analysis evaluates expected yields and the resulting cross sectional limits using windows in this mass variable. The windows are formed by fitting mass distributions in simulated signal events like those in Figure 65 to Gaussian distributions and taking all events that fall within $\pm 1.4\sigma$ of the mean. As can be seen in Figure 65, typical values for this width are $\sigma \approx 300 - 500$ GeV depending on the generated mass.

11.5 EFFICIENCY

The numbers of events passing each requirement through ionization are shown in Table 6 for the full 2015 dataset and a simulated 1600 GeV, 10 ns lifetime R-Hadron sample. The table highlights the overall acceptance \times efficiency for signal events, which for this example is 19%. Between SM rejection and ionization, this signal region reduces the background of tracks which pass the kinematic requirements down by an additional factor of almost 2000.

There is a strong dependence of this efficiency on lifetime and mass, with efficiencies dropping to under 1% at low lifetimes. Figure 66 shows the dependence on both mass and lifetime for all signal samples considered in this search. The dependence on mass is relatively slight and comes predominantly from the increasing fraction of R-Hadrons which pass the ionization cut with increasing mass. The trigger and E_T^{miss} requirements are most efficient for particles that decay before reaching the calorimeters. However, the chance of a particle to be reconstructed as a high-quality track decreases significantly at low lifetimes as the particle does not propagate sufficiently through the inner detector. These effects lead to a maximum in the selection efficiency for lifetimes around 10-30 ns.

The inefficiency of this signal region at short lifetimes comes almost exclusively from an acceptance effect, in that the particles do not reach the necessary

Selection	Exp. Signal Events	Observed Events in 3.2 fb^{-1}
Generated	26.0 ± 0.3	
E_T^{miss} Trigger	24.8 ± 0.3 (95%)	
$E_T^{\text{miss}} > 130 \text{ GeV}$	23.9 ± 0.3 (92%)	
Track Quality and $p_T > 50$	10.7 ± 0.2 (41%)	368324
Isolation Requirement	9.0 ± 0.2 (35%)	108079
Track $p > 150 \text{ GeV}$	6.6 ± 0.2 (25%)	47463
$M_T > 130 \text{ GeV}$	5.8 ± 0.2 (22%)	18746
Electron and Hadron Veto	5.5 ± 0.2 (21%)	3612
Muon Veto	5.5 ± 0.2 (21%)	1668
Ionization Requirement	5.0 ± 0.1 (19%)	11

Table 6: The expected number of events at each level of the selection for metastable $1600 \text{ GeV}, 10 \text{ ns}$ R-Hadrons, along with the number of events observed in data, for 3.2 fb^{-1} . The simulated yields are shown with statistical uncertainties only. The total efficiency \times acceptance is also shown for the signal.

2249 layers of the SCT. This can be seen more clearly by defining a fiducial region
 2250 which includes events with at least one R-Hadron that is produced with non-
 2251 zero charge, $p_T > 50 \text{ GeV}$, $p > 150 \text{ GeV}$, $|\eta| < 2.5$, and a decay distance greater
 2252 than 37 cm in the transverse plane. At short (1 ns) lifetimes, the acceptance into
 2253 this region is as low as 4%. Once this acceptance is accounted for, the selection
 2254 efficiency ranges from 25% at lifetimes of 1 ns up to 45% at lifetimes of 10 ns.

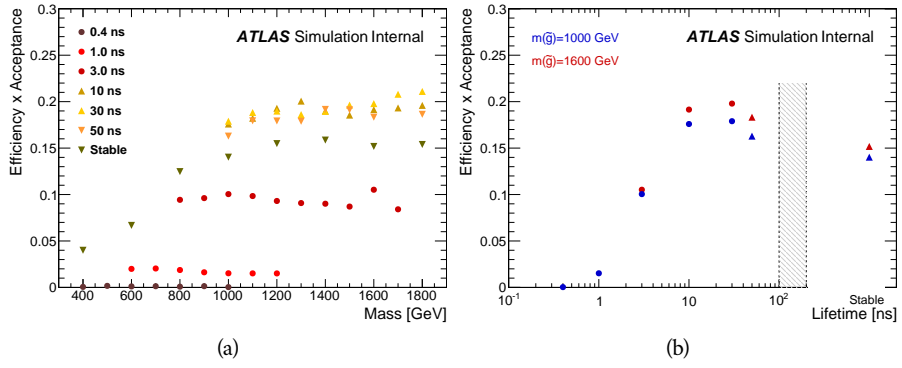


Figure 66: The acceptance \times efficiency as a function of R-Hadron (a) mass and (b) lifetime. (a) shows all of the combinations of mass and lifetime considered in this search, and (b) highlights the lifetime dependence for 1000 GeV and 1600 GeV R-Hadrons.

2255

2256 BACKGROUND ESTIMATION

2257 The event selection discussed in the previous section focuses on detector signatures,
 2258 emphasizing a single high-momentum, highly-ionizing track. That track
 2259 is then required to be in some way inconsistent with the expected properties
 2260 of SM particles, with various requirements designed to reject jets, hadrons,
 2261 electrons, and muons (Section 11.3). Therefore the background for this search comes
 2262 entirely from reducible backgrounds that are outliers of various distributions in-
 2263 cluding dE/dx , f_{EM} , and p_T^{Cone} . The simulation can be tuned in various ways to
 2264 do an excellent job of modeling the average properties of each particle type [79],
 2265 but it is not necessarily expected to accurately reproduce outliers. For this rea-
 2266 sons, the background estimation used for this search is estimated entirely using
 2267 data.

2268 12.1 BACKGROUND SOURCES

2269 SM charged particles with lifetimes long enough to form tracks in the inner de-
 2270 tector can be grouped into three major categories based on their detector inter-
 2271 actions: hadrons, electrons, and muons. Every particle that enters into the back-
 2272 ground for this search belongs to one of these types. Relatively pure samples of
 2273 tracks from each of these types can be formed in data by inverting the various
 2274 rejection techniques in Section 11.3. Specifically, muons are selected requiring
 2275 medium muon identification, electrons requiring $E/p > 1.0$ and $f_{EM} > 0.95$,
 2276 and hadrons requiring $E/p > 1.0$ and $f_{EM} < 0.95$.

2277 Figure 67 shows the distributions of momentum and dE/dx for these cate-
 2278 gories in data, after requiring the event level selection as well as the track re-
 2279 quirements on p_T , hits, and N_{split} , as discussed in Section 11.2. Simulated signal
 2280 events are included for reference. These distribution are only illustrative of the
 2281 differences between types, as the rejection requirements could alter their shape.
 2282 This is especially significant for momentum which enters directly into E/p and
 2283 can indirectly affect muon identification. However the various types show clear
 2284 differences in both distributions. The distributions of momentum are not nec-
 2285 cessarily expected to match between the various types because the production
 2286 mechanisms for each type result in different kinematic distributions. dE/dx is
 2287 also different between types because of incomplete isolation; although the re-
 2288 quirement on N_{split} helps to reduce the contribution of nearby particles it does
 2289 not completely remove the effect of overlaps. Muons are better isolated because
 2290 they do not have the additional particle from hadronization present for hadrons
 2291 and they are significantly less likely do interact with the detector and produce
 2292 secondary particles compared to hadrons and electrons. Thus muons have the
 2293 smallest fraction of dE/dx above the threshold of $1.8 \text{ MeVg}^{-1}\text{cm}^2$; hadrons and
 2294 electrons have a larger fraction above this threshold.

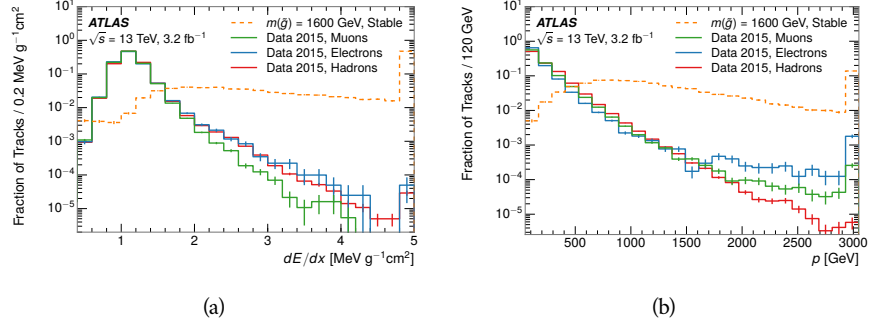


Figure 67: The distribution of (a) dE/dx and (b) momentum for tracks in data and simulated signal after requiring the event level selection and the track selection on p_T , hits, and N_{split} . Each sub-figure shows the normalized distributions for tracks classified as hadrons, electrons, and muons in data and R-Hadrons in the simulated signal.

2295 It is difficult to determine what fraction of each particle type enters into the fi-
 2296 nal signal region. The background method will not have significant dependence
 2297 on the relative contributions of each species, but it is useful to understand the
 2298 differences between each when considering the various tests of the method.

2299 12.2 PREDICTION METHOD

2300 The data-driven background estimation relies on the independence between ion-
 2301 ization and other kinematic variables in the event. For standard model particles
 2302 with momenta above 50 GeV, dE/dx is not correlated with momentum; though
 2303 there is a slight relativistic rise as momentum increases, the effect is small com-
 2304 pared to the width of the distribution of ionization energy deposits.. So, the
 2305 proposed method to estimate the mass distribution of the signal region is to use
 2306 momentum from a track with low dE/dx (below the threshold value) and to com-
 2307 bine it with a random dE/dx value from a dE/dx template. The resulting track is
 2308 just as likely as the original, so a number of such random generations provide the
 2309 expected distributions of momentum and ionization. These are then combined
 2310 using the parametrization described in Section 11.4.1 to form a distribution of
 2311 mass for the signal region.

2312 Algorithmically this method is implemented by forming two distinct Control
 2313 Regions (**CR**s). The first **CR**, CR1, is formed by applying the entire event selec-
 2314 tion from Chapter 11 up to the dE/dx and mass requirements. The dE/dx re-
 2315 quirement is instead inverted for this region. Because of the independence of
 2316 dE/dx , the tracks in this control region have the same kinematic distribution
 2317 as the tracks in the signal region, and are used to measure a two-dimensional
 2318 template of p and η . The second **CR**, CR2, is formed from the event selection
 2319 through the dE/dx requirement, but with an inverted E_T^{miss} requirement. The
 2320 tracks in this control region are expected to have similar dE/dx distributions to
 2321 the signal region before the ionization requirement, and so this region is used to
 2322 measure a two-dimensional template of dE/dx and η .

2323 The contribution of any signal to the control regions is minimized by the in-
 2324 verted selection requirements. Only less than 10% of simulated signal events
 2325 have either dE/dx or E_T^{miss} below the threshold values in the original signal re-
 2326 gion, while the backgrounds are significantly enhanced by inverting those re-
 2327 quirements. The signal contamination is less than 1% in both control regions
 2328 for all of the simulated masses and lifetimes considered in this analysis.

2329 With those measured templates, the shape of the mass estimation is generated
 2330 by first selecting a random (p, η) combination from CR1. This momentum
 2331 value is combined with a dE/dx value taken from the appropriate distribution
 2332 of dE/dx for the selected η from CR2. The use of η in both random samplings
 2333 controls for any correlation between p , dE/dx , and η . Those values are then
 2334 used to calculate a mass in the same way that is done for regular tracks in data,
 2335 see Section 11.4.1. As this procedure includes all dE/dx values, the cut at 1.8
 2336 MeVg $^{-1}$ cm 2 is then enforced to fully model the signal region. The generated
 2337 mass distribution is then normalized by scaling the background estimate to the
 2338 data in the region $M < 160$ GeV, where signals of this type have already been
 2339 excluded [63]. This normalization uses the distributions of mass generated with-
 2340 out the ionization requirement.

2341 The statistical uncertainties on these background distributions are calculated
 2342 by independently fluctuating each bin of the input templates according to their
 2343 Poisson uncertainties. These fluctuations are repeated a large number of times,
 2344 and the uncertainty on the resulting distribution is taken as the root mean square
 2345 (RMS) deviation of the fluctuations from the average. As the procedure uses one
 2346 million random combinations to generate the distributions, The statistical un-
 2347 certainty from the actual random generations is negligible compared to the un-
 2348 certainty from measuring the templates.

2349 12.3 VALIDATION

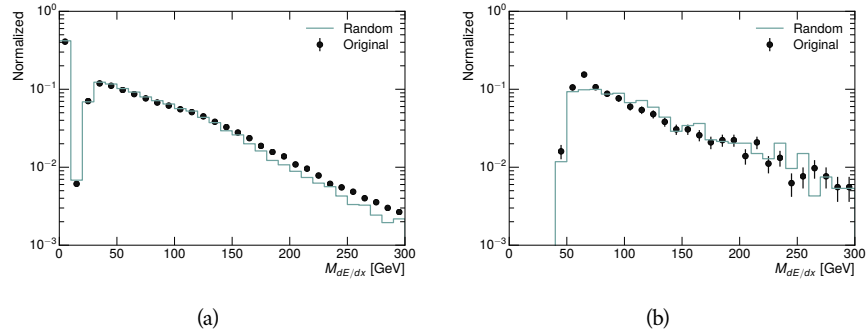
2350 The validity of the background estimation technique can be evaluated in both
 2351 data and simulation. The underlying assumption that random combinations of
 2352 dE/dx and momentum can predict a mass distribution in an orthogonal region
 2353 can be tested using simulated samples where concerns like multiple particle types
 2354 can be controlled. Using the same technique in another set of signal-depleted
 2355 regions in data then extends this confidence to the more complicated case where
 2356 several particle species are inherently included.

2357 12.3.1 CLOSURE IN SIMULATION

2358 The first test of the procedure is done using a simulated sample of $W \rightarrow \mu\nu$
 2359 decays. These types of events provide the ingredients required to test the back-
 2360 ground estimate, E_T^{miss} and isolated tracks, with high statistics. In this example
 2361 there is no signal, so simulated events in the orthogonal CRs are used to estimate
 2362 the shape of the mass distribution of the simulated events in the signal region. To
 2363 reflect the different topology for W boson decays, the CRs use slightly modified
 2364 definitions. In all CRs, the requirement of $p > 150$ GeV and the SM rejection

2365 requirements are removed. Additionally, for the signal region the requirement
 2366 on E_T^{miss} is relaxed to 30 GeV and the corresponding inverted requirement on
 2367 CR2 is also set at 30 GeV.

2368 With these modified selections, the simulated and randomly generated distri-
 2369 butions of $M_{dE/dx}$ are shown in Figure 68. This figure includes the mass distri-
 2370 butions before and after the requirement on dE/dx , which significantly shapes
 2371 the distributions. In both cases the background estimation technique repro-
 2372 duces the shape of $M_{dE/dx}$ in the signal region. There is a small difference in the pos-
 2373 itive tail of the mass distribution prior to the ionization cut, where the random
 2374 events underestimate the fraction of tracks with mass above 150 GeV by about
 2375 20%. After the ionization requirement, however, this discrepancy is not present
 2376 and the two distributions agree to within statistical uncertainties.



2377 Figure 68: The distribution of $M_{dE/dx}$ (a) before and (b) after the ionization requirement
 2378 for tracks in simulated W boson decays and for the randomly generated back-
 2379 ground estimate.

2380 This ability to reproduce the shape of the mass distribution in simulated events
 2381 shows that the technique works as expected. No significant biases are acquired
 2382 in using low dE/dx events to select kinematic templates or in using low E_T^{miss}
 2383 events to select ionization templates, as either would result in a mismodeling of
 2384 the shape of the mass distribution. The simulated events contain only one par-
 2385 ticle type, however, so this test only establishes that the technique works well
 2386 when the the CRs are populated by exactly the same species.

2387 12.3.2 VALIDATION REGION IN DATA

2388 The second test of the background estimate is performed using data in an or-
 2389 thogonal validation region. The validation region, and the corresponding CRs,
 2390 are formed using the same selection requirements as in the nominal method but
 2391 with a modified requirement on momentum, $50 < p[\text{GeV}] < 150$. This allows
 2392 the technique to be checked in a region with very similar properties but where
 2393 the signal is depleted, as the majority of the signal has momentum above 150
 2394 GeV while the backgrounds are enhanced below that threshold. Any biases on
 2395 the particle composition of the CRs for the signal region will be reflected in the
 2396 CRs used to estimate the mass distribution in the validation region.

2394 Figure 69 shows the measured and randomly generated mass distributions for
 2395 data before and after the ionization requirement. The background estimate does
 2396 an excellent job of modeling the actual background before the ionization require-
 2397 ment, with good agreement to within the statistical uncertainties out to the limit
 2398 of the mass distribution. There are very few events in the validation region after
 2399 the ionization requirement, but the few observed events are consistent with the
 2400 background prediction. The good agreement in this validation region provides
 2401 a confirmation that the technique works even in the full-complexity case with
 2402 multiple particle types entering the distributions. Any bias from changes in par-
 2403 ticle composition between regions is small compared to statistical uncertainties.

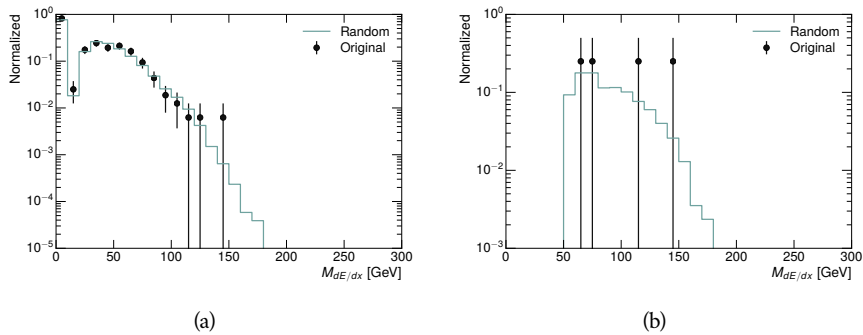


Figure 69: The distribution of $M_{dE/dx}$ (a) before and (b) after the ionization require-
 ment for tracks in the validation region and for the randomly generated back-
 ground estimate.

2404

2405 SYSTEMATIC UNCERTAINTIES AND RESULTS

2406 13.1 SYSTEMATIC UNCERTAINTIES

2407 A number of systematic uncertainties affect the interpretation of the results of
 2408 the search. These uncertainties can broken down into two major categories,
 2409 those which affect the estimate of the background using data and those which
 2410 affect the measurement of the signal yield estimated with simulated events. The
 2411 total measured systematic uncertainties are 7% for the background estimation
 2412 and approximately 32% for the signal yield depending on lifetime. These system-
 2413atic uncertainties are expected to be small compared to the statistical fluctuations
 2414 of the measured yields so that measured cross-sectional limits will be dominated
 2415 by statistical uncertainties. The following sections describe each source of sys-
 2416 tematic uncertainty for each of the two types.

2417 13.1.1 BACKGROUND ESTIMATE

2418 The systematic uncertainties on the background estimate come primarily from
 2419 considering alternative methods for generating the background distributions.
 2420 These uncertainties are small compared to the statistical uncertainties on the
 2421 background estimate which come from the limited statistics in measuring the
 2422 template distributions, as described in Section 12.2. They are summarized in
 2423 Table 7.

Source of Uncertainty:	Value [%]
Analytic Description of dE/dx	4.0
Muon Fraction (Stable Region only)	3.0
IBL Ionization Correction	3.8
Normalization	3.0
Total (Metastable Region):	6.3
Total (Stable Region):	7.0

Table 7: A summary of the sources of systematic uncertainty for the data-driven back-
 ground in the signal region. If the uncertainty depends on the mass, the maxi-
 mum values are reported.

2424 13.1.1.1 ANALYTIC DESCRIPTION OF DE/DX

2425 The background estimate uses a binned template distribution to estimate the
 2426 dE/dx of tracks in the signal region, as described in Section 12.2. It is also possi-

ble to fit that measured distribution to a functional form to help smooth the distribution in the tails of dE/dx where the template is driven by a small number of tracks. Both Landau convolved with a Gaussian and Crystal Ball functions are considered as the functional form and used to re-estimate the background distribution. The deviations compared to the nominal method are found to be 4%, and this is taken as a systematic uncertainty to cover the inability carefully predict the contribution from the long tail of dE/dx where there are few measurements available in data.

2435 13.1.1.2 MUON FRACTION

2436 The stable region of the analysis explicitly includes tracks identified as muons,
 2437 which have a known difference in their dE/dx distributions compared to non-
 2438 muon tracks (Section 12.1). To account for a difference in muon fraction be-
 2439 tween the background region and the signal region for this selection, the dE/dx
 2440 templates for muons and non-muons are measured separately and then the rel-
 2441 ative fraction of each is varied in the random generation. The muon fraction
 2442 is varied by its statistical uncertainty and the resulting difference of 3% in back-
 2443 ground yield is taken as the systematic uncertainty.

2444 13.1.1.3 IBL CORRECTIONS

2445 The IBL, described in Section 6.3.1, received a significant dose of radiation during
 2446 the data collection in 2015. The irradiation can cause a drift in the frontend
 2447 electronics and thus alter the dE/dx measurement which includes the ToT output
 2448 by the IBL. These effects are corrected for in the nominal analysis by scaling the
 2449 dE/dx measurements by a constant factor derived for each run to match the
 2450 average dE/dx value to a reference run where the IBL was known to be stable
 2451 to this effect. However, this corrective factor does not account for inter-run
 2452 variations. To account for this potential drift of dE/dx , the correction procedure
 2453 is repeated by varying the corrections up and down by the maximal run-to-run
 2454 variation from the full data-taking period, which results in an uncertainty of
 2455 3.8%.

2456 13.1.1.4 NORMALIZATION

2457 As described in Section 12.2, the generated distribution of masses is normalized
 2458 in a shoulder region ($M < 160$ GeV) where signals have been excluded by pre-
 2459 vious analyses. That normalization factor is varied by its statistical uncertainty
 2460 and the resulting fluctuation in the mass distribution of 3% is taken as a system-
 2461 atic uncertainty on the background estimate.

2462 13.1.2 SIGNAL YIELD

2463 The systematic uncertainties on the signal yield can be divided into three cate-
 2464 gories; those on the simulation process, those on the modeling of the detector
 2465 efficiency or calibration, and those affecting the overall signal yield. They are
 2466 summarized in Table 7. The largest uncertainty comes from the uncertainty on

2467 the production cross section for gluinos, which is the dominant systematic un-
 2468 certainty in this analysis.

Source of Uncertainty	-[%]	+[%]
ISR Modeling (Metastable Region)	1.5	1.5
ISR Modeling (Stable Region)	14	14
Pile-up Reweighting	1.1	1.1
Trigger Efficiency Reweighting	0.9	0.9
E_T^{miss} Scale	1.1	2.2
Ionization Parametrization	7.1	0
Momentum Parametrization	0.3	0.0
Electron Rejection	0.0	0.0
Hadron Rejection	0.0	0.0
μ Identification	4.3	4.3
Luminosity	5	5
Signal size uncertainty	28	28
Total (Metastable Region)	30	29
Total (Stable Region)	33	32

Table 8: A summary of the sources of systematic uncertainty for the simulated signal yield. The uncertainty depends on the mass and lifetime, and the maximum negative and positive values are reported in the table.

2469 13.1.2.1 ISR MODELING

2470 As discussed in Section 10.2, MadGraph is expected to reproduce the distribution
 2471 of ISR in signal events more accurately than the nominal Pythia samples. The
 2472 analysis reweights the distribution of ISR in the simulated signal events to match
 2473 the distribution found in generated MadGraph samples. This has an effect on the
 2474 selection efficiency in the signal samples, where ISR contributes to the generation
 2475 of E_T^{miss} . To account for the potential inaccuracy on the simulation of ISR at high
 2476 energies, half of the difference between the signal efficiency with the reweighted
 2477 distribution and the original distribution is taken as a systematic uncertainty.

2478 13.1.2.2 PILEUP REWEIGHTING

2479 The simulated events were generated prior to data collection with an estimate of
 2480 the average number of interactions per bunch crossing. This estimate does not
 2481 match the value of pileup during actual data collection, but a large fraction of the
 2482 simulated events would be discarded in order to match the distribution in data.
 2483 Therefore the simulated signal events are not reweighted for pileup by default
 2484 in the analysis. The effect of the pileup on signal efficiency is not expected to
 2485 depend on the mass or lifetime of the generated signal events, which allows all

2486 of the generated signal events to be used together to assess the pileup dependence.
 2487 To account for the potential effect of the difference in the number of interactions
 2488 per bunch crossing between data and simulation, the difference in yield between
 2489 the nominal signal events and the reweighted events averaged over all masses
 2490 and lifetimes is taken as a systematic uncertainty on the yield for each mass and
 2491 lifetime (1.1%).

2492 13.1.2.3 TRIGGER EFFICIENCY REWEIGHTING

2493 As described in Section 11.2, the selection for this analysis does not require a suf-
 2494 ficiently large value of E_T^{miss} to be above the plateau of trigger efficiency. There-
 2495 fore, some signal events which would otherwise pass the event selection can be
 2496 excluded because of the trigger requirement. These effects can be difficult to es-
 2497 timate in simulation, and thus are constrained by comparing data and simulated
 2498 events in an alternative W boson region which uses decays to muons to find a rel-
 2499 atively pure sample of events with missing energy. The trigger efficiency for data
 2500 and simulated W events are shown in Figure 70. The comparison between data
 2501 and MC in this region constrains the simulation of the trigger efficiency. The
 2502 simulated signal events are reweighted by the ratio of data to simulation in the
 2503 W boson decays, while the difference between the data and simulation in those
 2504 decays is taken as a systematic uncertainty. This results in an uncertainty of only
 2505 0.9% as the majority of events are well above the plateau and the disagreement
 2506 between data and simulation is small even below that plateau.

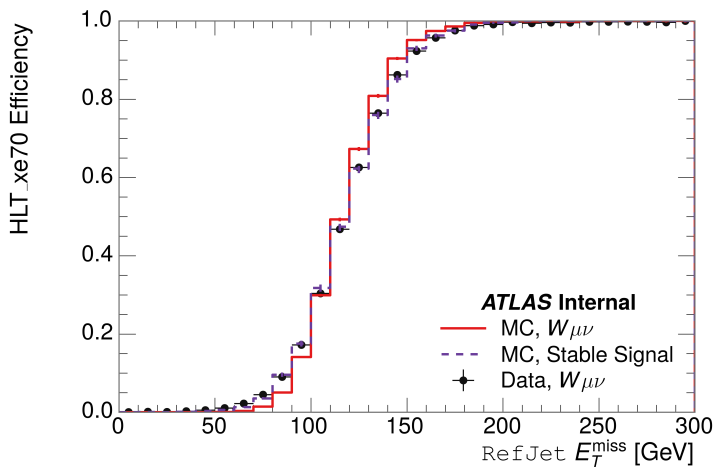


Figure 70: The trigger efficiency for the HLT_xe70 trigger requirement as a function of Calorimeter E_T^{miss} for simulated data events with a W boson selection. Simulated signal events and simulated W boson events are also included.

2507 13.1.2.4 MISSING TRANSVERSE MOMENTUM SCALE

2508 The ATLAS Combined Performance (CP) group provides a default recommenda-
 2509 tion for systematic variations of jets and missing energy (**note: I'm not quite**
 2510 **sure what to cite for this - I don't see any papers from the jet/met group**

Systematic Variation	-[%]	+[%]
JET_GroupedNP_1	-0.7	1.3
JET_GroupedNP_2	-0.7	1.2
JET_GroupedNP_3	-0.5	1.3

Table 9: Example of the contributing systematic variations to the total systematic for the E_T^{miss} Scale, as measured in a 1200 GeV, Stable R-Hadron signal sample.

2511 **after this was implemented).** These variations enter into this analysis only in
 2512 the requirement on E_T^{miss} . The effect of the measured scale of E_T^{miss} is evaluated
 2513 by varying the E_T^{miss} scale according to the one sigma variations provided by all
 2514 **CP** recommendations on objects affecting event kinematics in simulated signal
 2515 events. Missing energy is reconstructed from fully reconstructed objects so any
 2516 systematic uncertainties affecting jets, muons, electrons, or the E_T^{miss} soft terms
 2517 are included. The only non-negligible contributions found using this method are
 2518 itemized in Table 9 for an example signal sample (1200 GeV, Stable R-Hadron),
 2519 where the systematic is measured as the relative difference in the final signal ef-
 2520 ficiency after applying the associated variation through the CP tools. The only
 2521 variations that are significant are the grouped jet systematic variations, which
 2522 combine recommended jet systematic uncertainties into linearly independent
 2523 variations.

2524 As the peak of the reconstructed E_T^{miss} distribution in the signal is significantly
 2525 above the current threshold for events which pass the trigger requirement, the
 2526 effect of scale variation is expected to be small, which is consistent with the mea-
 2527 sured systematic of approximately 2%. Events which do not pass the trigger re-
 2528 quirement usually fail because there are no ISR jets in the event to balance the
 2529 R -hadrons' transverse momentum, so the reconstructed E_T^{miss} is low and there-
 2530 fore also expected to be not very sensitive to scale changes.

2531 13.1.2.5 MOMENTUM PARAMETRIZATION

2532 The uncertainty on the signal efficiency from track momentum is calculated us-
 2533 ing the **CP** group recommendations for tracks. In particular, only one recom-
 2534 mended systematic variation affects track momentum, the sagitta bias for q/P .
 2535 This uncertainty is propagated to the final selection efficiency by varying the
 2536 track momentum by the recommended one sigma variation, and the associated
 2537 uncertainty is found to be negligible (0.3%).

2538 13.1.2.6 IONIZATION REQUIREMENT

2539 The dE/dx distributions in data and simulated events have different most prob-
 2540 able values, which is due in part to radiation effects in the detector that are not
 2541 fully accounted for in the simulation. The difference does not affect the mass
 2542 measurement used in this analysis, as independent calibrations are done in sim-
 2543 ulation and in data. However, it does affect the efficiency of the high dE/dx
 2544 selection requirement. To calculate the size of the effect on the signal efficiency,

2545 the dE/dx distribution in signal simulation is scaled by a scale factor obtained
 2546 from comparing the dE/dx distribution of inclusive tracks in data and in sim-
 2547 ulation. The difference in efficiency for this sample with a scaled dE/dx dis-
 2548 tribution, relative to the nominal case, is taken as a systematic uncertainty on
 2549 signal efficiency. The uncertainty is as large as 7% for low masses and falls to a
 2550 negligible effect for large masses.

2551 13.1.2.7 ELECTRON AND JET REJECTION

2552 The systematic uncertainty on the electron rejection is measured by varying the
 2553 EM fraction requirement significantly, from 0.95 to 0.9. This is found to have
 2554 a less than 0.04% effect on signal acceptance, on average, and so is completely
 2555 negligible. Similarly, the uncertainty on jet rejection is measured by tightening
 2556 the E/p requirement from 0.5 to 0.4. This is found to have no effect on signal
 2557 acceptance, so again the systematic is again negligible.

2558 13.1.2.8 MUON VETO

2559 The metastable signal region requires that the candidate tracks are not identi-
 2560 fied as medium muons because the majority of R-Hadrons in the lifetime range
 2561 included in that region do not reach the muon spectrometers before they de-
 2562 cay. However, the exponential tail of the R-Hadron lifetime distribution results
 2563 in some R-Hadrons traversing the muon spectrometer. These can still fail the
 2564 muon medium identification because they can fail on the requirement on the
 2565 number of precision hits required to pass the loose selection because they ar-
 2566 rive late to the muon spectrometer. This can be seen in Figure 71, which shows
 2567 the efficiency of the muon veto as a function of $1/\beta$, for two simulated stable
 2568 R-Hadron samples.

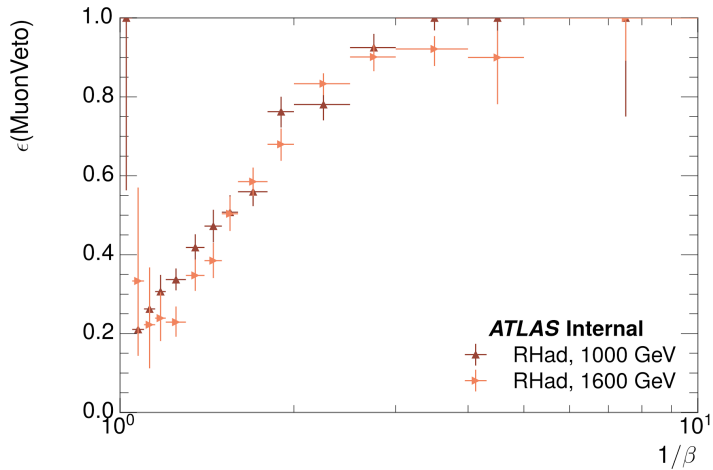


Figure 71: The efficiency of the muon veto for R -hadrons of two different masses, as a function of $1/\beta$ for simulated R-Hadron tracks.

2569 Thus, the efficiency of the muon veto depends on the timing resolution of
 2570 the spectrometer, so an uncertainty is applied to the signal efficiency to cover

2571 differences in timing resolution between data and simulation. First, a sample of
 2572 $Z \rightarrow \mu\mu$ events is selected in data in which one of the muons has a late arrival
 2573 time measured in the MDT. Then the reconstructed β distribution is compared
 2574 to the distribution in simulated $Z \rightarrow \mu\mu$ events; the difference between these
 2575 two distributions reflects the difference in timing resolution between data and
 2576 simulation. To emulate this difference in simulated signal events, the magnitude
 2577 of the difference is used to scale and shift the true β distribution of R-Hadrons in
 2578 simulation. Signal events are then reweighted based on this varied β distribution,
 2579 and the difference in the efficiency of the muon veto selection is compared with
 2580 the nominal and reweighted true β distributions. The difference in muon veto
 2581 efficiency is taken as a systematic uncertainty of the muon veto.

2582 The comparison of reconstructed β between data and simulation is performed
 2583 separately in the barrel, transition, and endcap regions of the spectrometer, and
 2584 the reweighting of the true β distribution in signal is done per region. The com-
 2585 parison of average reconstructed MDT β between data and simulation for the
 2586 barrel region is shown in Figure 72 for $Z \rightarrow \mu\mu$ events. As expected, The uncer-
 2587 tainty is found to be negligible for R-hadrons with short lifetimes, and is only
 2588 significant for lifetimes above 30 ns.

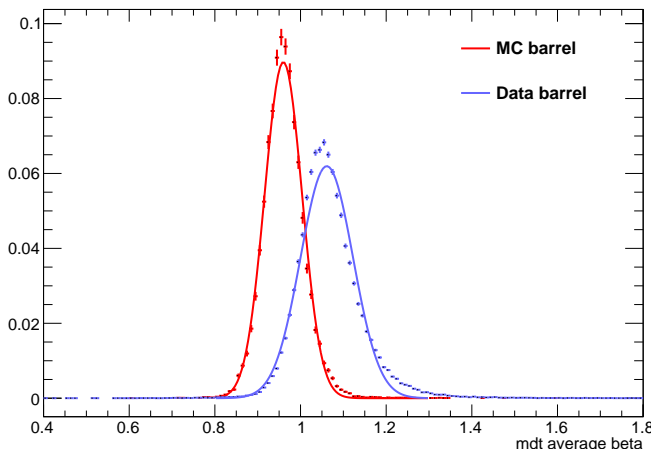


Figure 72: The average reconstructed MDT β distribution for $Z \rightarrow \mu\mu$ events in which
 one of the muons is reconstructed as a slow muon, for both data and simula-
 tion. A gaussian fit is superimposed.

2589 13.1.2.9 LUMINOSITY

2590 The luminosity uncertainty is provided by a luminosity measurement on ATLAS
 2591 and was measured to be 5% at the time of the publication of this analysis.

2592 13.1.2.10 SIGNAL SIZE

2593 As discussed in Section 10.2, the signal cross sections are calculated at NLO in the
 2594 strong coupling constant with a resummation of soft-gluon emission at NLL. The
 2595 uncertainties on those cross sections are between 14% to 28% for the R-Hadrons

Selection Region	Expected Background	Data
Stable	$17.2 \pm 2.6 \pm 1.2$	16
Metastable	$11.1 \pm 1.7 \pm 0.7$	11

Table 10: The estimated number of background events and the number of observed events in data for the specified selection regions prior to the requirement on mass. The background estimates show statistical and systematic uncertainties.

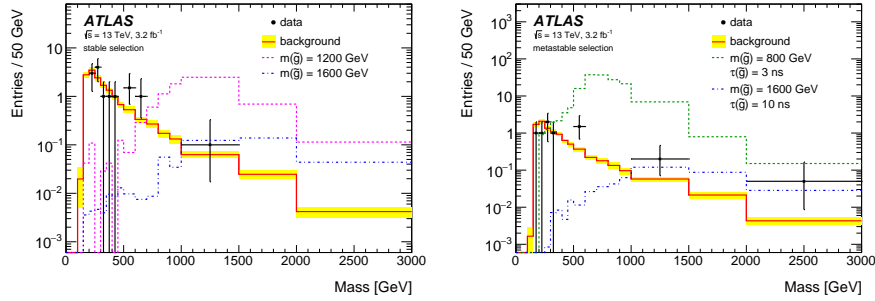


Figure 73: The observed mass distribution of events in data and the generated background distribution in (a) the stable and (b) the metastable signal region. A few example simulated signal distributions are superimposed.

2596 in the range of 400 to 1800 GeV [75, 76], where the uncertainty increases with
2597 the mass.

2598 13.2 FINAL YIELDS

2599 This full analysis was performed using the 3.2 fb^{-1} from the 2015 data-taking.
2600 Using the selections discussed in Chapter 11, sixteen events were observed in
2601 the stable signal region and eleven events were observed in the metastable signal
2602 region, prior to requirements on the candidate track mass. The background esti-
2603 mate discussed in Chapter 12 predicts $17 \pm 2.6(\text{stat}) \pm 1.2(\text{syst})$ events for the
2604 stable region and $11.1 \pm 1.7(\text{stat}) \pm 0.7(\text{syst})$ events for the metastable region.
2605 These counts are summarized in Table 10.

2606 The mass estimated using dE/dx (Section 11.4.1) provides the final discrimi-
2607 nating variable, where the signal would be expected as an excess in the falling ex-
2608 ponential tail of the expected background. The observed distribution of masses
2609 is shown in Figure 73, along with the predicted distribution from the background
2610 estimate for each signal region. Both include a few example simulated signal dis-
2611 tributions, which show the scale of an excess were the R-Hadron signals present.
2612 Their is no statistically significant evidence of an excess in the data over the back-
2613 ground estimation. From this distribution it is clearly possible to rule out signals
2614 with lower masses, around 1200 GeV, which have larger cross sections.

2615 13.3 CROSS SECTIONAL LIMITS

2616 Because there is no observed significant excess of events in the signal region, this
 2617 analysis sets upper limits on the allowed cross section for R-Hadron production.
 2618 These limits are set for each mass point by counting the observed events in data,
 2619 along with the expected background and simulated signal events, in windows of
 2620 mass. The mass windows are formed by fitting the distribution of signal events to
 2621 a Gaussian distribution, and the window is then $\pm 1.4\sigma$ around the center of that
 2622 Gaussian. Two examples of the windows formed by this procedure are shown
 2623 in Tables 11-12, for the stable and 10 ns working points. The corresponding
 2624 counts of observed data, expected background, and simulated signal for those
 2625 same working points are shown in Tables 13-14. Appendix B includes the mass
 2626 windows and counts for all of the considered signal points.

$m(\tilde{g})$ [GeV]	Left Extremum [GeV]	Right Extremum [GeV]
1000	655	1349
1100	734	1455
1200	712	1631
1300	792	1737
1400	717	1926
1500	815	2117
1600	824	2122
1700	900	2274
1800	919	2344

Table 11: The left and right extremum of the mass window for each generated mass point with a 10 ns lifetime.

$m(\tilde{g})$ [GeV]	Left Extremum [GeV]	Right Extremum [GeV]
800	627	1053
1000	726	1277
1200	857	1584
1400	924	1937
1600	993	2308
1800	1004	2554

Table 12: The left and right extremum of the mass window used for each generated stable mass point.

2627 The 95% confidence level upper limits on the cross sections for a large grid of
 2628 masses (between 800 and 1800 GeV) and lifetimes (between 0.4 and stable) are
 2629 extracted from these counts with the CL_S method using the profile likelihood

$m(\tilde{g})$ [GeV]	Expected Signal	Expected Background	Observed Data
800	462.83 ± 14.86	1.764 ± 0.080	2.0
1000	108.73 ± 3.38	1.458 ± 0.070	1.0
1200	31.74 ± 0.95	1.137 ± 0.060	1.0
1400	10.22 ± 0.29	1.058 ± 0.058	1.0
1600	3.07 ± 0.09	0.947 ± 0.054	1.0
1800	1.08 ± 0.05	0.940 ± 0.054	1.0

Table 13: The expected number of signal events, the expected number of background events, and the observed number of events in data with their respective statistical errors within the respective mass window for each generated stable mass point

$m(\tilde{g})$ [GeV]	Expected Signal	Expected Background	Observed Data
1000	144.48 ± 5.14	1.499 ± 0.069	2.0
1100	73.19 ± 2.61	1.260 ± 0.060	2.0
1200	41.54 ± 1.41	1.456 ± 0.067	2.0
1300	22.58 ± 0.77	1.201 ± 0.058	2.0
1400	12.70 ± 0.42	1.558 ± 0.071	2.0
1500	6.73 ± 0.24	1.237 ± 0.060	2.0
1600	3.90 ± 0.13	1.201 ± 0.058	2.0
1700	2.27 ± 0.07	1.027 ± 0.052	2.0
1800	1.34 ± 0.04	1.019 ± 0.052	2.0

Table 14: The expected number of signal events, the expected number of background events, and the observed number of events in data with their respective statistical errors within the respective mass window for each generated mass point with a lifetime of 10 ns.

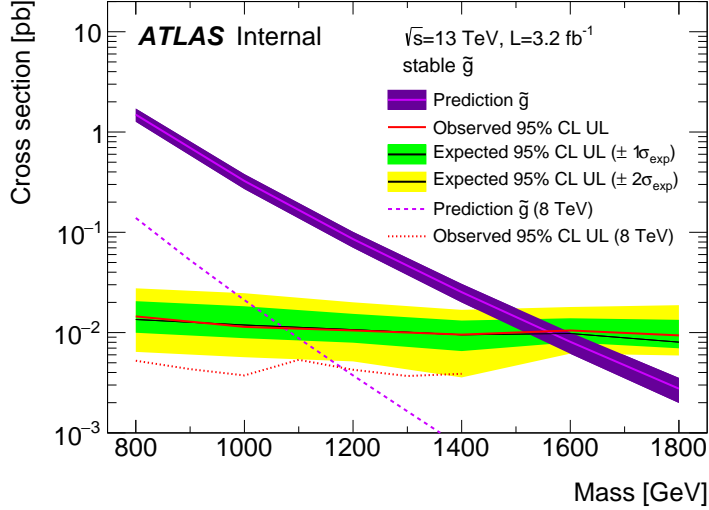


Figure 74: The observed and expected cross section limits as a function of mass for the stable simulated signal. The predicted cross section values for the corresponding signals are included.

ratio as a test statistic [80]. For this procedure, the systematic uncertainties estimated for the signal and background yields are treated as Gaussian-distributed nuisance parameters. The uncertainty on the normalization of the expected background distribution is included in the expected background events. At this point the expected cross section limit is calculated for both the metastable and stable signal region for each lifetime point, and the region with the best expected limit is selected for each lifetime. Using that procedure, the metastable region is used for lifetimes up to and including 30 ns, and the stable region for lifetimes above it.

The resulting cross-sectional upper limits are shown as a function of mass in Figure 74 and Figure 75 for each lifetime considered. The limits are interpolated linearly between each mass point, and the dependence of the limit on the mass is small as the efficiency is relatively constant for large R-Hadron masses. There is however a strong dependence on lifetime, as discussed in Section 11.5, where the probability to form a fully reconstructed track and the kinematic freedom to produce E_T^{miss} result in a local maximum in the limit at 10–30 ns. The figures also include the expected cross section for pair-produced gluino R-Hadrons for reference. For the 10 ns and stable cross section limits, both the observed limit and expected cross section for the Run 1, 8 TeV version of this analysis are included. There the cross sectional limits are lower because of the increased available luminosity, while the signal cross sections were also much lower because of the lower collision energy.

13.4 MASS LIMITS

The cross-sectional limits can then be used to derive a lower mass limit for gluino R-Hadrons by comparing them to the theoretically predicted production cross

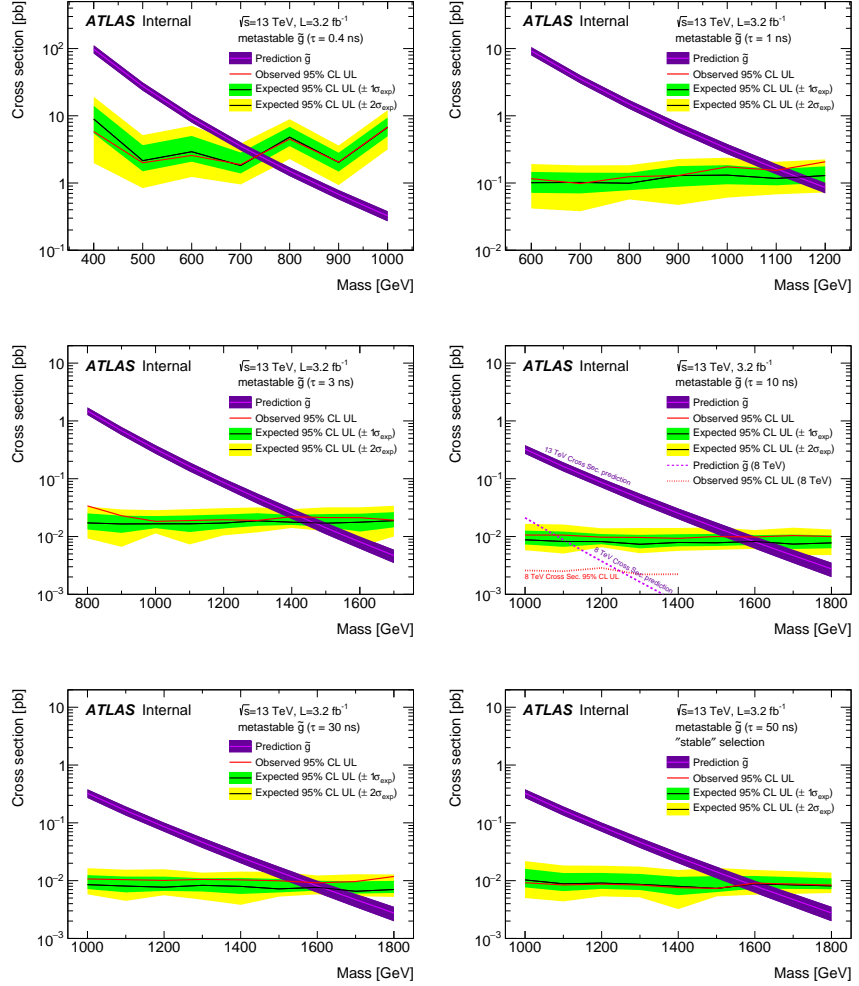


Figure 75: The observed and expected cross section limits as a function of mass for each generated lifetime. The predicted cross section values for the corresponding signals are included.

sections. These mass limits range from only 740 GeV at the lowest lifetimes considered, where the selection efficiency is very low, to up to 1580 GeV at 30 ns where the selection efficiency is maximized. The observed and expected mass limits for each lifetime point are detailed in Table 15, which also lists which selection region was used for each lifetime. These excluded range of masses as a function of lifetime is also shown in Figure 76. The Run 1 limits are included for comparison; the limits have increased by about 200 GeV on average. The search has also improved since the previous incarnation from Run 1 in optimizing the region between 30 GeV and detector-stable lifetimes by introducing the second signal region. The definition of the stable region prevents the significant drop in mass limit that occurred above 30 GeV in the Run 1 analysis.

Selection	τ [ns]	$M_{\text{obs}} > [\text{GeV}]$	$M_{\text{exp}} > [\text{GeV}]$
Metastable	0.4	740	730
"	1.0	1110	1150
"	3.0	1430	1470
"	10	1570	1600
"	30	1580	1620
Stable	50	1590	1590
"	stable	1570	1580

Table 15: The observed and expected 95% CL lower limit on mass for gluino R-Hadrons for each considered lifetime.

13.5 CONTEXT FOR LONG-LIVED SEARCHES

This search plays an important role in the current, combined [ATLAS](#) search for long lived particles. The mass limits provided by various [ATLAS](#) searches for long-lived gluino R-Hadrons can be seen in Figure 77. This search provides the most competitive limit for lifetimes between 3 ns up through very long lifetimes, where it is still competitive with dedicated searches for stable particles. The limits placed on gluino production are very similar to the limits on promptly decaying models.

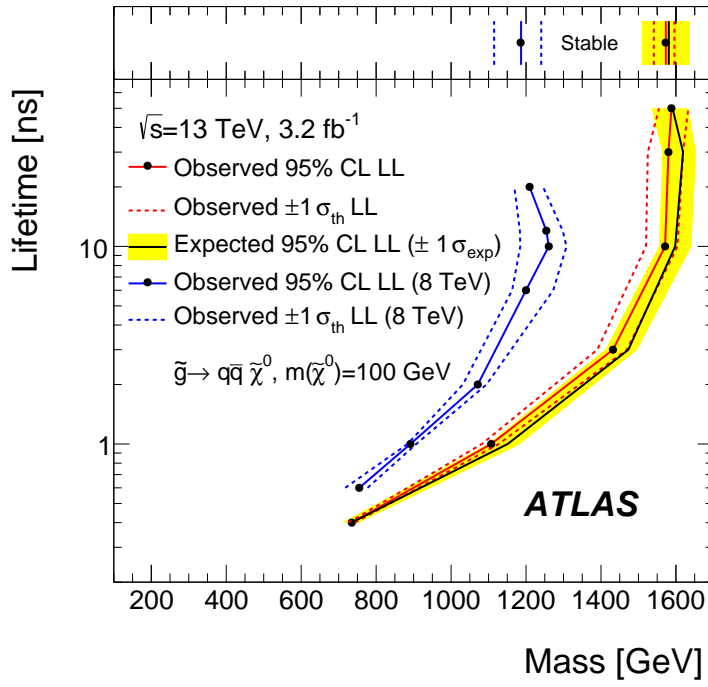


Figure 76: The excluded range of masses as a function of gluino lifetime. The expected lower limit (LL), with its experimental $\pm 1\sigma$ band, is given with respect to the nominal theoretical cross-section. The observed 95% LL obtained at $\sqrt{s} = 8 \text{ TeV}$ [63] is also shown for comparison.

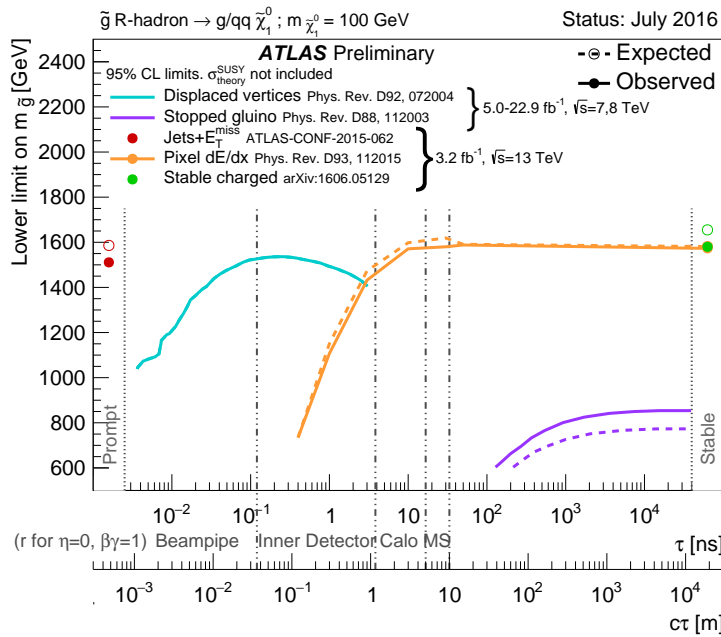


Figure 77: The constraints on the gluino mass as a function of lifetime for a split-supersymmetry model with the gluino R-Hadrons decaying into a gluon or light quarks and a neutralino with mass of 100 GeV. The solid lines indicate the observed limits, while the dashed lines indicate the expected limits. The area below the curves is excluded. The dots represent results for which the particle is assumed to be prompt or stable.

2674

PART VI

2675

CONCLUSIONS

2676

You can put some informational part preamble text here.

14

2677

2678 SUMMARY AND OUTLOOK

2679 14.1 SUMMARY

2680 14.2 OUTLOOK

2681

PART VII

2682

APPENDIX

2683

A

2684

2685 INELASTIC CROSS SECTION

B

2686

²⁶⁸⁷ EXPANDED R-HADRON YIELDS AND LIMITS

$m(\tilde{g})$ [GeV]	Left Extremum [GeV]	Right Extremum [GeV]
1000	682	1387
1100	763	1478
1200	801	1606
1300	809	1841
1400	861	2011
1500	920	2032
1600	952	2173
1800	1017	2422

Table 16: The left and right extremum of the mass window for each generated mass point with a 50 ns lifetime.

$m(\tilde{g})$ [GeV]	Left Extremum [GeV]	Right Extremum [GeV]
1000	689	1321
1100	746	1513
1200	788	1670
1300	860	1734
1400	833	1925
1500	852	2048
1600	833	2283
1700	946	2379
1800	869	2505

Table 17: The left and right extremum of the mass window for each generated mass point with a 30 ns lifetime.

$m(\tilde{g})$ [GeV]	Left Extremum [GeV]	Right Extremum [GeV]
1000	655	1349
1100	734	1455
1200	712	1631
1300	792	1737
1400	717	1926
1500	815	2117
1600	824	2122
1700	900	2274
1800	919	2344

Table 18: The left and right extremum of the mass window for each generated mass point with a 10 ns lifetime.

$m(\tilde{g})$ [GeV]	Left Extremum [GeV]	Right Extremum [GeV]
800	531	1065
900	576	1165
1000	610	1345
1100	635	1432
1200	663	1563
1300	620	1667
1400	742	1727
1500	761	1937
1600	573	2000
1700	621	2182

Table 19: The left and right extremum of the mass window used for each generated mass point with a lifetime of 3 ns.

$m(\tilde{g})$ [GeV]	Left Extremum [GeV]	Right Extremum [GeV]
600	411	758
700	385	876
800	486	970
900	406	987
1000	408	1136
1100	555	1196
1200	516	1378

Table 20: The left and right extremum of the mass window used for each mass point with a lifetime of 1 ns.

$m(\tilde{g})$ [GeV]	Left Extremum [GeV]	Right Extremum [GeV]
400	204	510
500	295	639
600	288	702
700	323	701
800	190	771
900	277	677
1000	249	688

Table 21: The left and right extremum of the mass window for each generated mass point with a lifetime of 0.4 ns.

$m(\tilde{g})$ [GeV]	Left Extremum [GeV]	Right Extremum [GeV]
800	627	1053
1000	726	1277
1200	857	1584
1400	924	1937
1600	993	2308
1800	1004	2554

Table 22: The left and right extremum of the mass window used for each generated stable mass point.

$m(\tilde{g})$ [GeV]	Expected Signal	Expected Background	Observed Data
1000	131.18 ± 6.35	1.803 ± 0.081	1.0 ± 1.0
1100	71.11 ± 3.35	1.409 ± 0.069	1.0 ± 1.0
1200	37.18 ± 1.75	1.310 ± 0.066	1.0 ± 1.0
1300	20.76 ± 0.95	1.431 ± 0.069	1.0 ± 1.0
1400	12.63 ± 0.57	1.273 ± 0.065	1.0 ± 1.0
1500	6.57 ± 0.29	1.115 ± 0.059	1.0 ± 1.0
1600	3.56 ± 0.16	1.041 ± 0.057	1.0 ± 1.0
1800	1.27 ± 0.05	0.918 ± 0.053	1.0 ± 1.0

Table 23: The expected number of signal events, the expected number of background events, and the observed number of events in data with their respective statistical errors within the respective mass window for each generated mass point with a lifetime of 50 ns.

$m(\tilde{g})$ [GeV]	Expected Signal	Expected Background	Observed Data
1000	144.65 ± 6.34	1.328 ± 0.063	2.0 ± 1.4
1100	75.28 ± 3.27	1.255 ± 0.060	2.0 ± 1.4
1200	40.51 ± 1.75	1.193 ± 0.058	2.0 ± 1.4
1300	20.91 ± 0.93	0.997 ± 0.051	2.0 ± 1.4
1400	11.97 ± 0.51	1.131 ± 0.056	2.0 ± 1.4
1500	6.81 ± 0.28	1.111 ± 0.055	2.0 ± 1.4
1600	4.19 ± 0.16	1.193 ± 0.058	2.0 ± 1.4
1700	2.42 ± 0.09	0.963 ± 0.050	2.0 ± 1.4
1800	1.46 ± 0.05	1.138 ± 0.056	3.0 ± 1.7

Table 24: The expected number of signal events, the expected number of background events, and the observed number of events in data with their respective statistical errors within the respective mass window for each generated mass point with a lifetime of 30 ns.

$m(\tilde{g})$ [GeV]	Expected Signal	Expected Background	Observed Data
1000	144.48 ± 5.14	1.499 ± 0.069	2.0 ± 1.4
1100	73.19 ± 2.61	1.260 ± 0.060	2.0 ± 1.4
1200	41.54 ± 1.41	1.456 ± 0.067	2.0 ± 1.4
1300	22.58 ± 0.77	1.201 ± 0.058	2.0 ± 1.4
1400	12.70 ± 0.42	1.558 ± 0.071	2.0 ± 1.4
1500	6.73 ± 0.24	1.237 ± 0.060	2.0 ± 1.4
1600	3.90 ± 0.13	1.201 ± 0.058	2.0 ± 1.4
1700	2.27 ± 0.07	1.027 ± 0.052	2.0 ± 1.4
1800	1.34 ± 0.04	1.019 ± 0.052	2.0 ± 1.4

Table 25: The expected number of signal events, the expected number of background events, and the observed number of events in data with their respective statistical errors within the respective mass window for each generated mass point with a lifetime of 10 ns.

$m(\tilde{g})$ [GeV]	Expected Signal	Expected Background	Observed Data
800	362.97 ± 14.68	1.841 ± 0.080	5.0 ± 2.2
900	169.20 ± 6.69	1.710 ± 0.076	3.0 ± 1.7
1000	84.78 ± 3.23	1.727 ± 0.076	2.0 ± 1.4
1100	40.06 ± 1.60	1.679 ± 0.075	2.0 ± 1.4
1200	20.06 ± 0.81	1.598 ± 0.072	2.0 ± 1.4
1300	10.76 ± 0.43	1.851 ± 0.080	2.0 ± 1.4
1400	5.52 ± 0.22	1.374 ± 0.064	2.0 ± 1.4
1500	3.16 ± 0.13	1.355 ± 0.064	2.0 ± 1.4
1600	2.13 ± 0.11	2.235 ± 0.093	3.0 ± 1.7
1700	1.10 ± 0.06	1.995 ± 0.085	2.0 ± 1.4

Table 26: The expected number of signal events, the expected number of background events, and the observed number of events in data with their respective statistical errors within the respective mass window for each generated mass point with a lifetime of 3 ns.

$m(\tilde{g})$ [GeV]	Expected Signal	Expected Background	Observed Data
600	431.80 ± 36.60	2.418 ± 0.099	3.0 ± 1.7
700	192.77 ± 15.28	3.267 ± 0.126	3.0 ± 1.7
800	69.63 ± 5.90	2.125 ± 0.089	3.0 ± 1.7
900	28.91 ± 2.59	3.114 ± 0.121	3.0 ± 1.7
1000	13.64 ± 1.22	3.359 ± 0.129	5.0 ± 2.2
1100	6.13 ± 0.57	1.879 ± 0.081	3.0 ± 1.7
1200	3.24 ± 0.30	2.387 ± 0.098	5.0 ± 2.2

Table 27: The expected number of signal events, the expected number of background events, and the observed number of events in data with their respective statistical errors within the respective mass window for each generated mass point with a lifetime of 1 ns.

$m(\tilde{g})$ [GeV]	Expected Signal	Expected Background	Observed Data
400	181.71 ± 75.59	6.780 ± 0.238	4.0 ± 2.0
500	103.88 ± 30.05	4.310 ± 0.160	4.0 ± 2.0
600	28.34 ± 9.34	4.868 ± 0.177	4.0 ± 2.0
700	13.62 ± 4.00	3.908 ± 0.147	4.0 ± 2.0
800	2.75 ± 1.15	9.001 ± 0.308	8.0 ± 2.8
900	2.25 ± 0.71	5.045 ± 0.183	5.0 ± 2.2
1000	0.34 ± 0.19	6.026 ± 0.214	6.0 ± 2.4

Table 28: The expected number of signal events, the expected number of background events, and the observed number of events in data with their respective statistical errors within the respective mass window for each generated mass point with a lifetime of p4 ns.

$m(\tilde{g})$ [GeV]	Expected Signal	Expected Background	Observed Data
800	462.83 ± 14.86	1.764 ± 0.080	2.0 ± 1.4
1000	108.73 ± 3.38	1.458 ± 0.070	1.0 ± 1.0
1200	31.74 ± 0.95	1.137 ± 0.060	1.0 ± 1.0
1400	10.22 ± 0.29	1.058 ± 0.058	1.0 ± 1.0
1600	3.07 ± 0.09	0.947 ± 0.054	1.0 ± 1.0
1800	1.08 ± 0.05	0.940 ± 0.054	1.0 ± 1.0

Table 29: The expected number of signal events, the expected number of background events, and the observed number of events in data with their respective statistical errors within the respective mass window for each generated stable mass point

- 2689 [1] Lyndon Evans and Philip Bryant. "LHC Machine". In: *JINST* 3 (2008), S08001.
2690 doi: [10.1088/1748-0221/3/08/S08001](https://doi.org/10.1088/1748-0221/3/08/S08001).
- 2691 [2] C Lefevre. "LHC: the guide (English version). Guide du LHC (version anglaise)".
2692 2009. URL: <https://cds.cern.ch/record/1165534>.
- 2693 [3] ATLAS Collaboration. "The ATLAS Experiment at the CERN Large Hadron
2694 Collider". In: *JINST* 3 (2008), S08003. doi: [10.1088/1748-0221/3/08/S08003](https://doi.org/10.1088/1748-0221/3/08/S08003).
- 2696 [4] S. Chatrchyan et al. "The CMS experiment at the CERN LHC". In: *JINST*
2697 3 (2008), S08004. doi: [10.1088/1748-0221/3/08/S08004](https://doi.org/10.1088/1748-0221/3/08/S08004).
- 2698 [5] A. Augusto Alves Jr. et al. "The LHCb Detector at the LHC". In: *JINST* 3
2699 (2008), S08005. doi: [10.1088/1748-0221/3/08/S08005](https://doi.org/10.1088/1748-0221/3/08/S08005).
- 2700 [6] K. Aamodt et al. "The ALICE experiment at the CERN LHC". In: *JINST* 3
2701 (2008), S08002. doi: [10.1088/1748-0221/3/08/S08002](https://doi.org/10.1088/1748-0221/3/08/S08002).
- 2702 [7] K. A. Olive et al. "Review of Particle Physics". In: *Chin. Phys. C* 38 (2014),
2703 p. 090001. doi: [10.1088/1674-1137/38/9/090001](https://doi.org/10.1088/1674-1137/38/9/090001).
- 2704 [8] Daniel Froidevaux and Paris Sphicas. "General-Purpose Detectors for the
2705 Large Hadron Collider". In: *Annual Review of Nuclear and Particle Science*
2706 56.1 (2006), pp. 375–440. doi: [10.1146/annurev.nucl.54.070103.181209](https://doi.org/10.1146/annurev.nucl.54.070103.181209). URL: <http://dx.doi.org/10.1146/annurev.nucl.54.070103.181209>.
- 2707 [9] M Capeans, G Darbo, K Einsweiller, M Elsing, T Flick, M Garcia-Sciveres,
2708 C Gemme, H Pernegger, O Rohne, and R Vuillermet. *ATLAS Insertable B-*
2709 *Layer Technical Design Report*. Tech. rep. CERN-LHCC-2010-013. ATLAS-
2710 TDR-19. 2010. URL: <https://cds.cern.ch/record/1291633>.
- 2711 [10] S. Agostinelli et al. "GEANT4: A simulation toolkit". In: *Nucl. Instrum. Meth.*
2712 A 506 (2003), pp. 250–303. doi: [10.1016/S0168-9002\(03\)01368-8](https://doi.org/10.1016/S0168-9002(03)01368-8).
- 2713 [11] ATLAS Collaboration. "A study of the material in the ATLAS inner de-
2714 tector using secondary hadronic interactions". In: *JINST* 7 (2012), P01013.
2715 doi: [10.1088/1748-0221/7/01/P01013](https://doi.org/10.1088/1748-0221/7/01/P01013). arXiv: [1110.6191 \[hep-ex\]](https://arxiv.org/abs/1110.6191).
2716 PERF-2011-08.
- 2717 [12] ATLAS Collaboration. "Electron and photon energy calibration with the
2718 ATLAS detector using LHC Run 1 data". In: *Eur. Phys. J. C* 74 (2014), p. 3071.
2719 doi: [10.1140/epjc/s10052-014-3071-4](https://doi.org/10.1140/epjc/s10052-014-3071-4). arXiv: [1407.5063](https://arxiv.org/abs/1407.5063)
2720 [hep-ex]. PERF-2013-05.
- 2721 [13] ATLAS Collaboration. "A measurement of the calorimeter response to sin-
2722 gle hadrons and determination of the jet energy scale uncertainty using
2723 LHC Run-1 pp -collision data with the ATLAS detector". In: (2016). arXiv:
2724 [1607.08842 \[hep-ex\]](https://arxiv.org/abs/1607.08842). PERF-2015-05.
- 2725
- 2726

- [14] ATLAS Collaboration. “Single hadron response measurement and calorimeter jet energy scale uncertainty with the ATLAS detector at the LHC”. In: *Eur. Phys. J. C* 73 (2013), p. 2305. doi: [10.1140/epjc/s10052-013-2305-1](https://doi.org/10.1140/epjc/s10052-013-2305-1). arXiv: [1203.1302 \[hep-ex\]](https://arxiv.org/abs/1203.1302). PERF-2011-05.
- [15] ATLAS Collaboration. “The ATLAS Simulation Infrastructure”. In: *Eur. Phys. J. C* 70 (2010), p. 823. doi: [10.1140/epjc/s10052-010-1429-9](https://doi.org/10.1140/epjc/s10052-010-1429-9). arXiv: [1005.4568 \[hep-ex\]](https://arxiv.org/abs/1005.4568). SOFT-2010-01.
- [16] T. Sjöstrand, S. Mrenna, and P. Skands. “A Brief Introduction to PYTHIA 8.1”. In: *Comput. Phys. Commun.* 178 (2008), pp. 852–867. doi: [10.1016/j.cpc.2008.01.036](https://doi.org/10.1016/j.cpc.2008.01.036). arXiv: [0710.3820](https://arxiv.org/abs/0710.3820).
- [17] ATLAS Collaboration. *Summary of ATLAS Pythia 8 tunes*. ATL-PHYS-PUB-2012-003. 2012. URL: <http://cds.cern.ch/record/1474107>.
- [18] A.D. Martin, W.J. Stirling, R.S. Thorne, and G. Watt. “Parton distributions for the LHC”. In: *Eur. Phys. J. C* 63 (2009). Figures from the MSTW Website, pp. 189–285. doi: [10.1140/epjc/s10052-009-1072-5](https://doi.org/10.1140/epjc/s10052-009-1072-5). arXiv: [0901.0002](https://arxiv.org/abs/0901.0002).
- [19] A. Sherstnev and R.S. Thorne. “Parton Distributions for LO Generators”. In: *Eur. Phys. J. C* 55 (2008), pp. 553–575. doi: [10.1140/epjc/s10052-008-0610-x](https://doi.org/10.1140/epjc/s10052-008-0610-x). arXiv: [0711.2473](https://arxiv.org/abs/0711.2473).
- [20] A. Ribon et al. *Status of Geant4 hadronic physics for the simulation of LHC experiments at the start of LHC physics program*. CERN-LCGAPP-2010-02. 2010. URL: <http://lcgapp.cern.ch/project/docs/noteStatusHadronic2010.pdf>.
- [21] M. P. Guthrie, R. G. Alsmiller, and H. W. Bertini. “Calculation of the capture of negative pions in light elements and comparison with experiments pertaining to cancer radiotherapy”. In: *Nucl. Instrum. Meth.* 66 (1968), pp. 29–36. doi: [10.1016/0029-554X\(68\)90054-2](https://doi.org/10.1016/0029-554X(68)90054-2).
- [22] H. W. Bertini and P. Guthrie. “News item results from medium-energy intranuclear-cascade calculation”. In: *Nucl. Instr. and Meth. A* 169 (1971), p. 670. doi: [10.1016/0375-9474\(71\)90710-X](https://doi.org/10.1016/0375-9474(71)90710-X).
- [23] V.A. Karmanov. “Light Front Wave Function of Relativistic Composite System in Explicitly Solvable Model”. In: *Nucl. Phys. B* 166 (1980), p. 378. doi: [10.1016/0550-3213\(80\)90204-7](https://doi.org/10.1016/0550-3213(80)90204-7).
- [24] H. S. Fesefeldt. *GHEISHA program*. Pitha-85-02, Aachen. 1985.
- [25] G. Folger and J.P. Wellisch. “String parton models in Geant4”. In: (2003). arXiv: [nucl-th/0306007](https://arxiv.org/abs/nucl-th/0306007).
- [26] N. S. Amelin et al. “Transverse flow and collectivity in ultrarelativistic heavy-ion collisions”. In: *Phys. Rev. Lett.* 67 (1991), p. 1523. doi: [10.1103/PhysRevLett.67.1523](https://doi.org/10.1103/PhysRevLett.67.1523).
- [27] N. S. Amelin et al. “Collectivity in ultrarelativistic heavy ion collisions”. In: *Nucl. Phys. A* 544 (1992), p. 463. doi: [10.1016/0375-9474\(92\)90598-E](https://doi.org/10.1016/0375-9474(92)90598-E).

- 2769 [28] L. V. Bravina et al. “Fluid dynamics and Quark Gluon string model - What
2770 we can expect for Au+Au collisions at 11.6 AGeV/c”. In: *Nucl. Phys. A* 566
2771 (1994), p. 461. doi: [10.1016/0375-9474\(94\)90669-6](https://doi.org/10.1016/0375-9474(94)90669-6).
- 2772 [29] L. V. Bravin et al. “Scaling violation of transverse flow in heavy ion colli-
2773 sions at AGS energies”. In: *Phys. Lett. B* 344 (1995), p. 49. doi: [10.1016/0370-2693\(94\)01560-Y](https://doi.org/10.1016/0370-2693(94)01560-Y).
- 2775 [30] B. Andersson et al. “A model for low-pT hadronic reactions with general-
2776 izations to hadron-nucleus and nucleus-nucleus collisions”. In: *Nucl. Phys.*
2777 *B* 281 (1987), p. 289. doi: [10.1016/0550-3213\(87\)90257-4](https://doi.org/10.1016/0550-3213(87)90257-4).
- 2778 [31] B. Andersson, A. Tai, and B.-H. Sa. “Final state interactions in the (nuclear)
2779 FRITIOF string interaction scenario”. In: *Z. Phys. C* 70 (1996), pp. 499–
2780 506. doi: [10.1007/s002880050127](https://doi.org/10.1007/s002880050127).
- 2781 [32] B. Nilsson-Almqvist and E. Stenlund. “Interactions Between Hadrons and
2782 Nuclei: The Lund Monte Carlo, Fritiof Version 1.6”. In: *Comput. Phys. Com-*
2783 *mun.* 43 (1987), p. 387. doi: [10.1016/0010-4655\(87\)90056-7](https://doi.org/10.1016/0010-4655(87)90056-7).
- 2784 [33] B. Ganhuyag and V. Uzhinsky. “Modified FRITIOF code: Negative charged
2785 particle production in high energy nucleus nucleus interactions”. In: *Czech.*
2786 *J. Phys.* 47 (1997), pp. 913–918. doi: [10.1023/A:1021296114786](https://doi.org/10.1023/A:1021296114786).
- 2787 [34] ATLAS Collaboration. “Topological cell clustering in the ATLAS calorime-
2788 ters and its performance in LHC Run 1”. In: (2016). arXiv: [1603.02934](https://arxiv.org/abs/1603.02934)
[hep-ex].
- 2790 [35] Peter Speckmayer. “Energy Measurement of Hadrons with the CERN AT-
2791 LAS Calorimeter”. Presented on 18 Jun 2008. PhD thesis. Vienna: Vienna,
2792 Tech. U., 2008. URL: <http://cds.cern.ch/record/1112036>.
- 2793 [36] CMS Collaboration. “The CMS barrel calorimeter response to particle
2794 beams from 2 to 350 GeV/c”. In: *Eur. Phys. J. C* 60.3 (2009). doi: [10.1140/epjc/s10052-009-0959-5](https://doi.org/10.1140/epjc/s10052-009-0959-5).
- 2796 [37] J. Beringer et al. (Particle Data Group). “Review of Particle Physics”. In:
2797 *Chin. Phys. C* 38 (2014), p. 090001. URL: <http://pdg.lbl.gov>.
- 2798 [38] P. Adragna et al. “Measurement of Pion and Proton Response and Lon-
2799 gitudinal Shower Profiles up to 20 Nuclear Interaction Lengths with the
2800 ATLAS Tile Calorimeter”. In: *Nucl. Instrum. Meth. A* 615 (2010), pp. 158–
2801 181. doi: [10.1016/j.nima.2010.01.037](https://doi.org/10.1016/j.nima.2010.01.037).
- 2802 [39] ATLAS Collaboration. “Jet energy measurement and its systematic uncer-
2803 tainty in proton–proton collisions at $\sqrt{s} = 7$ TeV with the ATLAS detec-
2804 tor”. In: *Eur. Phys. J. C* 75 (2015), p. 17. doi: [10.1140/epjc/s10052-014-3190-y](https://doi.org/10.1140/epjc/s10052-014-3190-y). arXiv: [1406.0076](https://arxiv.org/abs/1406.0076) [hep-ex]. PERF-2012-01.
- 2806 [40] Hung-Liang Lai, Marco Guzzi, Joey Huston, Zhao Li, Pavel M. Nadolsky,
2807 et al. “New parton distributions for collider physics”. In: *Phys. Rev. D* 82
2808 (2010), p. 074024. doi: [10.1103/PhysRevD.82.074024](https://doi.org/10.1103/PhysRevD.82.074024). arXiv: [1007.2241](https://arxiv.org/abs/1007.2241) [hep-ph].

- 2810 [41] E. Abat et al. “Study of energy response and resolution of the ATLAS barrel
 2811 calorimeter to hadrons of energies from 20 to 350 GeV”. In: *Nucl. Instrum.*
 2812 *Meth. A* 621.1-3 (2010), pp. 134 – 150. doi: <http://dx.doi.org/10.1016/j.nima.2010.04.054>.
- 2814 [42] ATLAS Collaboration. “Jet energy measurement with the ATLAS detector
 2815 in proton–proton collisions at $\sqrt{s} = 7$ TeV”. In: *Eur. Phys. J. C* 73 (2013),
 2816 p. 2304. doi: <10.1140/epjc/s10052-013-2304-2>. arXiv: [1112.6426 \[hep-ex\]](1112.6426). PERF-2011-03.
- 2818 [43] Nausheen R. Shah and Carlos E. M. Wagner. “Gravitons and dark matter in
 2819 universal extra dimensions”. In: *Phys. Rev. D* 74 (2006), p. 104008. doi: <10.1103/PhysRevD.74.104008>. arXiv: [hep-ph/0608140 \[hep-ph\]](hep-ph/0608140).
- 2821 [44] Jonathan L. Feng, Arvind Rajaraman, and Fumihiro Takayama. “Graviton
 2822 cosmology in universal extra dimensions”. In: *Phys. Rev. D* 68 (2003), p. 085018.
 2823 doi: <10.1103/PhysRevD.68.085018>. arXiv: [hep-ph/0307375 \[hep-ph\]](hep-ph/0307375).
- 2825 [45] Paul H. Frampton and Pham Quang Hung. “Long-lived quarks?” In: *Phys.*
 2826 *Rev. D* 58 (5 1998), p. 057704. doi: <10.1103/PhysRevD.58.057704>.
 2827 URL: <http://link.aps.org/doi/10.1103/PhysRevD.58.057704>.
- 2829 [46] C. Friberg, E. Norrbin, and T. Sjostrand. “QCD aspects of leptoquark pro-
 2830 duction at HERA”. In: *Phys. Lett. B* 403 (1997), pp. 329–334. doi: [10.1016/S0370-2693\(97\)00543-1](10.1016/S0370-2693(97)00543-1). arXiv: [hep-ph/9704214 \[hep-ph\]](hep-ph/9704214).
- 2832 [47] Herbert K. Dreiner. “An introduction to explicit R-parity violation”. In:
 2833 (1997). arXiv: <hep-ph/9707435>.
- 2834 [48] Edmond L. Berger and Zack Sullivan. “Lower limits on R-parity-violating
 2835 couplings in supersymmetry”. In: *Phys. Rev. Lett.* 92 (2004), p. 201801. doi:
 2836 <10.1103/PhysRevLett.92.201801>. arXiv: <hep-ph/0310001>.
- 2837 [49] R. Barbieri, C. Berat, M. Besancon, M. Chemtob, A. Deandrea, et al. “R-
 2838 parity violating supersymmetry”. In: *Phys. Rept.* 420 (2005), p. 1. doi: <10.1016/j.physrep.2005.08.006>. arXiv: <hep-ph/0406039>.
- 2840 [50] M. Fairbairn et al. “Stable massive particles at colliders”. In: *Phys. Rept.* 438
 2841 (2007), p. 1. doi: <10.1016/j.physrep.2006.10.002>. arXiv: <hep-ph/0611040>.
- 2843 [51] Christopher F. Kolda. “Gauge-mediated supersymmetry breaking: Intro-
 2844 duction, review and update”. In: *Nucl. Phys. Proc. Suppl.* 62 (1998), p. 266.
 2845 doi: [10.1016/S0920-5632\(97\)00667-1](10.1016/S0920-5632(97)00667-1). arXiv: <hep-ph/9707450>.
- 2846 [52] Howard Baer, Kingman Cheung, and John F. Gunion. “A Heavy gluino as
 2847 the lightest supersymmetric particle”. In: *Phys. Rev. D* 59 (1999), p. 075002.
 2848 doi: <10.1103/PhysRevD.59.075002>. arXiv: <hep-ph/9806361>.
- 2849 [53] S. James Gates Jr. and Oleg Lebedev. “Searching for supersymmetry in
 2850 hadrons”. In: *Phys. Lett. B* 477 (2000), p. 216. doi: [10.1016/S0370-2693\(00\)00172-6](10.1016/S0370-2693(00)00172-6). arXiv: <hep-ph/9912362>.

- 2852 [54] G. F. Giudice and A. Romanino. “Split supersymmetry”. In: *Nucl. Phys. B*
 2853 699 (2004), p. 65. doi: [10.1016/j.nuclphysb.2004.11.048](https://doi.org/10.1016/j.nuclphysb.2004.11.048). arXiv:
 2854 [hep-ph/0406088](https://arxiv.org/abs/hep-ph/0406088).
- 2855 [55] N. Arkani-Hamed, S. Dimopoulos, G. F. Giudice, and A. Romanino. “As-
 2856 pects of split supersymmetry”. In: *Nucl. Phys. B* 709 (2005), p. 3. doi: [10.1016/j.nuclphysb.2004.12.026](https://doi.org/10.1016/j.nuclphysb.2004.12.026). arXiv: [hep-ph/0409232](https://arxiv.org/abs/hep-ph/0409232).
- 2857 [56] Glennys R. Farrar and Pierre Fayet. “Phenomenology of the Production,
 2858 Decay, and Detection of New Hadronic States Associated with Supersym-
 2859 metry”. In: *Phys. Lett.* B76 (1978), pp. 575–579. doi: [10.1016/0370-2693\(78\)90858-4](https://doi.org/10.1016/0370-2693(78)90858-4).
- 2860 [57] A. C. Kraan, J. B. Hansen, and P. Nevski. “Discovery potential of R-hadrons
 2861 with the ATLAS detector”. In: *Eur. Phys. J.* C49 (2007), pp. 623–640. doi:
 2862 [10.1140/epjc/s10052-006-0162-x](https://doi.org/10.1140/epjc/s10052-006-0162-x). arXiv: [hep-ex/0511014](https://arxiv.org/abs/hep-ex/0511014)
 2863 [[hep-ex](#)].
- 2864 [58] Rasmus Mckeprang and David Milstead. “An Updated Description of
 2865 Heavy-Hadron Interactions in GEANT-4”. In: *Eur. Phys. J.* C66 (2010), pp. 493–
 2866 501. doi: [10.1140/epjc/s10052-010-1262-1](https://doi.org/10.1140/epjc/s10052-010-1262-1). arXiv: [0908.1868](https://arxiv.org/abs/0908.1868)
 2867 [[hep-ph](#)].
- 2868 [59] ATLAS Collaboration. “Search for massive, long-lived particles using mul-
 2869 titrack displaced vertices or displaced lepton pairs in pp collisions at $\sqrt{s} =$
 2870 8 TeV with the ATLAS detector”. In: *Phys. Rev. D* 92 (2015), p. 072004.
 2871 doi: [10.1103/PhysRevD.92.072004](https://doi.org/10.1103/PhysRevD.92.072004). arXiv: [1504.05162](https://arxiv.org/abs/1504.05162) [[hep-ex](#)].
 2872 SUSY-2014-02.
- 2873 [60] ATLAS Collaboration. “Search for charginos nearly mass degenerate with
 2874 the lightest neutralino based on a disappearing-track signature in pp col-
 2875 lisions at $\sqrt{s} = 8$ TeV with the ATLAS detector”. In: *Phys. Rev. D* 88 (2013),
 2876 p. 112006. doi: [10.1103/PhysRevD.88.112006](https://doi.org/10.1103/PhysRevD.88.112006). arXiv: [1310.3675](https://arxiv.org/abs/1310.3675)
 2877 [[hep-ex](#)]. SUSY-2013-01.
- 2878 [61] ATLAS Collaboration. “Searches for heavy long-lived sleptons and R-Hadrons
 2879 with the ATLAS detector in pp collisions at $\sqrt{s} = 7$ TeV”. In: *Phys. Lett. B*
 2880 720 (2013), p. 277. doi: [10.1016/j.physletb.2013.02.015](https://doi.org/10.1016/j.physletb.2013.02.015). arXiv:
 2881 [1211.1597](https://arxiv.org/abs/1211.1597) [[hep-ex](#)]. SUSY-2012-01.
- 2882 [62] ATLAS Collaboration. “Searches for heavy long-lived charged particles
 2883 with the ATLAS detector in proton–proton collisions at $\sqrt{s} = 8$ TeV”. In: *JHEP* 01 (2015), p. 068. doi: [10.1007/JHEP01\(2015\)068](https://doi.org/10.1007/JHEP01(2015)068). arXiv:
 2884 [1411.6795](https://arxiv.org/abs/1411.6795) [[hep-ex](#)]. SUSY-2013-22.
- 2885 [63] ATLAS Collaboration. “Search for metastable heavy charged particles with
 2886 large ionisation energy loss in pp collisions at $\sqrt{s} = 8$ TeV using the AT-
 2887 LAS experiment”. In: *Eur. Phys. J.* C 75 (2015), p. 407. doi: [10.1140/epjc/s10052-015-3609-0](https://doi.org/10.1140/epjc/s10052-015-3609-0). arXiv: [1506.05332](https://arxiv.org/abs/1506.05332) [[hep-ex](#)]. SUSY-
 2888 2014-09.
- 2889
- 2890
- 2891
- 2892

- 2893 [64] ATLAS Collaboration. “Search for heavy long-lived charged R -hadrons
 2894 with the ATLAS detector in 3.2 fb^{-1} of proton–proton collision data at
 2895 $\sqrt{s} = 13 \text{ TeV}$ ”. In: *Phys. Lett.* B760 (2016), pp. 647–665. doi: [10.1016/j.physletb.2016.07.042](https://doi.org/10.1016/j.physletb.2016.07.042). arXiv: [1606.05129](https://arxiv.org/abs/1606.05129) [hep-ex].
- 2897 [65] Torbjorn Sjöstrand, Stephen Mrenna, and Peter Skands. “PYTHIA 6.4 Physics
 2898 and Manual”. In: *JHEP* 0605 (2006), p. 026. doi: [10.1088/1126-6708/2006/05/026](https://doi.org/10.1088/1126-6708/2006/05/026). arXiv: [hep-ph/0603175](https://arxiv.org/abs/hep-ph/0603175).
- 2900 [66] *Further ATLAS tunes of PYTHIA6 and Pythia 8*. Tech. rep. ATL-PHYS-PUB-
 2901 2011-014. Geneva: CERN, 2011. url: <https://cds.cern.ch/record/1400677>.
- 2903 [67] Aafke Christine Kraan. “Interactions of heavy stable hadronizing parti-
 2904 cles”. In: *Eur. Phys. J.* C37 (2004), pp. 91–104. doi: [10.1140/epjc/s2004-01946-6](https://doi.org/10.1140/epjc/s2004-01946-6). arXiv: [hep-ex/0404001](https://arxiv.org/abs/hep-ex/0404001) [hep-ex].
- 2906 [68] M. Fairbairn et al. “Stable massive particles at colliders”. In: *Phys. Rept.* 438
 2907 (2007), p. 1. doi: [10.1016/j.physrep.2006.10.002](https://doi.org/10.1016/j.physrep.2006.10.002). arXiv: [hep-ph/0611040](https://arxiv.org/abs/hep-ph/0611040).
- 2909 [69] W. Beenakker, R. Hopker, M. Spira, and P. M. Zerwas. “Squark and gluino
 2910 production at hadron colliders”. In: *Nucl. Phys. B* 492 (1997), p. 51. doi:
 2911 [10.1016/S0550-3213\(97\)00084-9](https://doi.org/10.1016/S0550-3213(97)00084-9). arXiv: [hep-ph/9610490](https://arxiv.org/abs/hep-ph/9610490).
- 2912 [70] A. Kulesza and L. Motyka. “Threshold resummation for squark-antisquark
 2913 and gluino-pair production at the LHC”. In: *Phys. Rev. Lett.* 102 (2009),
 2914 p. 111802. doi: [10.1103/PhysRevLett.102.111802](https://doi.org/10.1103/PhysRevLett.102.111802). arXiv: [0807.2405](https://arxiv.org/abs/0807.2405) [hep-ph].
- 2916 [71] A. Kulesza and L. Motyka. “Soft gluon resummation for the production
 2917 of gluino-gluino and squark-antisquark pairs at the LHC”. In: *Phys. Rev.*
 2918 D 80 (2009), p. 095004. doi: [10.1103/PhysRevD.80.095004](https://doi.org/10.1103/PhysRevD.80.095004). arXiv:
 2919 [0905.4749](https://arxiv.org/abs/0905.4749) [hep-ph].
- 2920 [72] Wim Beenakker, Silja Brening, Michael Kramer, Anna Kulesza, Eric Lae-
 2921 nen, et al. “Soft-gluon resummation for squark and gluino hadroprodu-
 2922 tion”. In: *JHEP* 0912 (2009), p. 041. doi: [10.1088/1126-6708/2009/12/041](https://doi.org/10.1088/1126-6708/2009/12/041). arXiv: [0909.4418](https://arxiv.org/abs/0909.4418) [hep-ph].
- 2924 [73] W. Beenakker, S. Brening, M.n Kramer, A. Kulesza, E. Laenen, et al. “Squark
 2925 and Gluino Hadroproduction”. In: *Int. J. Mod. Phys. A* 26 (2011), p. 2637.
 2926 doi: [10.1142/S0217751X11053560](https://doi.org/10.1142/S0217751X11053560). arXiv: [1105.1110](https://arxiv.org/abs/1105.1110) [hep-ph].
- 2927 [74] Michael Krämer et al. *Supersymmetry production cross sections in pp collisions
 2928 at $\sqrt{s} = 7 \text{ TeV}$* . 2012. arXiv: [1206.2892](https://arxiv.org/abs/1206.2892) [hep-ph].
- 2929 [75] Rasmus Mackeprang and Andrea Rizzi. “Interactions of Coloured Heavy
 2930 Stable Particles in Matter”. In: *Eur. Phys. J.* C50 (2007), pp. 353–362. doi:
 2931 [10.1140/epjc/s10052-007-0252-4](https://doi.org/10.1140/epjc/s10052-007-0252-4). arXiv: [hep-ph/0612161](https://arxiv.org/abs/hep-ph/0612161)
 2932 [hep-ph].

- 2933 [76] Rasmus Mackeprang and David Milstead. “An Updated Description of
2934 Heavy-Hadron Interactions in GEANT-4”. In: *Eur. Phys. J.* C66 (2010), pp. 493–
2935 501. doi: [10.1140/epjc/s10052-010-1262-1](https://doi.org/10.1140/epjc/s10052-010-1262-1). arXiv: [0908.1868](https://arxiv.org/abs/0908.1868)
2936 [[hep-ph](#)].
- 2937 [77] J. Alwall, R. Frederix, S. Frixione, V. Hirschi, F. Maltoni, O. Mattelaer, H. S.
2938 Shao, T. Stelzer, P. Torrielli, and M. Zaro. “The automated computation of
2939 tree-level and next-to-leading order differential cross sections, and their
2940 matching to parton shower simulations”. In: *JHEP* 07 (2014), p. 079. doi:
2941 [10.1007/JHEP07\(2014\)079](https://doi.org/10.1007/JHEP07(2014)079). arXiv: [1405.0301](https://arxiv.org/abs/1405.0301) [[hep-ph](#)].
- 2942 [78] “dE/dx measurement in the ATLAS Pixel Detector and its use for particle
2943 identification”. In: (2011).
- 2944 [79] ATLAS Collaboration. “The ATLAS Simulation Infrastructure”. In: *Eur.*
2945 *Phys. J.* C70 (2010), pp. 823–874. doi: [10.1140/epjc/s10052-010-1429-9](https://doi.org/10.1140/epjc/s10052-010-1429-9). arXiv: [1005.4568](https://arxiv.org/abs/1005.4568) [[physics.ins-det](#)].
- 2946 [80] Alexander L. Read. “Presentation of search results: The CL(s) technique”.
2947 In: *J. Phys.* G28 (2002). [,11(2002)], pp. 2693–2704. doi: [10.1088/0954-3899/28/10/313](https://doi.org/10.1088/0954-3899/28/10/313).

2950 DECLARATION

2951 Put your declaration here.

2952 *Berkeley, CA, September 2016*

2953

Bradley Axen

2954

2955 COLOPHON

2956

Not sure that this is necessary.